SEISMIC ANISOTROPY DEPENDENCE ON FLUIDS, FRACTURES, AND STRESS: PHYSICAL MODELING WITH BAKKEN AND BARNETT SHALE FIELD CASES

A Dissertation Presented to the
Faculty of the Department of Earth and Atmospheric Sciences
University of Houston

In Partial Fulfillment
of the Requirements for the Degree
Doctor of Philosophy

By
Omoboya Olabode Kingsley
May 2015

SEISMIC ANISOTROPY DEPENDENCE ON FLUIDS, FRACTURES, AND STRESS: PHYSICAL MODELING WITH BAKKEN AND BARNETT SHALE FIELD CASES

Omoboya Olabode Kingsley

APPROVED:

Dr. Robert R. Stewart, Chairman (University of Houston)

Dr. Evgeny Chesnokov (University of Houston)

Dr. Yingcai Zheng (University of Houston)

Dr. Steven Peterson (formerly Marathon Oil Corporation)

Dean, College of Natural Sciences and Mathematics

ACKNOWLEDGEMENTS

Firstly, I would like to express my gratitude to **Dr. Robert R. Stewart** for his guidance and tutorship over the nearly six years we have met. I am indebted to him because of his support and mentorship throughout my graduate program at the University of Houston. I am also grateful to the AGL (Allied Geophysical Laboratories) for financial support.

I am privileged to have met **Dr. Nikolay Dyaur** and **Dr. Bob Wiley**, as they have been of immense help in acquiring and analyzing physical modeling data at the AGL. **Jay Krishnan** has been very helpful and responsive towards issues of seismic processing.

I would also like to thanks **Michele Simon** of Hess Corp and **Dr. Steven Peterson** (formerly of Marathon Oil) for their donation of dataset and expert help and advice in the duration of my graduate program. I'd like to acknowledge **Dr. Evgeny Chesnokov** for helping me understand the seemingly convoluted world of anisotropy, rock properties, tensors, etc. **Jose Jadsom de Figueiredo** was a great grad school colleague (and partner in crime); he was also a good collaborator on various publications. **Huw James** helped me better understand shale reservoirs due to his many decades of experience working in the industry.

I would like to thank my parents and siblings for unending support and encouragement. I'd like to single out my mother **Mabel Omoboya** for prayers and support during my graduate program.

Lastly, I thank my wife **Adetoun Omoboya** for her unending patience and support during my PhD program, especially towards the end, her encouragement and prayers were key to the overall success of the program.

DEDICATION

To the three most important women in my life:

My wife Toun, my daughter Kathlyn, and my mum Mabel.

SEISMIC ANISOTROPY DEPENDENCE ON FLUIDS, FRACTURES, AND STRESS: PHYSICAL MODELING WITH BAKKEN AND BARNETT SHALE FIELD CASES

A Dissertation Presented to the
Faculty of the Department of Earth and Atmospheric Sciences
University of Houston

In Partial Fulfillment
of the Requirements for the Degree
Doctor of Philosophy

By
Omoboya Olabode Kingsley
May 2015

ABSTRACT

A major goal of geophysical research is to understand and predict the seismic response of fluids, fractures, and stress in the subsurface. In this dissertation, we explored different forward modeling and field techniques with the goal of quantifying seismic anisotropy and its relationship with subsurface states. This dissertation includes two series of physical modeling experiments as well as analyses of wide-azimuth 3D data from the Williston Basin in North Dakota and the Fort Worth Basin in Texas. In the first set of lab experiments, we explored fluid substitution effects in a synthetic anisotropic medium. We observed the effects of different fluids on wide-azimuth P-wave NMO ellipses from our synthetic composite rock sample. We find that fluid substitution from air to water can increase inherent anisotropies by as much as 50%. We also observe changes in P-wave NMO ellipses as a function of different fluid saturants in the synthetic sample. In the second set of experiments, we varied uniaxial normal stress and measured transit-time and its associated effects on a layered synthetic orthorhombic medium. The experiment was designed to measure the dynamic elastic properties of sedimentary reservoir rocks deposited in layers under stress. Results show a general increase in all measured velocities with stress ranging from 4% to 10%. We also observed anisotropic behavior *a priori* to both orthorhombic and VTI symmetries in different principal axes of the synthetic sample as uniaxial stress changes. 3D wide-azimuth data from the Ross Field of the Williston Basin in North Dakota is fully processed using conventional techniques. We presented a velocity-based workflow for inverting for the direction and intensity of preferred orientations within the subsurface. We demonstrate a potential for using wide-azimuth P-wave seismic data as

a tool for subsurface characterization in shale reservoirs. Lastly, using fully processed wide-azimuth 3D dataset and wells from the Fort Worth Basin in Texas, we presented a workflow that integrated RMO analysis and azimuthally sectored inversions to generate a broad overview of subsurface orientation in the Barnett shale play.

TABLE OF CONTENT

LIST OF TABLES

LIST OF FIGURES

CHAPTER ONE

INTRODUCTION

With the advent and tremendous growth of unconventional oil and gas production in the US, the need arises to adequately understand and characterize fractures and *in-situ* stress state in the subsurface (Sonnenberg, 2013). Much of this unconventional oil and gas is produced from naturally occurring or induced fractures after hydraulic fracturing.

This dissertation uses a combination of modeling and imaging tools to better understand the effects of fluids, fractures, and stress on seismic wavefields. Fracture spacing and dimensions can range from a few millimeters to tens of meters. *In-situ* stress can also vary greatly within a geologic setting (Pollastro et al. 2008). As a result, the seismic response to fractures and stress is dependent on a whole suite of factors, ranging from fracture dimension to fluid saturation and the direction of minimum and maximum horizontal stress. In this dissertation, we attempt to model these effects individually (effects of stress and fluid-filled fractures on seismic anisotropy).

Different theories of wave propagation in fractured azimuthally anisotropic media have been proposed: the penny-shaped crack model by Hudson (1980, 1981) and Thomsen (1995) and the linear slip model by Schoenberg (1980, 1983). Eshelby (1957) and Crampin (1985) proposed a method of relating the magnitude of shear-wave splitting to fracture density. The Kuster and Toksöz (1974) method was based on a long-wavelength, first-order scattering theory for calculating the effective moduli for randomly distributed fractures. Following these theoretical models, a variety of techniques have been developed to help characterize fractures in the subsurface. Lynn et al. (1995) and Lynn (2004a, 2004b), used a method based on amplitude variation with reflection amplitudes in different azimuths for fracture characterization. Tsvankin and Grechka (2011) used normal moveout ellipses in wide-azimuth data for characterizing fractures and *in-situ* stress. Here, we adopt workflows similar to Tsvankin and Grechka (2011) to wide-azimuth data from the Williston Basin.

In this dissertation, each chapter details a different set of experiment or field analysis related to anisotropic media. Two sets of physical modeling work, and two field studies that included processing, imaging, and interpretation of wide-azimuth data are presented.

Chapter 2 presents an experiment on the effects of direct fluid substitution on seismic anisotropy in a synthetic HTI medium. We replaced air (gas proxy) with water (brine proxy) and later glycerin (oil proxy) and observed the change in elastic and seismic properties of the medium. We also presented NMO ellipses from the three different fluid substitution states. We believe results from this experimental project can help better understand effects on fluid substitution in an anisotropic media in a controlled environment.

In Chapter 3, we study the dynamic elastic properties of layered orthorhombic medium under uniaxial normal stress. We observed that stress plays a key role in observed anisotropic anomalies in any medium. We find that certain anisotropic attributes seem to dominate the character of anisotropy as stress increases.

In Chapter 4, using wide-azimuth surface seismic data from the Williston basin we demonstrate a potential for using wide-azimuth P-wave seismic data as a tool for subsurface characterization in shale reservoirs. This project included full processing of 3D wide-azimuth data from the Red Sky survey. Finally we presented NMO ellipses from various wells at the level of our reservoir of interest. In this project, we find our results agree with results from other data sources such as microseismic data. We also recommend that wide-azimuth acquisition and processing of converted-wave data might help better anisotropic characterization in this shale play. As shown by Stewart et al. (2003) and Far and Hardage (2014), converted waves can provide more accurate information orientation and intensity of fractures.

In Chapter 5, we combined the analysis of RMO with azimuthally sectored inversion to create a broad overview of the nature of anisotropy in the Fort Worth Basin. The data used was a fully processed wide-azimuth 3D dataset and wells from the Fort Worth Basin in Texas. In this chapter, we were able to observe and distinguish observed anisotropies that were due to highly dipping structures in the Ellenberger Formation.

Overall conclusions and future works are stated in Chapter 6.

1.1 Fundamentals of seismic anisotropy and the effective medium theory

Rock formations are made up of heterogeneities of different scales down to the atomic level. Heterogeneities are typically smaller than the wavelength of the incident wave-field travelling through the medium. However, if these heterogeneities are aligned or biased towards a particular direction, then the usual isotropic and homogeneous assumptions begin to fail. In essence, anisotropy occurs as a result of aligned inhomogeneities. A set of fractures or faults with a preferred orientation will give a rock formation an effective anisotropy with a favored axis of symmetry.

Backus (1959) introduced the "equivalent medium theory" to permit the prediction of the stiffness coefficients of a polar anisotropic medium (VTI) from a given set of layers. The equivalent medium theory allows the prediction of properties of a heterogeneous medium by replacing small scale heterogeneities with a conceptually homogeneous medium that can still predict stiffness coefficients from the heterogeneous medium.

Hooke's law of elasticity forms the foundation of seismic anisotropy as it does for most of seismology:

$$\tau_{ij} = C_{ijkl} E_{kl} \tag{1.1}$$

where τ_{ij} is the second rank stress tensor, C_{ijkl} is the fourth rank elastic moduli tensor and E_{kl} describes the strain field.

Consider Newton's equation of motion;

$$\rho \frac{\partial^2 U_i}{\partial t^2} = \frac{\partial \tau_{ij}}{\partial x_j} \tag{1.2}$$

where U_i is the displacement of a particle at time t and position x and τ_{ij} is the stress tensor (force per unit area) and defining the strain tensor (symmetry of strain tensor)

$$E_{ik} = \frac{1}{2}\left(\frac{\partial U_i}{\partial x_k} + \frac{\partial U_k}{\partial x_i}\right) \tag{1.3}$$

$$\tau_{ij} = \sum_{k,l} C_{ijkl}\, E_{kl} = C_{ijkl}\, E_{kl} \tag{1.4}$$

Combine these equations with Hooke's law;

$$\rho\frac{\partial^2 U_i}{\partial t^2} = C_{ijkl}\,\frac{\partial^2 U_m}{\partial x_n \partial x_j} \tag{1.5}$$

We arrive at the generalized wave equation in both the isotropic and anisotropic media.

Hooke's law assumes stress and strain are linearly dependent. As a result,

$$\tau_{11} = C_{1111}E_{11} + C_{1112}E_{12} + C_{1113}E_{13} + \cdots$$
$$\tau_{12} = C_{1211}E_{11} + C_{1212}E_{12} + C_{1213}E_{13} + \cdots$$

(1.6)

The symmetry of the medium is captured in $C_{\alpha\beta}$, since both stress and strain are symmetric i.e., $ij = ji$ (stress symmetry) and $kl = lk$ (strain symmetry); we can simplify using the Voigt notation.

$$C_{ijkl} = C_{\alpha\beta}$$

ij	11	22	33	23	13	12
α	1	2	3	4	5	6

We can now reconstruct the stiffness matrix as follows:

$$\begin{bmatrix} C_{11} & C_{12} & C_{13} & C_{14} & C_{15} & C_{16} \\ C_{12} & C_{22} & C_{23} & C_{24} & C_{25} & C_{26} \\ C_{13} & C_{23} & C_{33} & C_{34} & C_{35} & C_{36} \\ C_{14} & C_{24} & C_{34} & C_{44} & C_{45} & C_{46} \\ C_{15} & C_{25} & C_{35} & C_{45} & C_{55} & C_{56} \\ C_{16} & C_{26} & C_{36} & C_{46} & C_{56} & C_{66} \end{bmatrix} \tag{1.7}$$

Once again, due to the symmetry of $C_{\alpha\beta}$, only 21 independent matrix elements are possible.

The types of symmetry available in a crystal depend on the number of independent elastic constants.

Symmetry type	Number of independent elastic constants
Triclinic	21
Monoclinic	13
Orthorhombic	9
Tetragonal	7
Trigonal (rhombic)	7
Hexagonal (Polar)	5
Cubic	3
Isotropic	2

Table 1.1: Anisotropic symmetry types and corresponding number of independent elastic constants.

In this study, we have discussed only a few of these symmetries as they affect our experiments and field study.

In an isotropic symmetry, only two independent elastic constants exist and the $C_{\alpha\beta}$ matrix will appear as:

$$\begin{bmatrix} c & \lambda & \lambda & 0 & 0 & 0 \\ \lambda & c & \lambda & 0 & 0 & 0 \\ \lambda & \lambda & c & 0 & 0 & 0 \\ 0 & 0 & 0 & \mu & 0 & 0 \\ 0 & 0 & 0 & 0 & \mu & 0 \\ 0 & 0 & 0 & 0 & 0 & \mu \end{bmatrix} \tag{1.8}$$

where $\lambda = c - 2\mu$, $c = K + \frac{4}{3}\mu$ and $\mu = \rho V_s^2$

1.1.1 Polar anisotropy

Polar anisotropy is the simplest realizable anisotropic symmetry in the earth (Ikelle and Amundsen, 2005). It is also commonly known as TI (transverse isotropy) symmetry. The symmetry axis is determined by either gravity (VTI) or regional stress/fractures (HTI). Figures 1.1 and 1.2 shows schematic diagrams of VTI and HTI symmetries.

The stiffness tensor of a VTI matrix is as follows:

$$\begin{bmatrix} C_{11} & C_{12} & C_{13} & 0 & 0 & 0 \\ C_{12} & C_{11} & C_{13} & 0 & 0 & 0 \\ C_{13} & C_{13} & C_{33} & 0 & 0 & 0 \\ 0 & 0 & 0 & C_{44} & 0 & 0 \\ 0 & 0 & 0 & 0 & C_{44} & 0 \\ 0 & 0 & 0 & 0 & 0 & C_{66} \end{bmatrix} \tag{1.9}$$

where $C_{12} = C_{11} + 2C_{66}$

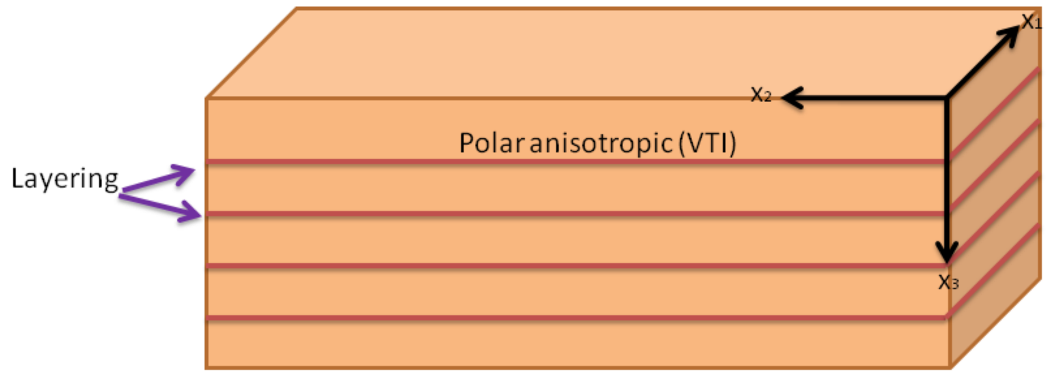

Figure 1.1: Schematic diagram of polar anisotropic symmetry (VTI case), modified from Far, (2011).

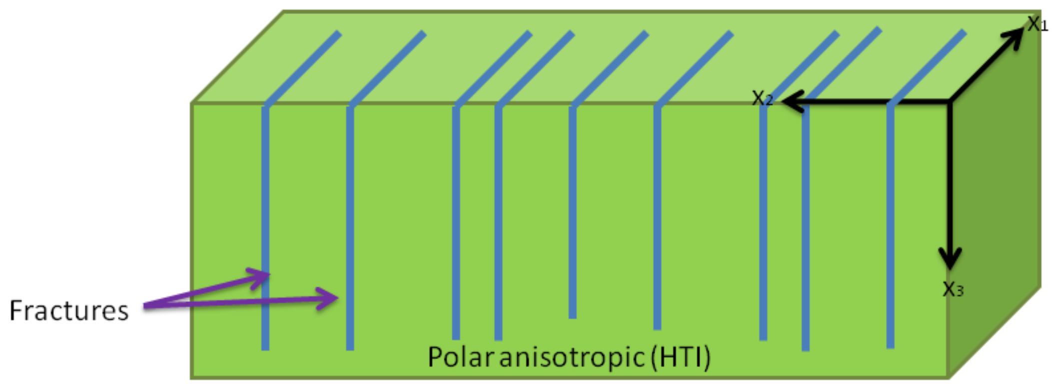

Figure 1.2: Schematic diagram of polar anisotropic symmetry (HTI case), modified from Far, (2011).

Thomsen (1986) introduced the Thomsen parameters assuming weak elastic anisotropy. These parameters for a VTI case are summarized here:

$$\varepsilon = \frac{C_{11} - C_{33}}{2C_{33}} \tag{1.10}$$

$$\gamma = \frac{C_{66} - C_{44}}{2C_{44}} \tag{1.11}$$

$$\delta = \frac{(C_{13} + C_{44})^2 - (C_{33} - C_{44})^2}{2C_{44}} \tag{1.12}$$

Epsilon ε is a measure of compressional wave anisotropy, Gamma γ is the measure of delay between fast and slow shear-waves (will be zero in VTI symmetry) and Delta δ is a combination of stiffness coefficients and velocities specifically applicable to the field of exploration seismology.

Alkhalifah (1997) suggested that VTI media had non-hyperbolic moveout and that this moveout was highly dependent on V_{nmo} and η where eta η is a combination of anisotropic parameters and is also a function of horizontal and NMO velocities Alkhalifah (1997):

$$\eta = \frac{1}{2}\left(\frac{V_h^2}{V_{nmo}^2} - 1\right) = \frac{\varepsilon - \delta}{1+2\delta} \tag{1.13}$$

The hyperbolic travel time equation can therefore be re-written in a non-hyperbolic form:

$$t^2 = t_0^2 + \frac{X^2}{V_{nmo}^2} - \frac{2\eta X^4}{t_0^2 V_{nmo}^4} \tag{1.14}$$

1.1.2 Orthorhombic anisotropy

Vertical fractures and horizontal layering combine to form orthorhombic symmetry (Schoenberg and Helbig, 1997). In essence, a combination of parallel vertical fractures due regional stress and a background VTI medium could cause of orthorhombic symmetry. Orthorhombic symmetry is characterized by three planes of symmetry. Due to two very common geologic phenomena (sedimentation/layering and regional stress), orthorhombic anisotropy might be the simplest and most realistic earth model for any geophysical problem (Schoenberg and Sayers, 1995). Figure 1.3 shows a schematic diagram of orthorhombic symmetry.

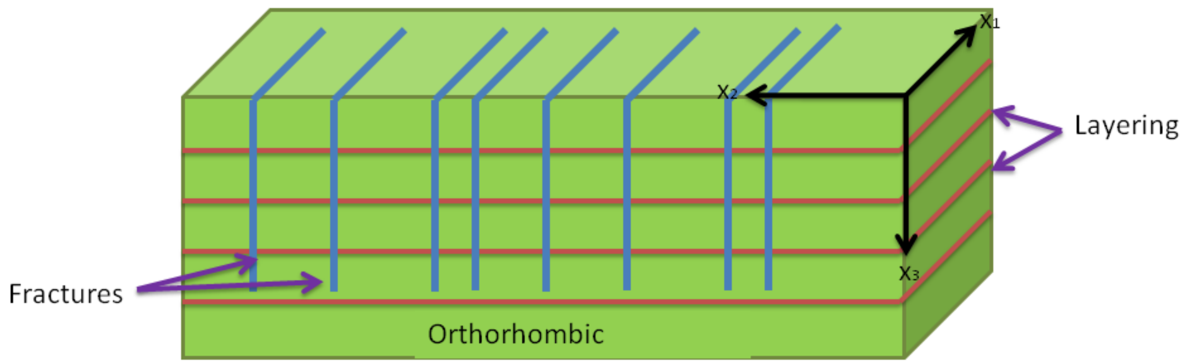

Figure 1.3: Schematic diagram of orthorhombic symmetry (caused by layering and fractures/stress), modified from Far, (2011).

In orthorhombic symmetry the matrix $C_{\alpha\beta}$ has only 9 independent elements:

$$\begin{bmatrix} C_{11} & C_{12} & C_{13} & 0 & 0 & 0 \\ C_{12} & C_{22} & C_{23} & 0 & 0 & 0 \\ C_{13} & C_{23} & C_{33} & 0 & 0 & 0 \\ 0 & 0 & 0 & C_{44} & 0 & 0 \\ 0 & 0 & 0 & 0 & C_{44} & 0 \\ 0 & 0 & 0 & 0 & 0 & C_{66} \end{bmatrix} \tag{1.14}$$

Tsvankin (1997) extended Thomsen's parameters for orthorhombic symmetry. Since there are three mirror symmetry planes, all anisotropic parameters are in triplicate:

$\varepsilon^1 = \dfrac{C_{22} - C_{33}}{2C_{33}}$	$\varepsilon^2 = \dfrac{C_{11} - C_{33}}{2C_{33}}$	$\varepsilon^3 = \dfrac{C_{11} - C_{22}}{2C_{22}}$
$\gamma^1 = \dfrac{C_{66} - C_{44}}{2C_{44}}$	$\gamma^2 = \dfrac{C_{66} - C_{55}}{2C_{55}}$	$\gamma^3 = \dfrac{C_{55} - C_{44}}{2C_{44}}$
$\delta^1 = \dfrac{(C_{23} + C_{44})^2 - (C_{33} - C_{44})^2}{2C_{33}(C_{33} - C_{44})}$	$\delta^2 = \dfrac{(C_{13} + C_{55})^2 - (C_{33} - C_{55})^2}{2C_{33}(C_{33} - C_{55})}$	$\delta^3 = \dfrac{(C_{12} + C_{66})^2 - (C_{11} - C_{66})^2}{2C_{11}(C_{11} - C_{66})}$

Table 1.2: Tsvankin (1997) extension of Thomsen's parameters for orthorhombic symmetry.

In this dissertation we analysed the evolution of elastic properties in two physical models with known anisotropic symmetries (HTI and orthorhombic symmetries) while varying physical properties like stress and fluid saturation. Enlightened by the theoretical analysis of various elastic matrices and symmetries discussed in this chapter, we are able to determine the approximate anisotropic symmetry of a model by only measuring P- and S-wave transit-times across orthogonal axes.

In field (or real-world) cases however, these analyses are more complicated. Understanding the anisotropic trend or symmetry of any rock layers (*in-situ*) is most likely the goal of the study. In a real-world case, we have to collate and assemble clues from different studies to begin to create a detailed picture of the subsurface. These studies might be in the form of Azimuthal NMO analysis, AVAZ, residual delay analysis, and results from microseismic/VSP data.

1.2 References

Alkhalifah, T., 1997, Seismic data processing in vertically inhomogeneous TI media. Geophysics. **62**, 662-675

Backus, M. M., 1959, Water reverberations, their nature and elimination. Geophysics. **24**, 233–261.

Crampin, S., 1985, Evaluation of anisotropy by shear-wave splitting. Geophysics. **50** 142-152.

Eshelby, J.D., 1957, The determination of the elastic field of an ellipsoidal inclusion, and related problems. Proceedings of the Royal Society of London. **241**, 376-396

Far, M. E., 2011, Seismic characterization of naturally fractured reservoirs. Ph.D. dissertation, University of Houston, Houston, TX.

Far, M. E., and B. Hardage, 2014, Interpretation of fractures and stress anisotropy in Marcellus Shale using multicomponent seismic data. Interpretation. **2**, 105-115.

Hudson, J. A., 1980, Overall properties of a cracked solid. Mathematical Proceedings of the Cambridge Philosophical Society. **88,** 371-384.

Hudson, J. A., 1981, Wave speeds and attenuation of elastic waves in material containing cracks. Geophysical Journal of the Royal Astronomical Society. **64,** 133–150.

Ikelle, L., and L, Amundsen., 2005, Introduction to Petroleum Seismology, Investigations in Geophysics series; no **12**. Society of Exploration Geophysicist.

Kuster, G.T., and M.N, Toksöz, 1974, Velocity and attenuation of seismic waves in two-phase media: Part I. theoretical formulations. Geophysics. **39**, 587-606

Lynn, H. B., 2004a, The winds of change: Anisotropic rocks: Their preferred direction of fluid flow and their associated seismic signatures: Part 1. The Leading Edge. **23**, 1156–1162.

Lynn, H. B., 2004b, The winds of change: Anisotropic rocks: Their preferred direction of fluid flow and their associated seismic signatures: Part 2. The Leading Edge. **23**, 1258–1268.

Lynn, H. B., C. R. Bates, M. Layman, and M. Jones, 1995, Natural fracture characterization using P-wave reflection seismic data, VSP, borehole imaging logs, and the in-situ stress field determination, SPE paper 29595, presented at the SPE Rocky Mountain Regional/Low-Permeability Reservoirs Symposium, Denver, 20-22 March 1995.

Pollastro, R.M., L.N.R. Roberts, T. A. Cook, and M.D. Lewan, 2008, Assessment of undiscovered technically recoverable oil and gas resources of the Bakken Formation, Williston Basin, Montana and North Dakota. USGS Open-File Report 2008–1353 Sheet 3 of 3.

Schoenberg, M., 1980, Elastic wave behavior across linear slip interfaces. The Journal of the Acoustic Society of America. **68**, 1516–1521.

Schoenberg M., 1983, Reflection of elastic waves from periodically stratified media with interfacial slip. Geophysical Prospecting. **31**, 265–292.

Schoenberg, S., and C.M, Sayers, 1995, Seismic anisotropy of fractured rocks. Geophysics. **60**, 204–211.

Schoenberg, S., and K, Helbig, 1997, Orthorhombic media: Modeling elastic wave behavior in a vertically fractured earth. Geophysics. **62**, 1954–1974.

Sonnenberg, A.S., 2013, Interest, activity continue in the Bakken. Bakken/Exshaw. The 2 013 Playbook. Harts Energy/Oil and Gas investor.

Stewart, R. R., J. E. Gaiser, R. J. Brown, and D. C. Lawton, 2003, Converted-wave seismic exploration: Applications. Geophysics. **68**, 40–57.

Thomsen, L., 1986, Weak elastic anisotropy. Geophysics. **51**, 1954-1966.

Thomsen, L., 1995, Elastic anisotropy due to aligned cracks in porous rocks. Geophysical Prospecting. **43**, 805–829.

Tsvankin, I., 1997, Reflection moveout and parameter estimation for horizontal transverse isotropy. Geophysics. **62**, 614-629.

Tsvankin, I., and V. Grechka, 2011, Seismology of azimuthally anisotropic media and seismic fracture characterization. Society of Exploration Geophysicist.

CHAPTER TWO

Effects of fluid substitution on elastic anisotropy in an HTI physical model

Bode Omoboya[1], J.J.S. de Figueiredo[1, 2], Nikolay Dyaur[1] and Robert R. Stewart[1]

[1]-University of Houston, Department of Earth and Atmospheric Sciences, Houston-Texas, USA: Email: bodeomoboya@gmail.com, nidyaur@gmail.com and rrstewart@uh.edu

[2]-Federal University of Para, Geophysics Department & National Institute of Petroleum Geophysics (INCT-GP), Belém-Pará, Brazil: Email: jadsom@ufpa.br

2.1 Summary

Seismic characterization of subsurface fractures has important applications and implications to reservoir characterization. Recent studies have shown that characterization of azimuthal anisotropy can help delineate orientation and intensity of fractures, as well as indicate the fluid content of their embedded cracks. To explore the influence of fluids on seismic response in an HTI medium, an experimental study using vertically aligned and preconditioned polycarbonate material embedded in isotropic resin was conducted. In a series of ultrasonic transmission and reflection experiments, the model was initially filled with air (a natural gas proxy) and then liquids (distilled water and glycerin as brine and oil proxies, respectively) were gradually injected into the composite material to simulate different fraction of fluid saturation. Porosity in our assembled cracked media was about 2.5% and crack density was estimated to be 3.5%. Our results show changes in ultrasonic compressional and shear-wave velocities in different directions as a function of different

saturating fluids. We also detected changes in delay between fast and slow split shear-waves as a function of different saturating fluids. The NMO velocity measured from the ultrasonic reflection response, showed not only changes in velocity values on saturation, but also a difference in the trend of NMO velocities as a function of source-receiver azimuth. Anisotropic parameters also varied with different levels of saturation. Our experiments indicate that the anisotropic parameter ε is reduced by 35% on full saturation with water (brine proxy) and 50% with glycerin (oil proxy). The anisotropic parameter γ increased by 35% from a gas-to-brine saturated medium and 40% from a gas-to-oil saturated medium. The most significant changes in elastic properties occur when gas is substituted for distilled water or glycerin. Changes in stiffness properties are small when brine is substituted for oil and vice versa.

Omoboya, B., J.J.S De Figueiredo, N. Dyaur, and R.R. Stewart, 2014, Experimental study of the influence of fluids on seismic azimuthal anisotropy: Journal of Petroleum Science and Engineering, Volume 130, June 2015, Pages 46-54.

2.2 Introduction

Transverse isotropy with a horizontal axis of symmetry is a simple and common azimuthally anisotropic earth model (Tsvankin, 1997). One major geological phenomenon that can lead to azimuthal anisotropy is regional stress (Sayers, 2002). A detailed knowledge of fracture orientation and fluid infill of the cracks would be ideal for reservoir characterization in many scenarios (in particular, hydraulic fracturing). In addition, time-lapse studies before and after hydraulic fracturing may give an in-depth insight to the relationship between fluids and seismic properties in the reservoir (Angerer et al., 2002).

Different theories of wave propagation in fractured azimuthal anisotropic media have been proposed: the penny-shaped crack model by Hudson (1980, 1981) and Thomsen (1995) and the linear slip model by Schoenberg (1980, 1983). Eshelby (1957) and Crampin (1985) proposed a method of relating the magnitude of shear-wave splitting to fracture density. The Eshelby model concludes that the magnitude of shear-wave splitting is directly proportional to fracture density. Sayers (2002) explored the interrelationship between shear compliance, normal compliance, and fluid infill of cracks in relation to shear-wave birefringence. In the Sayers model, shear-wave splitting depends on shear compliance, and shear compliance is in turn influenced by fluid bulk modulus. This theory connects the sensitivity of seismic birefringence to fluid type in a cracked medium (Galvin et al., 2007). Most experimental and field tests of these theories appear to support the claim that shear-wave splitting is affected by the type of fluid infill in the cracks. Potters et al. (1999) and Van der Kolk et al. (2001) demonstrated differences in shear-wave splitting as a function of fluid type (gas and oil) in a known carbonate reservoir. Rathore et al. (1995) measured acoustic anisotropy and observed shear-wave splitting in a synthetic sandstone sample.

Tillotson et al. (2011) added fluid dependence in some special cases to a similar synthetic porous rock medium and concluded that shear-wave splitting is related to fluid viscosity. Ebrom et al. (1990) and Tatham et al. (1992) explored seismic response in an effective anisotropic medium using polycarbonate sheets. We employ an approach similar to that of Tatham et al. (1992) to the more specific case in which we incorporate different saturating fluids. We also investigated the effective medium response of our model with different fluids. Our assembled cracked medium is of known fracture orientation and dimensions as well as having a controlled fraction of fluid saturation.

Many attempts have been made to use multicomponent data for reservoir characterization in fractured reservoirs. Mueller (1992) analyzed seismic amplitudes in fast and slow shear-wave sections in the Austin Chalk and was able to correlate amplitude anomalies to higher productivity from surrounding wells. Lynn and Thomsen (1990) analyzed and related incremental misties from fast and slow shear seismograms to the direction of cracks in a fractured reservoir. Stewart et al. (2002, 2003) provided a detailed approach to the use of multicomponent data for estimating and analyzing fracture properties in subsurface targets. Our experimental study considers the effect of different fluid infills in aligned cracks embedded in an isotropic matrix. We describe here the first part of a series of ultrasonic experiments that include water (brine substitute) and glycerin (oil substitute) saturation in an inherently anisotropic medium. Fracture orientation and fluid properties in reservoirs are largely unknown in the exploration phase; however, in this experimental study, we aspire to use known laboratory models and surveys to inform the assessment of field data over fractured reservoirs. A limitation of ultrasonic physical modeling is that the rock properties extracted from the model are determined at relatively high (100s of kHz) frequencies. However, the ratio of our wavelength to crack spacing is large. Thus, physical modeling can assist in understanding wave propagation between numerical analysis and field data. We are thus creating a well-known model with complete acquisition geometry to simulate the real-earth *(in-situ*).

2.3 Sample description

Under controlled conditions, we constructed an anisotropic physical medium consisting of an HTI fracture volume. The fractures comprised of stacked polycarbonate sheets immersed in an isotropic matrix made of epoxy resin. Our assembled cracked medium is composed of grooved or roughened polycarbonate plates. The medium is a 30 cm (X) by 30 cm (Y) by 13 cm (Z) model, made up of an assortment of materials from polycarbonate plates to copper tubes to act as fluid injectors. Figure 2.1 is a photograph of the composite model showing all principal directions and aligned fractures in the centre.

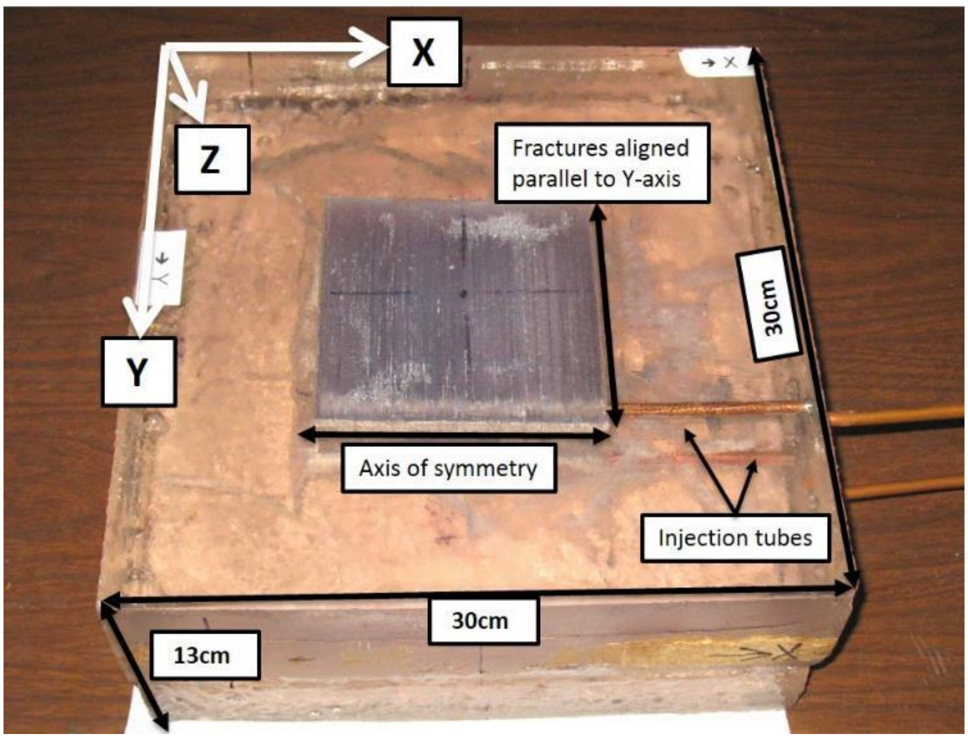

Figure 2.1: Photograph of physical model showing aligned fractures in the center and copper tubes for fluid injection. Full model dimension is 30 cm by 30 cm by 13 cm.

The composite model is composed of 95 grooved or scratched polycarbonate sheets contained in an isotropic resin material. Epoxy resin was used to help locally isolate fracture domains from surrounding saturations and to keep the fractured reservoir in the same condition during different liquid or gas replacements. This allowed us to independently study the influence of different fluid saturations on elastic properties of the model.

The indents or grooves on the polycarbonate sheets were made using sandpaper to help develop porosities. All polycarbonate sheets are aligned vertically to serve as a fracture plane. Each polycarbonate sheet has a thickness of about 1.2 mm. The depth of the indents or grooves is about 0.25 mm. These indents were randomly placed along each polycarbonate sheet. This was designed to mimic oval or penny-shaped (with very low aspect ratio) cracks that lead to HTI symmetry. A crack may be referred to as a low-aspect ratio void in the rock matrix, (Gueguen and Sarout, 2011). The cracks embedded in our sample are very thin (thread-like) but run in all directions parallel to the fracture plane. This assemblage of fractures was then embedded in a resin background. The fabrication process was conducted in a vacuum chamber. Figure 2.2 gives a schematic diagram of the composite model.

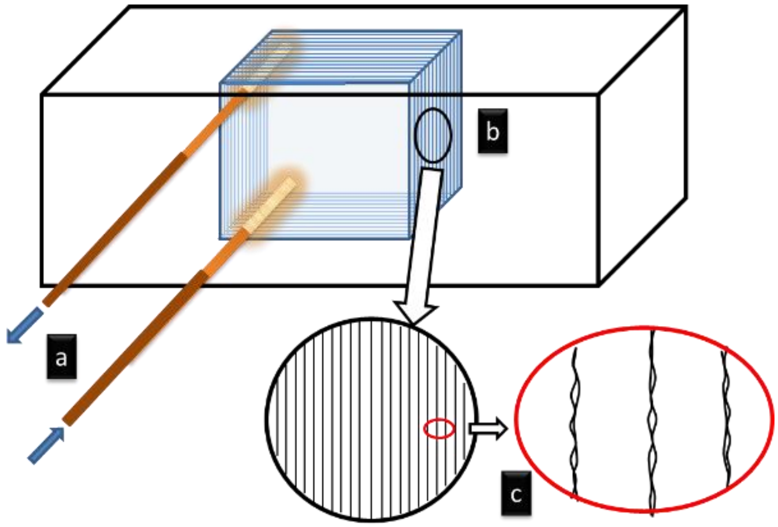

Figure 2.2: Schematic diagram of composite model showing fracture system: a) Copper tubes for fluid injection, b) Fracture zone made up of 95 polycarbonate sheets and c) Schematic magnification on polycarbonate sheets showing crack indents (not to scale).

Before individual materials were assembled together into the composite model, measurements of density and velocity were taken on each sample. Velocities were inferred from transit-time (transmission) recordings. Densities were inferred from mass and volume measurements. Details of these measurements are discussed in section 2.3. Error analysis is discussed in section 2.4.1. Table 2.1 shows physical properties of individual materials that make up the composite model.

On close inspection, we found the composite sample and the fracture area to be slightly orthorhombic but the physical properties in the Y (2) and Z (3) directions are close enough to consider them transversely isotropic with horizontal axis of symmetry. In this study, the composite model was thus treated as a polar anisotropic model with a horizontal axis of symmetry (HTI).

	V_P (m/s)	V_S (m/s)	V_P/V_s	Density (g/cm^3)
Individual polycarbonate sheet	2300 ± 25.5	1320 ± 18.7	1.74	1.19
Isotropic (undisturbed) resin	2540 ± 33.0	1250 ± 16.5	2.03	1.22

Table 2.1: Physical properties of constituent materials that make up the composite model.

2.4 Experimental setup

Two types of experiments were undertaken on the composite sample in the work presented here. All experiments, model fabrication, and testing were carried out at the Allied Geophysical Laboratories, University of Houston. The two types of experiments were:

1) Ultrasonic transmission measurements (direct source to receiver recordings, i.e. one-way transit time) were taken in three orthogonal axes and one oblique direction to estimate velocities and consequently compute elastic parameters as functions of fluid saturation. We will refer to these experiments as the "transmission" experiments throughout this article;
2) Scaled surface reflection (source to reflector, reflector to receiver in CMP style acquisition) measurements were taken before and after liquid (water and glycerin) saturation. We will refer to these as the "reflection" experiments.

One main goal of this study was to create an anisotropic physical model with fractures that could be filled with fluids under controlled conditions. Scaled ultrasonic measurements were taken in all orthogonal directions on the block faces, travel times were picked directly from a digital oscilloscope and inverted for compressional and shear-wave velocities, stiffness coefficients, and anisotropic parameters. In each set of experimental studies, liquid saturation was gradually increased (and air expelled), and all measurements were repeated.

The principal axes of the model were labelled X, Y, and Z, with Z being the vertical direction (see Figure 2.1). The Z direction is of much interest to exploration geophysics. In our case, only the Z (3) and X (1) directions were investigated because of HTI symmetry. Initial testing of the model revealed enough similarity between the Z (3) and Y (2) directions (less than 3% difference).

Water and glycerin saturations were increased from 0% to 50% and then to 100% (initial saturation of the composite medium was air). Much care was taken so that air was expelled and replaced with water or glycerin during this process by installing valves on the ends of the copper tubes to prevent air leakage and to keep contaminants out. In each case, a fluid was injected into one valve and the resident fluid was expelled through the other. The injection process was continued until the density of the ejected fluid was the same as that of the injected fluid indicating that the medium was saturated with the desired fluid. Densities of the fluids were estimated by taking a sample of the ejected fluid in a syringe and measuring the mass (and volume) of the syringe on a digital weight scale. The density comparison was particularly useful when replacing water with glycerin. This was to ensure there was no residual dissolved air or undesired liquid (water in the case of glycerine saturation) remained in the system.

Our ultrasonic measurement system included a 5077PR pulsar/receiver, an HS-4 (50 MHz) digital oscilloscope, low-noise preamplifiers and P- and S-wave transducers with central frequencies of 0.1MHz. The dominant wavelength of the compressional wave was ~30 mm (the thickness of polycarbonate sheet was ~1.2 mm). This provides an ultrasonic wavelength that was at least 10 times the thickness of each polycarbonate sheet (or fracture aperture). The diameter of P-wave transducers (both source and receiver) was 38 mm, and that of S-wave transducers was 25.4 mm. With this configuration, we measured the velocity of compressional and shear-waves in different orthogonal directions to characterize anisotropy in the model.

In the first set of experiments (the transmission experiments), transit time measurements were taken in the Z and X axes and then the model was injected with water or glycerin; measurements are repeated at different saturation fractions. For shear-wave measurements (mostly on the Z axes), the shear transducers (both transmitting and receiving transducers simultaneously) were rotated 0^o to 360^o every 10^o and S-wave transit-time measurements were repeated at every instance of rotation to infer fast and slow shear-wave directions (and consequently fast and slow shear-wave velocities). Figure 2.3 is a schematic diagram showing the position and polarization of the shear-wave transducers in the transmission experiment, relative to embedded fractures (or stack of polycarbonate sheets). Polarization of the shear transducers were varied every 10^o simultaneously (both transmitting and receiving transducers).

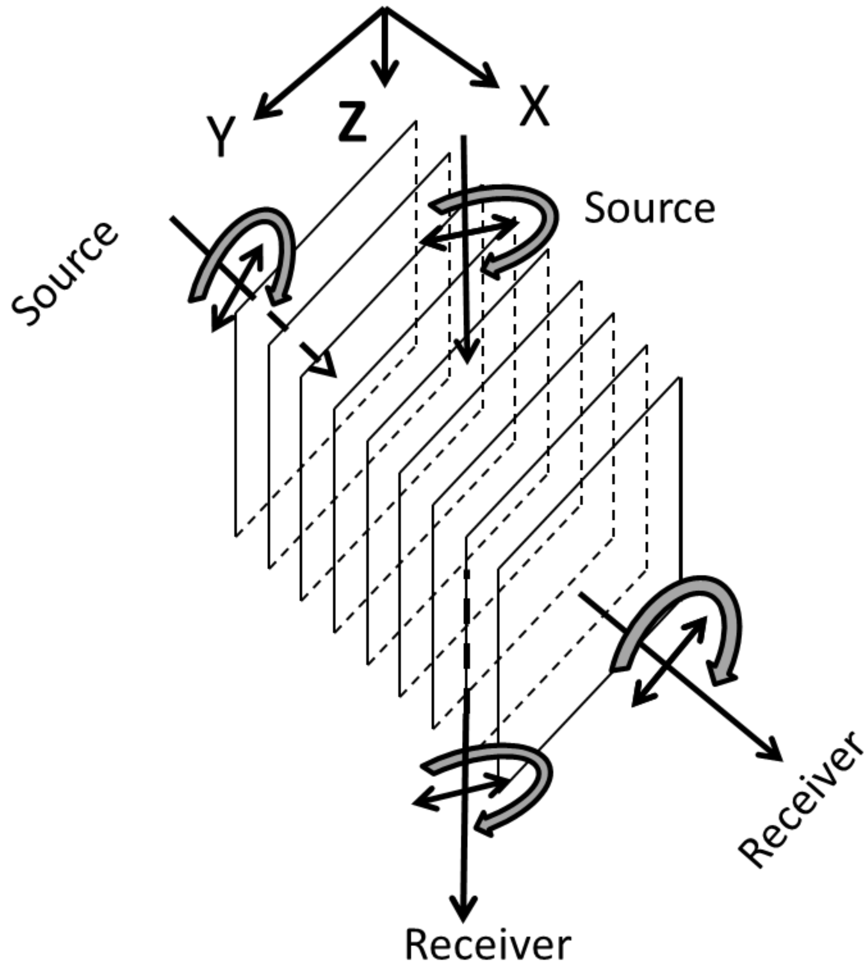

Figure 2.3: Schematic diagram of the ultrasonic shear-wave transmission experimental setup relative to aligned fractures (polycarbonate sheets), showing position and polarization S-wave transducers. S-wave polarization ranged from 0^0 to 360^0 (measurement taken every 10^o interval)

Figure 2.4 is an annotated photograph of the transmission experimental setup (for both P-waves and S-waves).

Fast and slow shear-wave arrivals were picked individually from a digital oscilloscope; results were reviewed by plotting all oscilloscope traces.

The wavelength of the shear-wave used was ~15mm. In all measurements (both compressional and shear-wave), the ultrasonic wavelengths were greater than the thickness of the polycarbonate sheet or fracture aperture, ensuring an effective seismic (elastic) response from the model. Velocity measurements were also taken at an oblique angle of 17^o on the XZ plane. Angle-dependent velocities were used to compute stiffness parameter C_{13} and, consequently, Thomsen's $\boldsymbol{\delta}$ (delta) parameter.

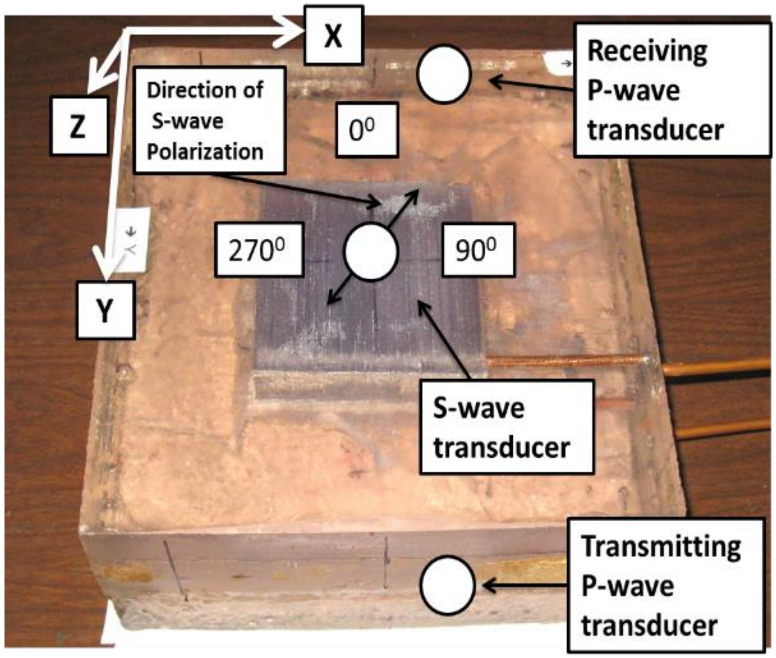

Figure 2.4: Annotated photograph of the ultrasonic transmission experimental setup for P-waves and S-waves (plan view), showing position of transducers. S-wave polarization ranged from 0^0 to 360^0 (measurement taken every 10^o interval)

For the scaled azimuthal CMP case (the reflection experiments), measurements were taken in only fully saturated conditions: at full air, water and glycerin saturations. The source-receiver configuration was designed to provide common-midpoint acquisition geometry. The measurements were repeated at every 15^o azimuth interval from azimuths 0^o to 180^o (90^o being the axis of symmetry). Minimum offset was 4cm (400m) and maximum offset was 22cm (2200m) with a 0.3cm (30m) offset interval. The transducer used for the CMP survey was a circular underwater transducer with 0.3 MHz dominant frequency. The diameter of underwater P-wave transducers was 6 mm. This set of experiments was conducted with the model (and source and receiver transducers) immersed in water (a marine environment). Figure 2.5 is a schematic diagram of the reflection (CMP) experimental setup.

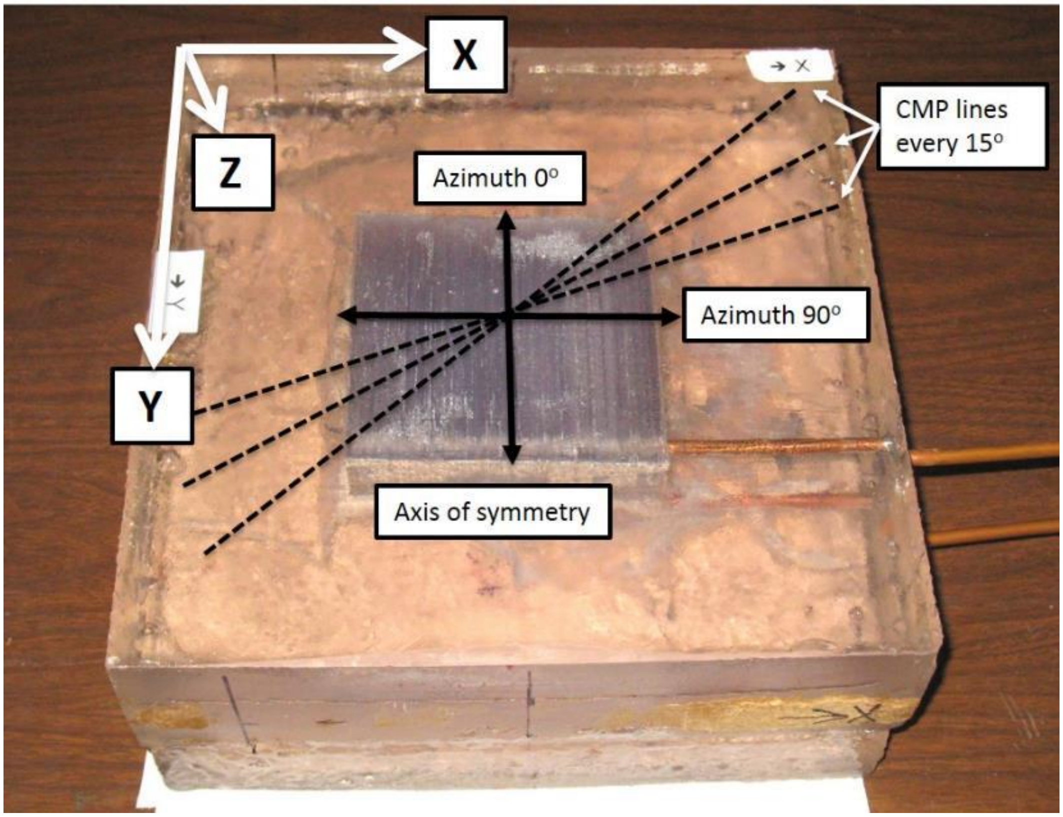

Figure 2.5: Schematic diagram of azimuthal reflection (CMP) experimental setup, showing position and azimuthal orientation of P-wave source-receiver transducer pairs (or CMP Lines). CMP lines were repeated for every 15° azimuth.

2.5 Experimental results and discussion

In addition to presenting our experimental results, we discuss error analysis and accuracy of experimental results. We analyse and compare the P- and S-wave velocities from the transmission experiments under different saturating conditions. Beyond acquiring the conventional ultrasonic transmission elastic wave velocities, P-wave NMO ellipses were obtained from the reflection experiments over the composite model impregnated with different fluids. Finally we analyse the stiffness coefficients and the anisotropic parameters ε and γ.

Following Stewart et al. (2013), we extracted and displayed velocity, elastic, and anisotropic properties for the fracture area only. Transit times and distances through the isotropic resin area were subtracted from the total times to create velocities of the fractures area.

2.5.1 Error analysis

To estimate velocity errors, we incorporated a methodology developed by Yin (1992) and Hornby (1998).

Measured velocities can be calculated from the following expression, (Hornby, 1998),

$$V = \frac{L}{t_m - t_t} \qquad (2.1)$$

where, V = velocity, L = measured length of the sample, t_m is the measured transit time and t_t is the transducer delay time.

Expanding equation 2.1 as a partial derivative,

$$\Delta V = \frac{dV}{dL}\Delta L + \frac{dV}{dt_m}\Delta t_m + \frac{dV}{dt_t}\Delta t_t \qquad (2.2)$$

Maximum absolute velocity error ΔV is

$$\Delta V = \frac{\Delta L}{t_m - t_t} + 2L\,\frac{\Delta t}{(t_m - t_t)^2} \qquad (2.3)$$

where, ΔL are variations in length/dimension measurements and Δt are errors in travel-time measurements.

Travel-time and length measurements were performed at least 10 times by two or three human operators during the course of this experiment. The reason for using more than one human operator was to help incorporate human (or interpretation) errors into our analysis. Time arrival picks on a digital oscilloscope can be slightly subjective, depending on the experience and knowledge of the operator. Variance and standard deviations were computed from these variations (both human and instrument variations) for every set of measurements.

For a particular travel-time measurement in the Y direction (Figure 2.6), travel time pick was at 138.93 µs, transducer delay was 0.34 µs, variance in travel-time pick (from 10 measurements) Δt_m = 0.61 µs, measured length was 297.93 mm and variance in length measurement ΔL = 1.13 mm. Figure 2.6 shows a digital oscilloscope display for the above named scenario. P-wave arrival was at 138.93 µs (on average from 10 measurements).

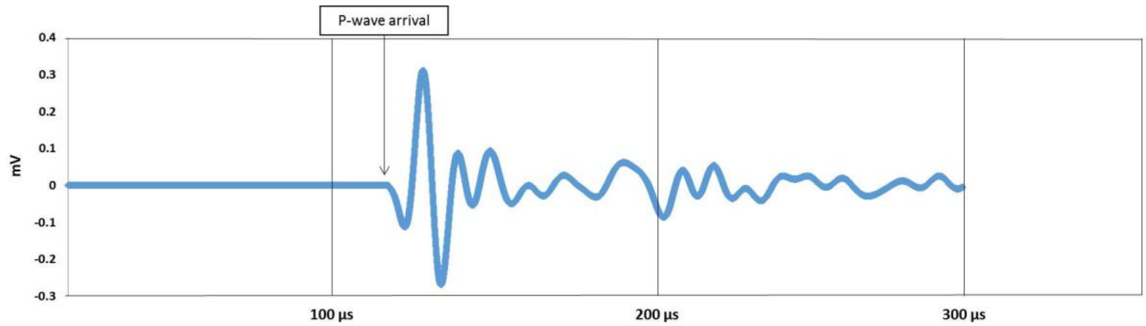

Figure 2.6: Digital oscilloscope display showing P-wave arrival (and corresponding transit time pick) in the X direction.

Using equation 2.3, we estimated maximum absolute velocity error for the above displayed oscilloscope results to be 27 m/s. Measured P-wave velocity was 2156 m/s. Therefore percentage error for this case scenario was ± 1.25%.

Velocity errors in this experimental study generally ranged from 1% to 1.5%.

2.5.2 *In-situ* (anisotropic) sample description

To create a context for the interpretation of the results displayed in this chapter, we present elastic and anisotropic properties of both the composite model and the embedded fractures. This is to help inform the reader of the *in-situ* (or undisturbed) elastic properties of our model prior to fluid saturation. In section 2.2, we measured physical properties of individual constituent materials before assemblage of the composite model. Here, we measure elastic properties of the already assembled model in order to inform the interpretation of results.

	V_P {Z} (m/s)	V_P {X} (m/s)	V_{S1} (m/s)	V_{S2} (m/s)	Density (g/cm^3)
Fracture region (polycarbonate sheets)	2155 ± 23.7	1564 ± 15.7	1210 ± 15.1	1073 ± 13.4	1.18
Composite model	2250 ± 28.0	1608 ± 16.0	1248 ± 15.6	1200 ± 15.0	1.20

Table 2.2: *In situ* physical properties of composite model and fracture area prior to fluid injection (air saturation case).

Physical properties of model after assemblage may differ slightly from properties of individual constituent materials due to the presence of air and impurities during the fabrication process. For example, velocity and density reduces for the polycarbonate sheets (fracture area) when embedded in the resin model (Table 2.1 and 2.2)

Isotropic Resin:

The generic stiffness matrix of an isotropic material is represented by the following:

$$\begin{pmatrix} \lambda + 2\mu & \lambda & \lambda & & & \\ \lambda & \lambda + 2\mu & \lambda & & & \\ \lambda & \lambda & \lambda + 2\mu & & & \\ & & & \mu & & \\ & & & & \mu & \\ & & & & & \mu \end{pmatrix} \qquad (2.4)$$

Using velocity and density values from Table 2.1, the isotropic stiffness matrix of the encompassing resin material is given below (in GPa):

$$\begin{pmatrix} \mathbf{7.80} & \mathbf{4.04} & \mathbf{4.04} & & & \\ \mathbf{4.04} & \mathbf{7.80} & \mathbf{4.04} & & & \\ \mathbf{4.04} & \mathbf{4.04} & \mathbf{7.80} & & & \\ & & & \mathbf{1.87} & & \\ & & & & \mathbf{1.87} & \\ & & & & & \mathbf{1.87} \end{pmatrix} \tag{2.5}$$

where, $\boldsymbol{\lambda} + \mathbf{2}\mu = \boldsymbol{\rho}\mathbf{V}_{\mathbf{p}}^{\mathbf{2}}$ and $\mu = \boldsymbol{\rho}\mathbf{V}_{s}^{\mathbf{2}}$.

Composite model and fractured region:

The fracture region and the composite model possess an effective HTI symmetry and the generic stiffness matrix of a polar anisotropic materials with horizontal axis of symmetry is listed below:

$$\begin{pmatrix} \mathbf{C_{11}} & \mathbf{C_{13}} & \mathbf{C_{13}} & & & \\ \mathbf{C_{13}} & \mathbf{C_{33}} & (\mathbf{C_{33} - 2C_{44}}) & & & \\ \mathbf{C_{13}} & (\mathbf{C_{33} - 2C_{44}}) & \mathbf{C_{33}} & & & \\ & & & \mathbf{C_{44}} & & \\ & & & & \mathbf{C_{55}} & \\ & & & & & \mathbf{C_{55}} \end{pmatrix} \tag{2.6}$$

The following elastic constants were derived from density and velocity measurements:

$$C_{11} = \rho Vp(x)^2 \tag{2.7}$$

$$C_{33} = \rho Vp(z)^2 \tag{2.8}$$

Because diagonal velocity (or transit-time) measurements were taken at an oblique angle (at 17^o on the XZ axes of the model), an angle-dependent version of Thomsen's equation was used to compute the stiffness parameter C_{13} and consequently Thomsen's $\boldsymbol{\delta}$ (delta) parameter:

$$C_{13} = \left[\frac{A-B}{4\sin^2\theta\cos^2\theta}\right]^{0.5} - C_{44} \tag{2.9}$$

where

$$A = [2\rho Vp_{zx}^2 - (C_{11} + C_{44})\sin^2\theta - (C_{33} + C_{44})\cos^2\theta\,]^2 \tag{2.10}$$

$$B = [(C_{11} - C_{44})\sin^2\theta - (C_{33} - C_{44})\cos^2\theta\,]^2 \tag{2.11}$$

The equation generally decomposes to the following when $\theta = 45^0$,

$$C_{13} = \left[\frac{\left(4Vp45(zx)^2 - C_{11} - C_{33} - 2C_{44}\right)^2 - (C_{11} - C_{33})^2}{4}\right]^{0.5} - C_{44} \tag{2.12}$$

$$C_{44} = \rho Vs1(z)^2 \tag{2.13}$$

$$C_{55} = \rho Vs2(z)^2 \tag{2.14}$$

where V_{S1} and V_{S2} correspond to fast and slow shear-wave velocities respectively.

Therefore, the initial derived polar anisotropic (HTI) stiffness matrix for the composite model is (in GPa):

$$\begin{pmatrix} \mathbf{3.10} & \mathbf{3.96} & \mathbf{3.96} & & & \\ \mathbf{3.96} & \mathbf{6.08} & \mathbf{2.34} & & & \\ \mathbf{3.96} & \mathbf{2.34} & \mathbf{6.08} & & & \\ & & & \mathbf{1.87} & & \\ & & & & \mathbf{1.73} & \\ & & & & & \mathbf{1.73} \end{pmatrix} \tag{2.15}$$

Transit times and distances through the isotropic resin area were subtracted from the total times to create velocities and consequently stiffness parameters of the fractures region, therefore, the initial derived polar anisotropic (HTI) stiffness matrix for the fractured area is (in GPa):

$$\begin{pmatrix} \mathbf{2.93} & \mathbf{3.72} & \mathbf{3.72} & & & \\ \mathbf{3.72} & \mathbf{5.58} & \mathbf{2.06} & & & \\ \mathbf{3.72} & \mathbf{2.06} & \mathbf{5.58} & & & \\ & & & \mathbf{1.76} & & \\ & & & & \mathbf{1.38} & \\ & & & & & \mathbf{1.38} \end{pmatrix} \tag{2.16}$$

2.5.3 Direct velocity measurements

In these experiments, velocities were calculated from direct transmission measurements. Figure 2.7 shows compressional wave velocities as a function of fluid saturation in the X (1) and Z (3) directions. Our observations indicate that P-wave velocities increased with increasing liquid saturation in both X and Z directions.

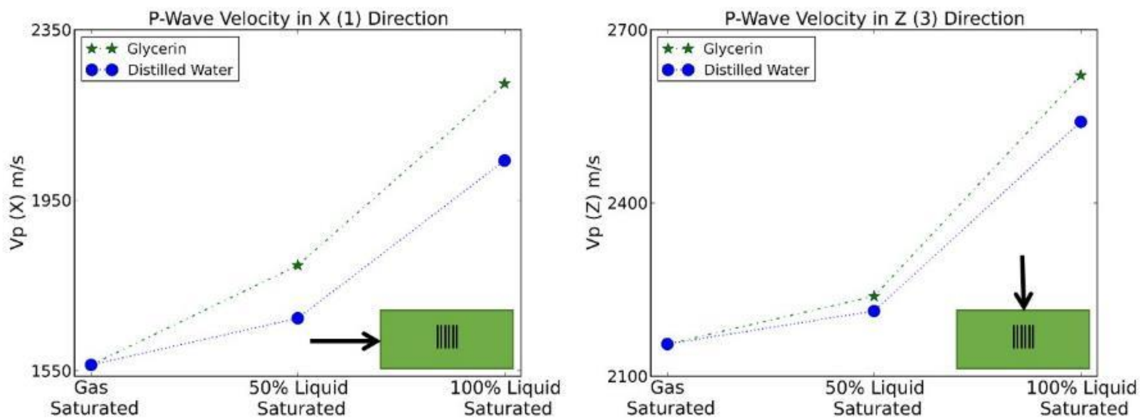

Figure 2.7: Compressional wave velocities as function of water saturation in: a) X direction (orthogonal to direction of fracture plane) and b) Z or vertical direction (parallel to direction of fracture plane). Errors in velocity measurement ranged from 1% to 1.5%.

Shear-wave splitting was observed and recorded in both initial (air saturated) and liquid saturated conditions (water and glycerin). Fast and slow shear-wave arrivals were picked from a digital oscilloscope. This process was repeated for all fluid saturation cases at every 10^o polarization angle. Figure 2.8 shows an oscilloscope seismogram plot (0^o polarization angle) for an air saturated case, from this display; we are able to pick arrivals of P- and S-waves. Although S-wave transducers were used, P-wave arrivals can be noticed on the seismogram display. This P-wave arrival was later muted after careful characterization of both P- and S-waveforms.

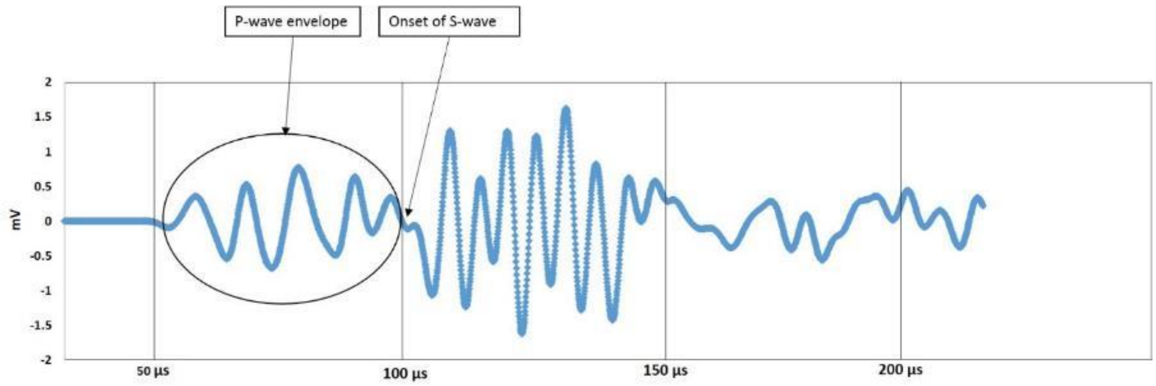

Figure 2.8: Shear-wave seismogram display, at shear-wave polarization angle (ϕ) of 0°. (Polarization angles 0^0 is parallel to the fracture plane, while 90^0 is perpendicular).

Figure 2.9 shows two oscilloscope waveforms, one at polarization of 0° (same waveform as Figure 2.8) and the other at 90°, fast shear-waves can be picked from the 0° polarization and slow shear-waves can be picked from the 90° polarization (axis of symmetry). Notice the delay time between fast (S1) and slow (S2) shear-waves. This process was repeated at different fractions of saturation during the course of the experiment.

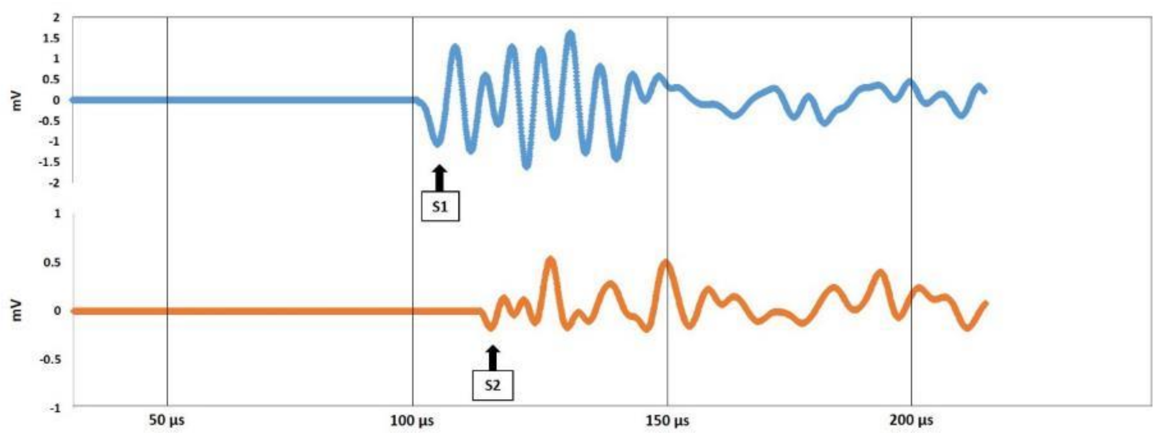

Figure 2.9: Shear-wave seismogram display after P-wave mute, showing shear-wave polarization angles (ϕ) of 0° (Blue) and 90° (Brown). Polarization angles 0^0 are parallel to the fracture plane, while 90^0 are perpendicular.

Figure 2.10 is a plot of fast and slow shear-wave velocities estimated from oscilloscope results. Note that slow shear-wave velocity decreases more (than fast shear-wave velocity) with increasing liquid saturation. At 50% saturation, the difference between water and glycerin starts to become apparent. Glycerin (more viscous than water) shows a higher net effective decrease when compared to water. Note also that fast shear-wave velocities seem independent of type of the saturating fluid. Values of fast shear velocities seem similar in all saturating conditions.

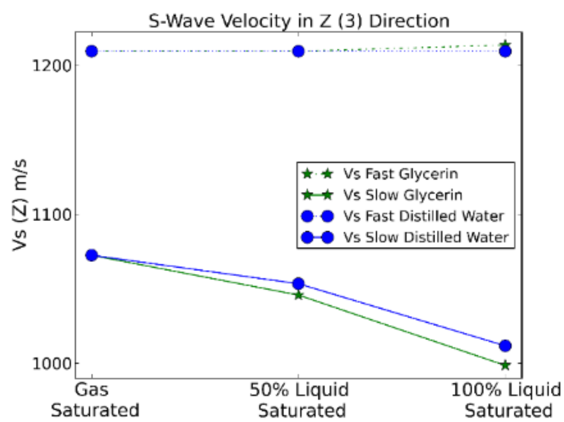

Figure 2.10: Fast and slow shear-wave velocities as function of liquid saturation in the Z-direction. Errors in velocity measurement ranged from 1% to 1.5%.

2.5.4 Azimuthal P-wave NMO analyses

The second set of experiments (also referred to as the reflection experiments) was designed to simulate wide-azimuth surveys over a fractured reservoir. Circular underwater transducers were used. Group velocities were likely measured because of the size of the source and receiver underwater sensors relative to the thickness of the model, following Dellinger and Vernik (1994). CMP type (reflection) measurements were acquired over the composite model. Figure 2.11 shows a schematic of the underwater experimental setup.

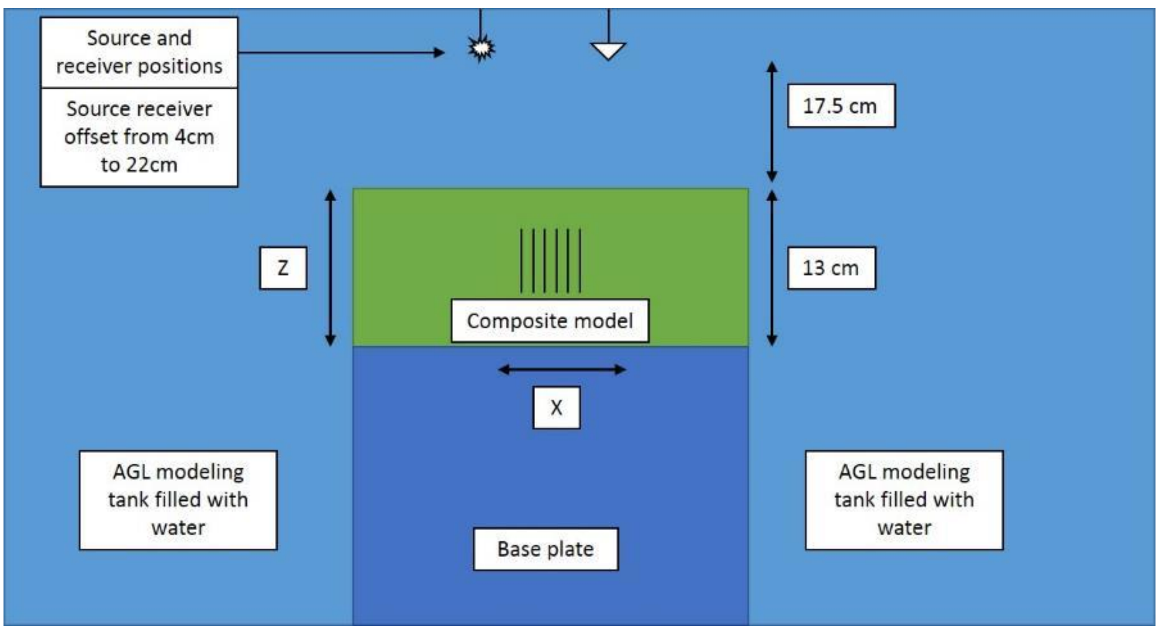

Figure 2.11: Schematic diagram of underwater experimental setup (min source-receiver offset = 4cm, max source-receiver offset = 22cm offset interval = 0.3cm).

Figure 2.12 shows three CMP gathers with the source-receiver azimuths 15°, 30°, and 45°, respectively, before water injection (90° is the axis of symmetry and 0° is parallel to the plane of fractures).

Reflectivity modeling for the composite model is documented in Appendix A. This reflectivity modeling helps identify events corresponding to the tops and bases of the composite model and the fracture area.

These CMP gathers have undergone a conventional noise and multiple attenuation processing sequence. This is to help ensure the removal of direct arrivals, multiples and random noise from our model data.

From Figure 2.12, we can observe significant changes in moveout of the reflected events from the fracture zone.

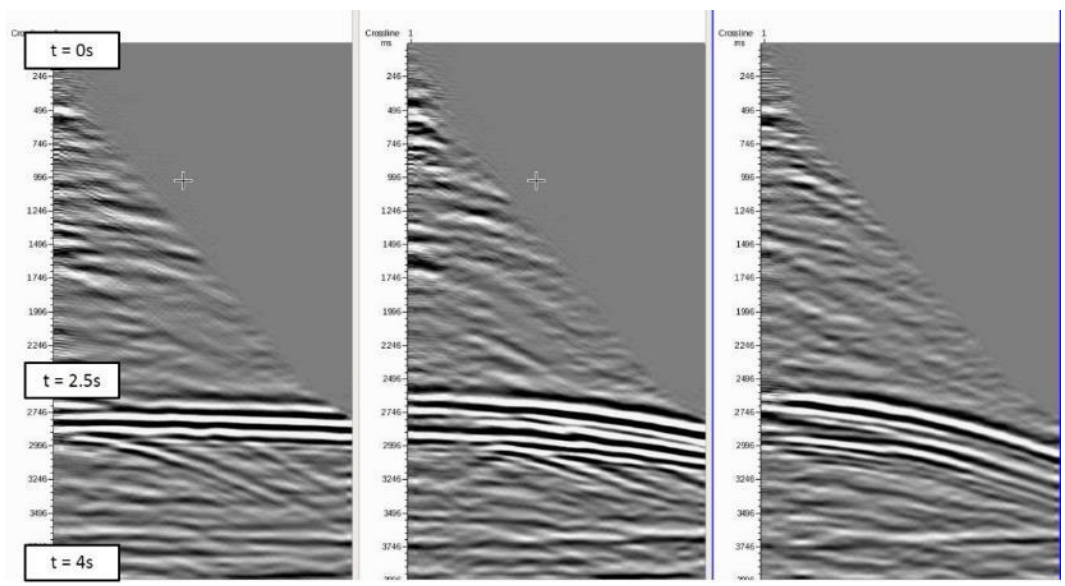

Figure 2.12: CMP gathers (air-saturated condition) with source-receiver azimuths of 15^{o}, 30^{o} and 45^{o}, respectively (min offset = 4cm, max offset = 22cm offset interval = 0.3cm).

After water and glycerin saturations, these azimuthal CMP surveys were repeated. Figure 2.13 shows NMO corrected CMP gathers (azimuth 30^{0}) with air and water saturants. Also, some differences in amplitude characteristics seem to be visible after water saturation.

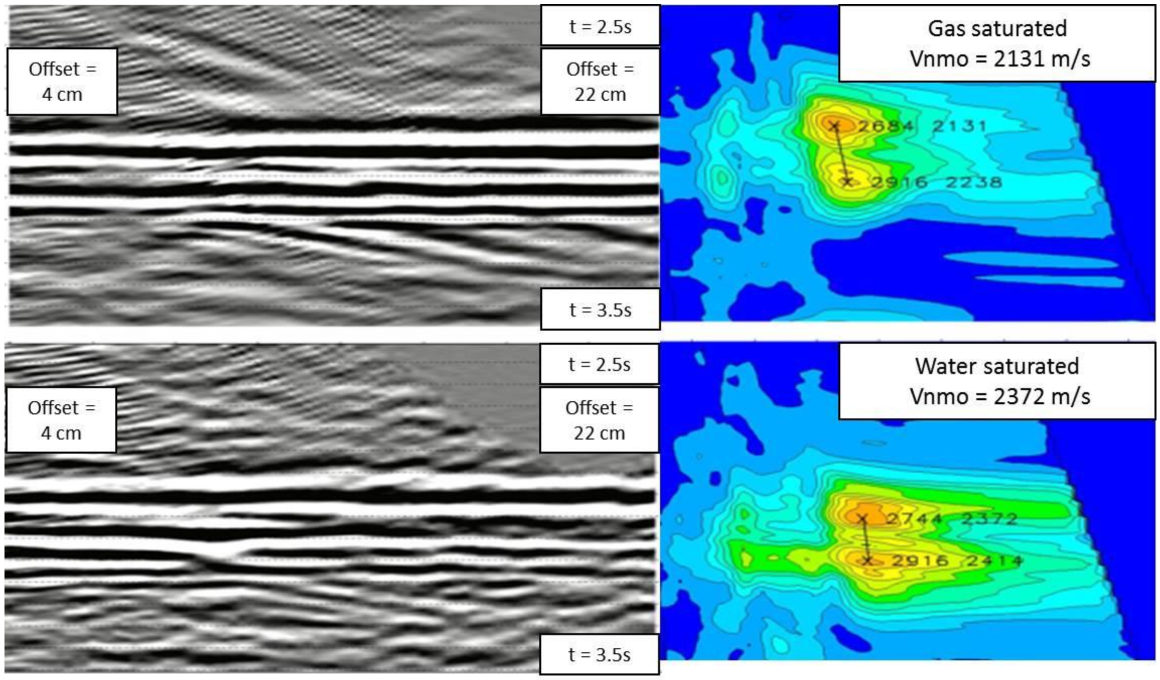

Figure 2.13: NMO-corrected CMP gathers (azimuth = 30°) showing stacking velocity semblance plot and time-velocity pairs: a) at gas-saturated condition, and b) at water-saturated condition.

We also observe not only a difference in NMO velocity with fluid saturation but a difference in the trend of stacking velocity as a function of azimuth in different saturating conditions. Figure 2.14 shows NMO ellipses from CMP surveys on the composite model when impregnated with different fluids.

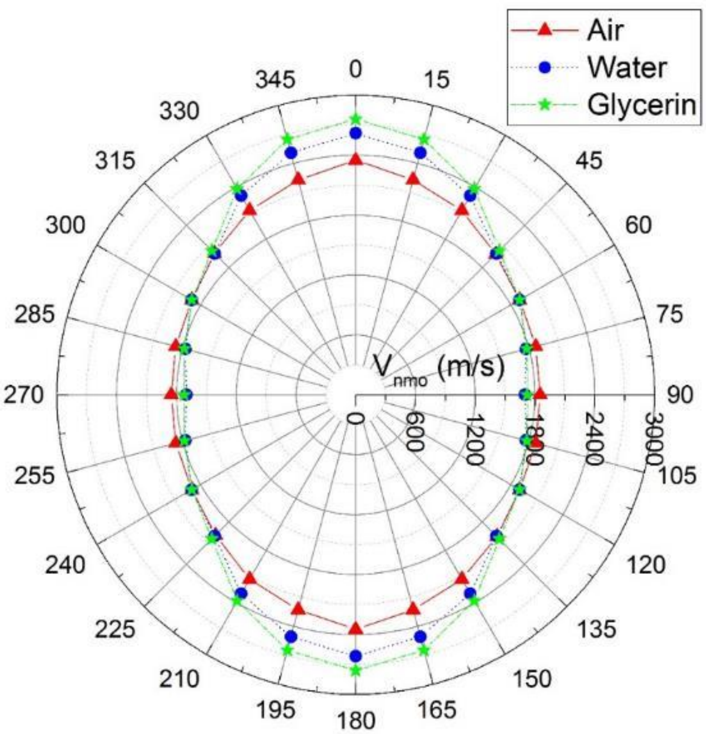

Figure 2.14: NMO ellipses under different saturating conditions. Cracks are aligned at 0°-180° axes (axis of symmetry is 90°).

2.5.5 Stiffness coefficients and anisotropic parameters

Elastic constants were calculated from density and velocity measurements. Thomsen's (1986) weak elastic anisotropic expressions were used to estimate anisotropic parameters. Figure 2.15 shows compressional wave dependent stiffness coefficients as a function of water and glycerin saturations. Note that parameters C_{11} and C_{33} show an increasing trend with increasing fluid viscosity. Observe that including denser and less compressible fluids in the system contributes to a less compliant composite material. Figure 2.16 shows a plot of shear-wave dependent coefficients.

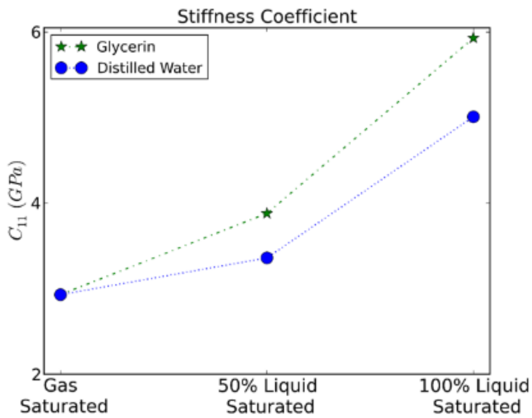

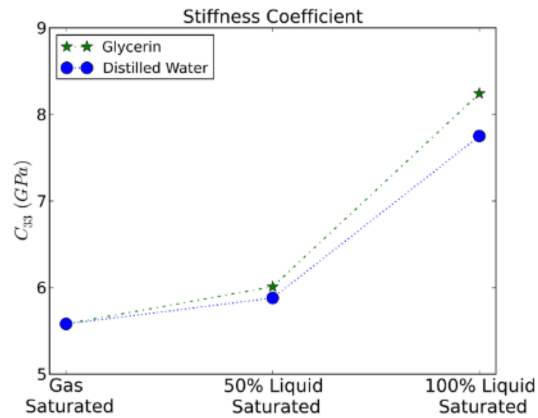

Figure 2.15: P-wave dependent stiffness coefficients as functions of liquid saturation: a) C_{11} b) C_{33}

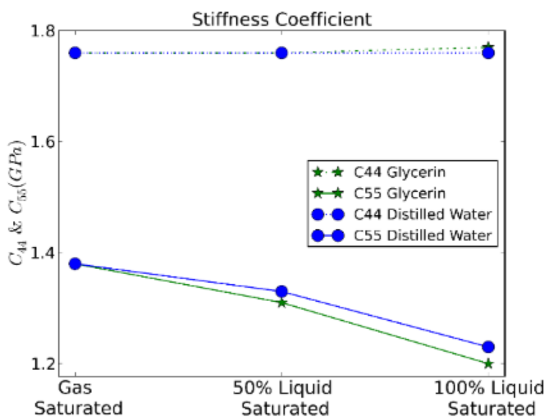

Figure 2.16: S-wave dependent stiffness coefficients as functions of liquid saturation (C_{44} and C_{55})

On computing anisotropic parameters, we observed a decrease in ε and an increase in the shear-wave splitting parameter γ. Figures 2.17 and 2.18 are plots of anisotropic parameters as functions of liquid saturation; observe the opposite trends between ε and γ.

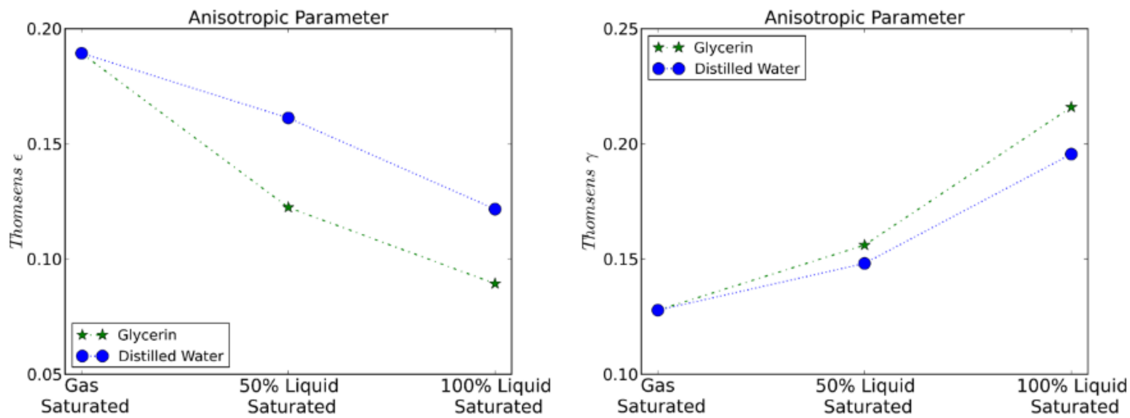

Figure 2.17: Anisotropic parameters as functions of liquid saturation (Thomsen's ε & γ).

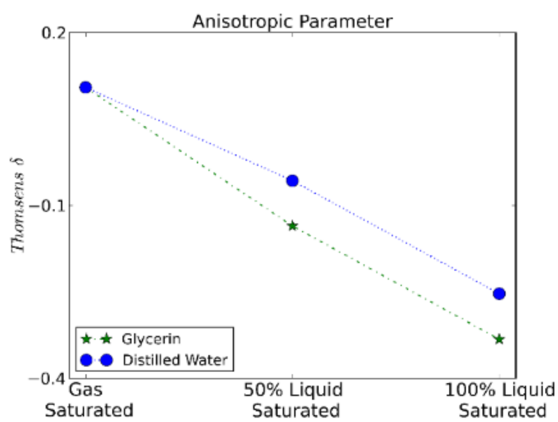

Figure 2.18: Thomsen's Delta as a functions of liquid saturation.

2.6 Conclusions

This experimental study has investigated the influence of different saturating fluids on anisotropy in an azimuthally anisotropic medium.

Our results show a relation between fluid type and the magnitude of shear-wave splitting. Fluid substitution affects the density of a medium which in turn affects physical properties such as P- and S-wave velocities as well as seismic birefringence.

Within the limit of our experiments, we also found that the trend of azimuthal NMO velocities is influenced by the nature of the saturating fluid.

Based on these results the following observations can be made:

1) Shear-wave dependent elastic modulus C_{55} is more sensitive to injected saturants than C_{44}. For compressional wave-dependent elastic moduli, C_{33} is more sensitive to fluid saturation than C_{11}.
2) Compressional wave-dependent stiffness coefficients C_{11} and C_{33} seem to be better overall fluid-type discriminators when compared to shear dependent elastic moduli.
3) The nature of the saturating fluid has a direct influence on shear-wave splitting as well as on the trend of azimuthal NMO. This is due in part to the effects of changes in density and fluid bulk modulus.
4) Slow shear-waves are more sensitive to fluid saturation than fast shear-waves.
5) A decrease in anisotropic parameter ε was observed as we increased water and glycerin saturations. The reverse was the case for anisotropic parameter γ.

6) Anisotropic parameters ε and γ seem to be powerful tools for characterizing the amount of fluid saturation as well the distinction of fluid types in a cracked medium.

Even though theoretical predictions (Sayers 2002; Berryman 2005; Galvin et al. 2007) as well as experimental and field observations have shown relationships between fluid types and shear-wave birefringence, this newly emerging field still requires quantitative analysis to optimally use shear-wave birefringence as a viable DHI. Experimental physical-modeling work can be a significantly useful tool to increase our understanding and gain better perception into the complex or seemingly convoluted behavior of elastic waves in anisotropic fractured media.

Acknowledgements

This physical modeling project was made possible by the financial support of Allied Geophysical Laboratories, University of Houston. The authors are grateful to Dr. Evgeny Chesnokov for his advice and Dr. Robert Wiley for his assistance during the experiments.

2.7 References

Angerer, E., S. Crampin, X. Li, and T. L. Davis, 2002, Processing, modelling and predicting time-lapse effects of overpressured fluid-injection in a fractures reservoir. Geophysical Journal International. **149**, 267 - 280.

Berryman, J., 2005, Fluid effects on shear-waves in finely layered porous media. Geophysics. **70** (2), N1 - N15.

Crampin, S., 1985, Evaluation of anisotropy by shear-wave splitting. Geophysics. **50** 142-152

Dellinger, J, A., and L, Vernik., 1994, Do traveltimes in pulse-transmission experiments yield anisotropic group or phase velocities? Geophysics. **59**, 1774-1779

Ebrom, D. A., R. H. Tatham, K. K. Sekharan, J. A. McDonald, and G. H. F. Gardner, 1990, Hyperbolic transmission analysis of first arrivals in an azimuthally anisotropic medium: A physical modeling study. Geophysics. **55**, 185–191.

Eshelby, J.D., 1957, The Determination of the Elastic Field of an Ellipsoidal Inclusion, and Related Problems. Proceedings of the Royal Society of London. **241**, 376-396

Galvin R.J., Gurevich B. and Sayers C.M. 2007. Fluid-dependent shear-wave splitting in a poroelastic medium with conjugate fracture sets. Geophysical Prospecting. **55**, 333 - 343.

Gueguen, Y., and J, Sarout, 2011. Characteristics of anisotropy and dispersion in cracked medium. Tectonophysics. **503**, 165 – 172.

Hornby, B.E., 1998. Experimental laboratory determination of the dynamic elastic properties of wet, drained shales. Journal of Geophysical Research. **103** (B12), 29945–29964.

Hudson, J. A., 1980, Overall properties of a cracked solid. Mathematical Proceedings of the Cambridge Philosophical Society. **88,** 371-384,

Hudson, J. A., 1981, Wave speeds and attenuation of elastic waves in material containing cracks. Geophysical Journal of the Royal Astronomical Society. **64,** 133–150.

Lynn, H.B., and L, Thomsen., 1990, Reflection shear-wave data collected near the principal axes of azimuthal anisotropy. Geophysics. **55**, 147-156

Mueller, M., 1992, Using shear-waves to predict lateral variability in vertical fracture intensity. The Leading Edge. **33**, 29-35

Potters, J.H.H.M., H.J.J. Groenendaal., S.J. Oates., J.H. Hake., and A.B. Kalden., 1999. The 3D shear experiment over the Natih field in Oman. Reservoir geology, data acquisition and anisotropy analysis. Geophysical Prospecting. **47**, 637 - 662.

Rathore J.S., Fjaer E., Holt R.M. and Renlie L. 1995. P- and S-wave anisotropy of a synthetic sandstone with controlled crack geometry. Geophysical Prospecting. **43**, 711-728.

Sayers C.M. 2002. Fluid-dependent shear-wave splitting in fractured media. Geophysical Prospecting. **50**, 393 - 401.

Schoenberg, M., 1980, Elastic wave behavior across linear slip interfaces: The Journal of the Acoustic Society of America. **68**, 1516–1521.

Schoenberg M., 1983, Reflection of elastic waves from periodically stratified media with interfacial slip. Geophysical Prospecting. **31**, 265–292.

Stewart, R.R., J.E. Gaiser., R.J. Brown., D.C. Lawton, 2002. Converted-wave seismic exploration: Methods. Geophysics. **67**, 1348-1363

Stewart, R.R., J.E. Gaiser., R.J. Brown., D.C. Lawton, 2003. Converted-wave seismic exploration: Applications. Geophysics. **68**, 40-57

Stewart, R.R., N. Dyaur., B. Omoboya., J. J. S. de Figueiredo., M. Willis., and S. Sil, 2013. Physical modeling of anisotropic domains: Ultrasonic imaging of laser-etched fractures in glass. Geophysics. **78**, 11-19

Tatham, R. H., M. D. Matthews, K. K. Sekharan, C. J.Wade, and L. M. Liro, 1992, A physical model study of shear-wave splitting and fracture intensity. Geophysics. **57**, 647–652

Thomsen, L.,1986, Weak elastic anisotropy. Geophysics. **51**, 1954-1966.

Thomsen, L., 1995, Elastic anisotropy due to aligned cracks in porous rock. Geophysical Prospecting. **43**, 805–829.

Tillotson P., Chapman M., Best A.I., Sothcott J., McCann C., Shangxu W. and Li X.Y. 2011. Observations of fluid-dependent shear-wave splitting in synthetic porous rocks with aligned penny-shaped fractures. Geophysical Prospecting. **59**, 111–119.

Tsvankin, I., 1997, Reflection moveout and parameter estimation for horizontal transverse isotropy. Geophysics. **62**, 614-629.

Van der Kolk, C.M., W. Guest and J.H.H.M. Potters., 2001. The 3D shear experiment over the Natih field in Oman: the effect of fracture-filled fluids on shear propagation. Geophysical Prospecting. **49**, 179 - 197.

Yin, H., 1992. Acoustic velocity and attenuation of rocks: isotropy, intrinsic anisotropy, and stress-induced anisotropy. Ph.D. dissertation. Stanford University, Palo Alto, CA, USA.

CHAPTER THREE

Dynamic elastic properties of a layered orthorhombic physical model

Bode Omoboya[1], J.J.S. de Figueiredo[2], Nikolay Dyaur[1] and Robert R. Stewart[1]

[1]- University of Houston, Department of Earth and Atmospheric Sciences, Houston-Texas, USA: Email: bodeomoboya@gmail.com, nidyaur@gmail.com and rrstewart@uh.edu

[2]-Federal University of Para, Geophysics Department & National Institute of Petroleum Geophysics (INCT-GP), Belém-Pará, Brazil: Email: jadsom@ufpa.br

3.1 Summary

Studies of orthorhombic seismic anisotropy are becoming increasingly widespread, as many sedimentary rocks are considered to possess orthorhombic symmetry, due to combination of layering, stress, and fractures. Here, we study the effect of uniaxial normal stress on a layered but orthorhombic medium (a stack of intrinsically orthorhombic phenolic boards). The experiment was designed to simulate sedimentary reservoir rocks deposited in layers with inherent orthotropic symmetry and under the influence of stress due to overlying sediments. The main goal is to measure elastic anisotropies with increasing uniaxial stress. The phenolic boards were coupled with a pressure device and uniaxial normal stress was increased and velocity measurements were repeated. Results show a general increase in all directly measured velocities with stress. Increase in compressional-wave and shear-wave velocities ranged from 4% to 10% in different

directions as a function of increasing uniaxial stress. Most elastic stiffness coefficients (with a few exceptions) increased with stress. Conversely, most elastic compliance coefficients decreased with stress. Anisotropic parameters (extension of Thomsen's parameters for orthorhombic symmetry) generally diminished or remained constant with increasing uniaxial stress. We observed anisotropic behavior a priori to both orthorhombic and VTI symmetries in different principal axes of the model. Polar anisotropy behavior is due primarily to layering and tends to increase with uniaxial stress. Certain direct velocity measurements and consequently elastic parameters C_{55} and C_{66} appear more sensitive to changes in stress, revealing an orientation within the fabric of the composite model. Also, anisotropic parameters suggest an inherent orthotropic property of the composite model.

3.2 Introduction

A combination of parallel vertical fractures, regional stress, and a background horizontal layering (common in shales) can form orthorhombic symmetry (Sayers, 2002). Shales account for up to 80% of the drilled section in the oil and gas industry (Sarout et al., 2006). Regional stress is also a common geologic phenomenon responsible for azimuthal anisotropy (Sayers, 2002). These two geologic phenomena (horizontal layering/stratification and regional stress) are widespread, thus, orthorhombic symmetry may be a realistic anisotropic earth model for reservoir characterization. This chapter considers the effect of normal uniaxial stress on velocity, as well as the general full dynamic elastic properties of a layered orthorhombic medium.

Studies of elastic properties on shales such as those of Jones and Wang (1981) and Hornby (1998) gave useful insights as well as set precedence for measurement of dynamic elastic properties under different stress conditions.

Many examples of the relationship of elastic properties of shales under different types of stress conditions have been reported in literature. Previous measurements by Pervukhina and Dewhurst (2008) showed the relationship between anisotropic parameters and mean effective stress in transversely isotropic shale core samples. Sarout et al. (2006) explored anisotropic properties of Callovo-Oxfordian shales under stress. Far et al. (2014) conducted experiments to explore connections between fracture compliance and uniaxial normal stress in a synthetic fracture physical model.

Podio et al. (1968) investigated dynamic elastic properties of Green River shales under uniaxial stress. We extend the approach of Podio et al. (1968), to slightly more complicated rock symmetry. In our experimental study, we consider a set of layered synthetic orthorhombic materials. Since real intrinsically orthorhombic rocks samples are rare in the laboratory (most exist only in *in-situ* conditions), measurements of dynamic elastic properties of orthotropic rock samples are by consequence rare or non-existent in literature. As a result, we have developed an alternative; physical modeling with synthetic or representative rock samples. Although with some natural limitations, physical modeling has proved to be a useful method of investigating physical phenomena that would otherwise be difficult or impossible to carry out in the field or in real rock samples (Stewart et al, 2013).

Rathore et al. (1995) measured acoustic anisotropy and observed shear-wave splitting in novel synthetic sandstone with well-known fracture geometry and orientation. Ebrom et al. (1990) and Tatham et al. (1992) explored seismic response in an effectively anisotropic medium using polycarbonate sheets. These types of experimental studies would have been hitherto impossible to adequately simulate and calibrate in real rocks or from seismic data.

3.2.1 Nature of phenolic model

Phenolic CE is an industrial laminate which possesses a unique orthogonal weave of fibers (Cheadle et al, 1991). This unique wave of fibers makes phenolic ideal for measuring orthorhombic anisotropy in a physical modeling setup. In this experiment, we have used phenolic sheets for the sole purpose of increasing and decreasing pressure on the model so we can measure the evolution of elastic properties as pressure changes.

Our assembled medium is made up of 55 phenolic slabs or boards coupled together with a pressure apparatus. Each board is about 1.8 mm thick. Figure 3.1 is a photograph of the composite model showing all dimensions and principal axes.

Phenolic CE is an industrial laminate with intrinsic orthorhombic symmetry. The peculiar intrinsic anisotropic property is mainly due to an orthogonal weave of fibers within the material. Figure 3.2 is a close-up photograph of the physical model/phenolic material showing orthogonal weave of microfibers that contributes to orthorhombic anisotropy.

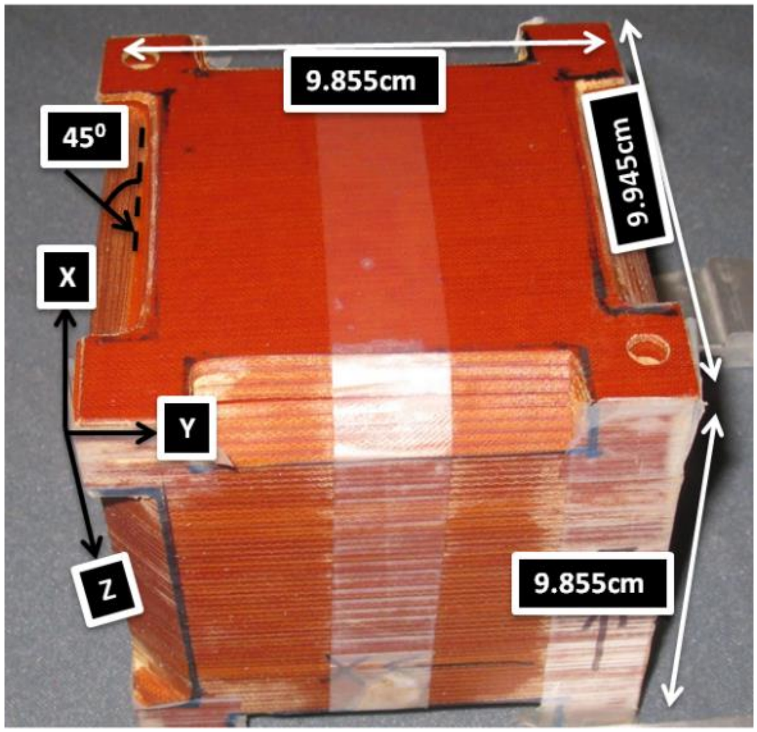

Figure 3.1: Photograph of physical model.

The composite model has the following physical properties in the initial stress state (0.05 MPa):

Density = 1.3g/cm^3, V_P (X-Direction) = 3097m/s, V_P (Y-Direction) = 2786m/s, V_P (Z-Direction) = 2049m/s (Directions with reference to Figure 3.1).

Fast shear-wave velocities ranged from 1143m/s to 1659m/s, while slow shear velocities ranged from 1058m/s to 1133m/s in all axes.

Diagonal P-wave velocities ranged from 2231m/s to 2375m/s in all axes and faces of the composite model.

Velocity errors ranged from 0.5% to 1%.

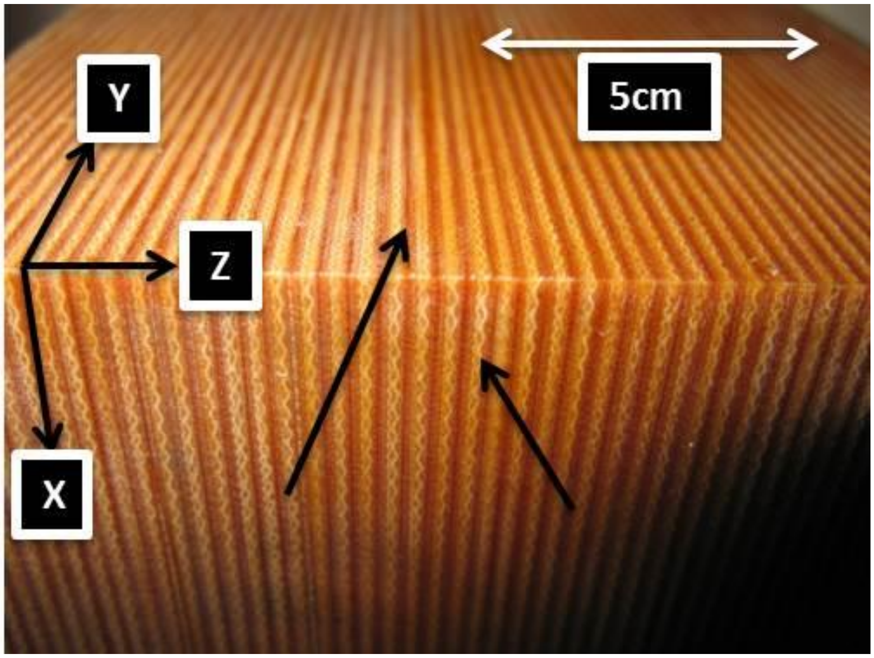

Figure 3.2: Photograph of physical model/phenolic material showing orthogonal weave of microfibers that constitute orthotropic anisotropy.

3.2.2 Main objectives

The main objectives of this experiment are as follows:

1) To assess the evolution of velocity anisotropy under uniaxial normal stress
2) To explore the effect of stress on anisotropy and dynamic elastic properties in an inherently anisotropic medium.
3) To explore which physical phenomena (horizontal layering/stratification or vertical fractures) dominates the character of anisotropy as uniaxial stress increases.

Results show anisotropic behavior ascribable to both orthorhombic symmetry and VTI symmetry due to layering. Anisotropic behavior attributable to polar anisotropy tends to increase with increasing uniaxial stress in the Z (vertical) direction.

3.3 Experimental setup

This physical modeling experiment was designed to simulate earth-like intrinsically anisotropic rocks buried in layers and so under the influence of pressure from overburden sediments. Scaled ultrasonic seismic measurements were taken in radial, sagittal, and traverse directions on all block faces, travel times were picked directly from a digital oscilloscope and used as input for calculation of compressional and shear-wave velocities, dynamic elastic properties as well as anisotropic parameters. Uniaxial normal stress was gradually increased and all measurements were repeated. Figure 3.3 is a schematic of the experimental setup showing the direction of application of stress, as well as positioning of transducers and strain gauges.

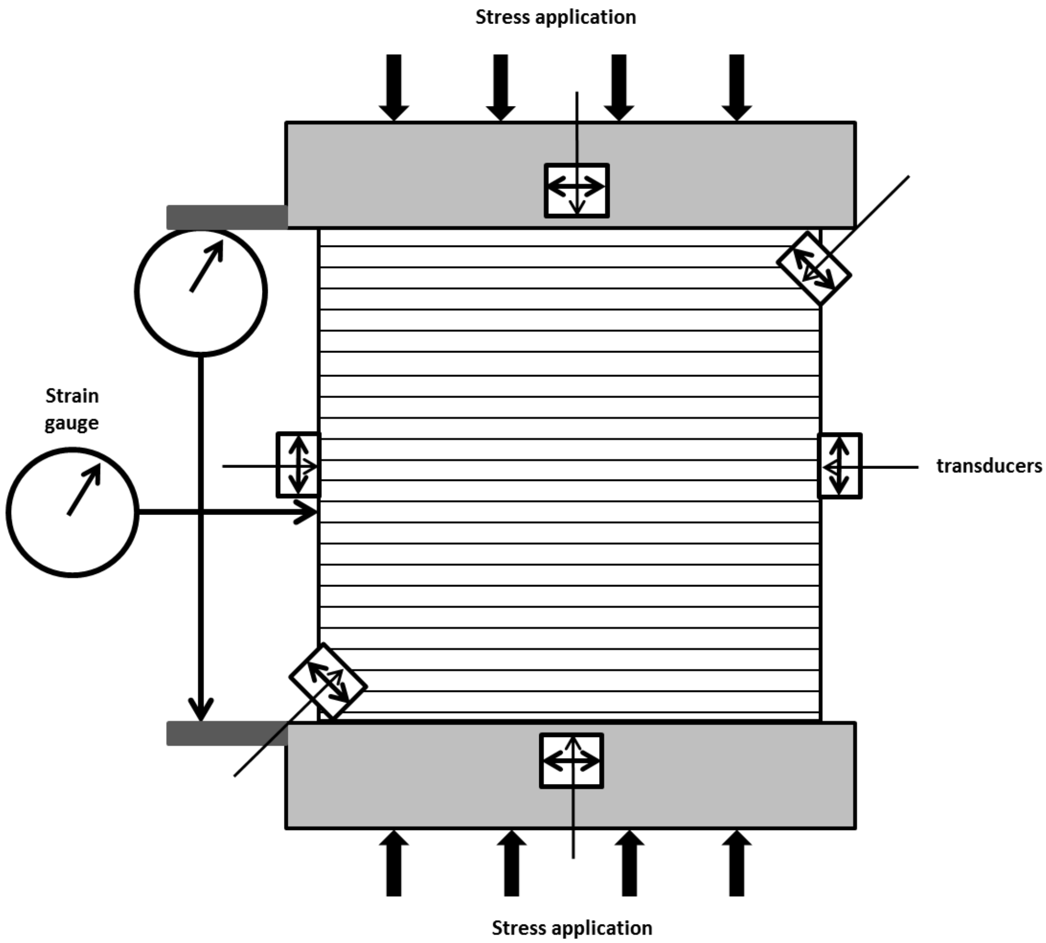

Figure 3.3: Schematic of experimental setup showing direction of application of stress and positions of ultrasonic transducers and strain gauges. Both P-wave and S-wave transducers were used.

In a seismic physical modeling experiment, an attempt is made at estimating the seismic response of a geologic model by measuring the reflected or transmitted wave field over the scaled model (Ebrom and McDonald, 1994). The scaling is on travel time and consequently wavelength but all other wave attributes such as velocity remain intact.

3.3.1 Sample preparation

The 55 phenolic boards were cut to size and bound together with the help of a pressure device. The pressure device was fitted with pressure and strain gauges. The boards were cut or designed to form an approximate cube shape. This was to ensure that the diagonal measurements in all axes would be 45 degrees (approximately). The principal axes of the composite model were labelled X, Y, and Z; with Z being the direction perpendicular to layering (or sedimentation/stratification in a real earth case). The Z direction is also the direction of much interest to exploration geophysics. Some publications label principal axes as 1, 2, and 3 axes), X direction = 1, Y direction = 2, and Z direction = 3. The thickness of the phenolic boards ranged from 1.6 mm to 1.9 mm. Before the commencement of travel time measurements, density measurements were taken and a strain test was conducted mainly to test the elastic strength of the composite model. Figure 3.4 shows a stress strain curve for the model. Figure 3.4 also shows the trend of the uniaxial loading and unloading cycle of the model. From the trend of uniaxial loading and unloading, we observe an irregular strain during the unloading process. Also, the material never seems to return to the initial strain state (zero strain) after complete unloading.

After the strain test, 7 sets of measurements were taken (black arrows in Figure 3.4) to be used in the experiment. Uniaxial stress was increased from 0.05MPa to 0.5MPa and travel time measurements were taken.

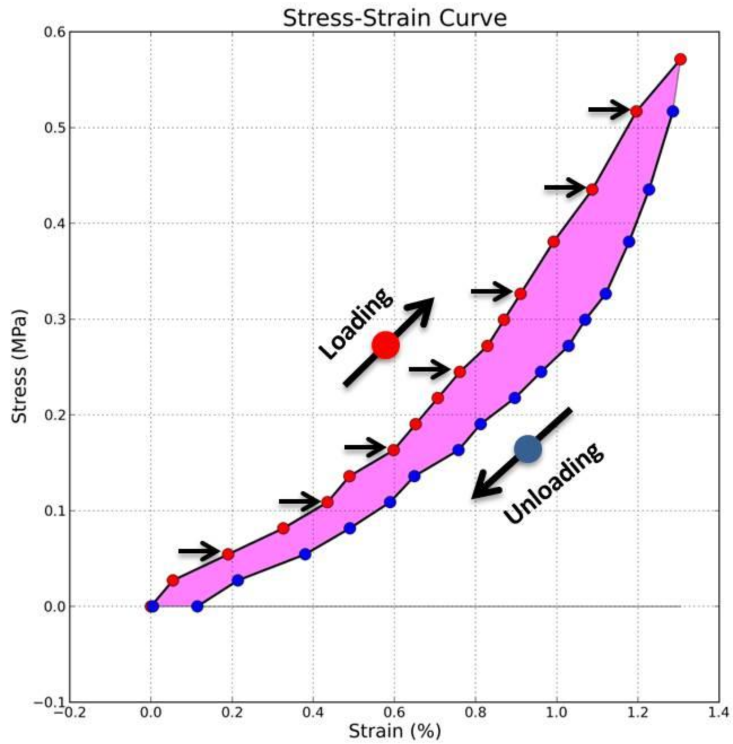

Figure 3.4: Stress-Strain curve for layered phenolic model showing trend of uniaxial loading and unloading. Black arrows indicate chosen values for velocity, measurements.

3.3.2 Measurement Technique

An ultrasonic transmission technique (pulse-echo technique) was used throughout the experimental study. Our ultrasonic measurement system included a 5077PR pulser/receiver, an HS-4 (50 MHz) digital oscilloscope, low noise amplifiers and P- and S-wave piezoceramic transducers of 0.1 MHz central frequency. We used 100 KHz (0.1MHz) compressional and shear-wave transducers to ensure seismic wavelength was at least 10 times the thickness of each phenolic sheet.

The wavelength of the compressional wave was measured at ~30 mm (thickness of phenolic board ~1.8 mm). In all measurements (both compressional and shear-wave), $\boldsymbol{\lambda} \gg \boldsymbol{H}$ ($\boldsymbol{\lambda}$ is seismic wavelength and $\boldsymbol{H}$ is thickness of the phenolic sheets). This was to ensure an effective seismic response from the whole model rather than scattering between layers. The source and receiver transducers were placed on opposing sides for a pulse transmission measurement. The direction of polarization of the shear transducer was varied from 0^o to 180^o (in the Z direction only) and measurements were taken every 10^o interval. In each case (all directions), 0^o was shear polarization oriented parallel to the bedding plane and 90^o was polarization perpendicular to bedding plane. Compressional and shear-wave arrivals were picked directly from seismograms produced by the AGL scaled ultrasonic system with an accuracy of ± 0.1µs. In this experiment, velocities were computed directly from travel time measurements. The diameter of the transducers used (both compressional and shear) was about 4cm. Transducer response has also been well studied for directivity and delay time. Time arrival measurements were taken in 3 principal axes, Z (3), X (1), and Y (2). Diagonal velocity measurements were also taken at 45^o in ZY axes and at two other slightly oblique angles; 44.4^o in ZX and 46.6^o in XY, this is due to the fact that the composite model is not a perfect cube (but a cuboid - Figure 3.1). The dimensions of the model are; 9.855 cm X 9.945 cm X 9.855 cm. As a result, angle-dependent velocities were used across ZX and XY axes to obtain diagonal stiffness coefficients C_{12} and C_{23}. The time and distance scaling factor is 1:10000. All model construction as well as ultrasonic measurements were carried out at the Allied Geophysical Laboratories (AGL) at the University of Houston.

3.4 Experimental results

We present here experimental results ranging from direct velocity measurements to dynamic elastic properties (stiffness and compliance). We also quantify anisotropies in terms of anisotropic parameters. Error analysis is also discussed. Shear-wave seismograms were plotted as a function of polarization angles in different stress regimes are also presented (Z direction).

3.4.1 Error analysis

To estimate velocity errors, we incorporated a methodology developed by Yin (1992) and Hornby (1998).

Measured velocities can be calculated from the following expression, (Hornby, 1998),

$$V = \frac{L}{t_m - t_t} \tag{3.1}$$

where, V = velocity, L = measured length of the sample, t_m is the measured travel-time and t_t is the transducer delay time.

Expanding equation 3.1 as a partial derivative,

$$\Delta V = \frac{dV}{dL}\Delta L + \frac{dV}{dt_m}\Delta t_m + \frac{dV}{dt_t}\Delta t_t \tag{3.2}$$

Maximum absolute velocity error ΔV is

$$\Delta V = \frac{\Delta L}{t_m - t_t} + 2L\,\frac{\Delta t}{(t_m - t_t)^2} \tag{3.3}$$

where, ΔL are fluctuations in length/dimension measurements and Δt are fluctuations in travel-time measurements.

Travel-time and length measurements were performed at least 10 times by two operators during the course of this experiment. Average values as well as fluctuations (variance and standard deviation) were recorded for every set of measurement.

Using equation 3.3, maximum absolute velocity error ranged from ± 0.5% to

± 1.5% for all experimental measurements.

3.4.2 Direct velocity measurements

Figure 3.5 shows compressional wave velocities as a function of uniaxial stress (proxy for overburden pressure) in all measured directions. Not surprisingly, P wave velocities increased with stress in all directions. This is due to a gradual closure of space between layers in the model. P-wave velocity in the Z direction is significantly lower than in X and Y direction due to laminate finishing of the phenolic model used. Diagonal P-wave measurements also show an overall increase with stress. Figure 3.5b also shows phase velocities in diagonal directions (ZX = 44.4^{o}, ZY = 45^{o} and XY= 46.6^{o}) as it varies with stress.

Shear-wave splitting was observed and recorded in all principal direction during the course of the experiment. Fast and slow shear-wave arrivals were picked and used to compute elastic properties and anisotropic parameters.

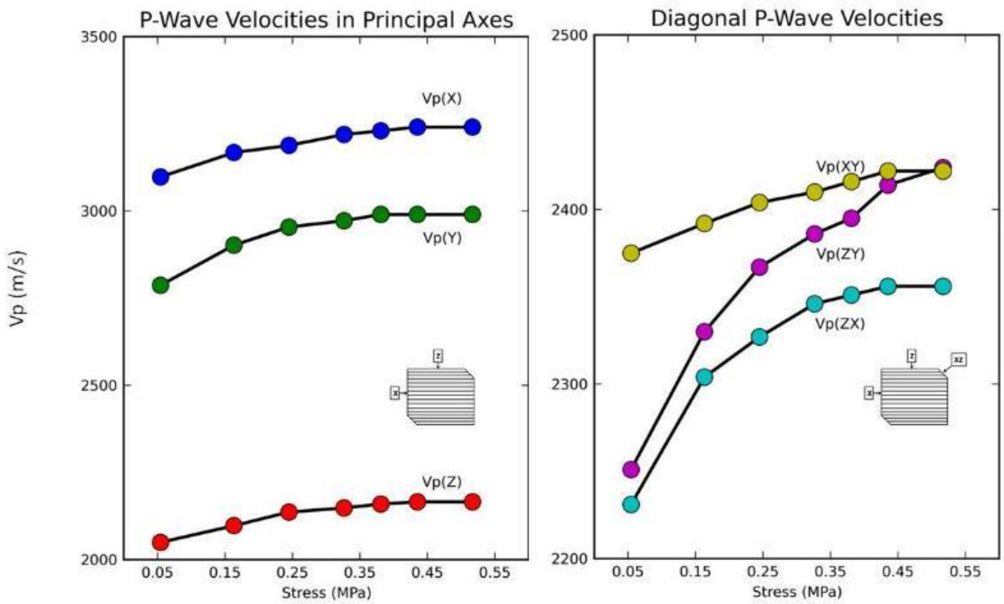

Figure 3.5: Compressional wave velocities as function of uniaxial stress. (P-wave velocity uncertainty is ± 0.15%)

Figure 3.6 displays a scaled shear-wave seismogram as a function of polarization angle (0° to 180° every 10°) in 3 different stress systems (0.16MPa, 0.33MPa, and 0.52MPa). Notice the decrease in arrival time for both fast (S1) and slow (S2) shear-waves as stress increases. The seismograms were produced for the Z-direction only.

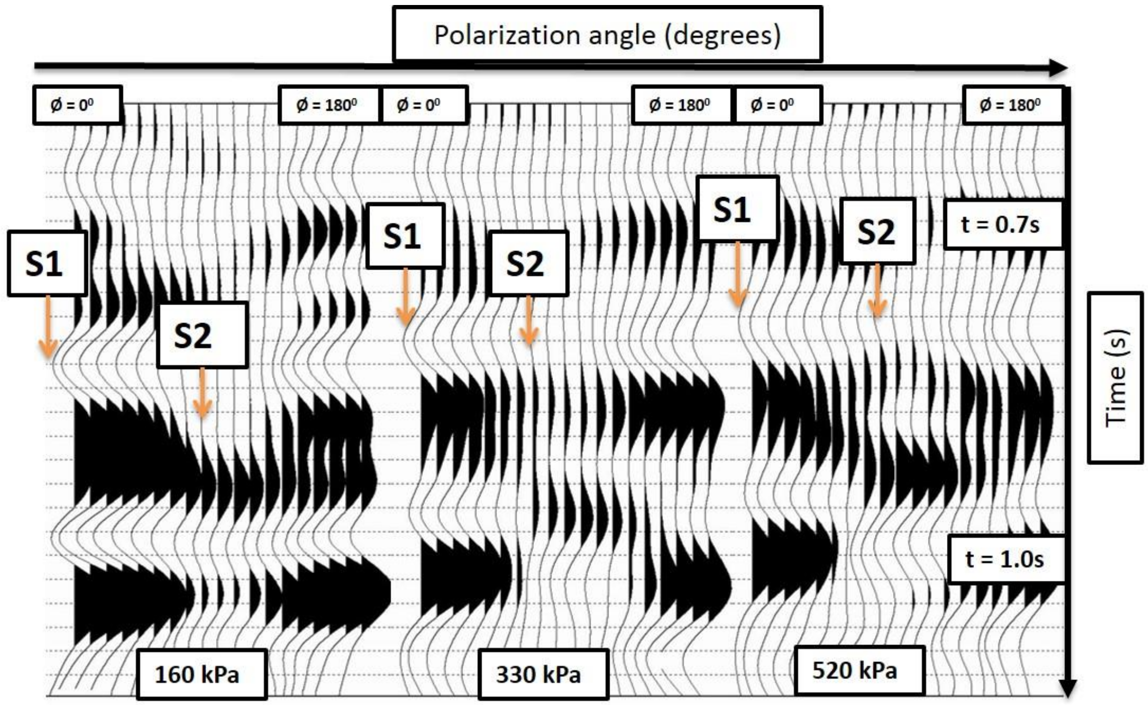

Figure 3.6: Shear-wave seismogram, as a function of shear-wave polarization (ø) in different stress regime (from left 0.16MPa, 0.33MPa, and 0.52MPa)

Figure 3.7 is a plot of fast and slow shear-wave velocities as uniaxial stress increases.

It can be observed from Figure 3.7 that velocities of fast and slow shear-waves largely increase with uniaxial stress. Also, the delay between fast and slow shear-waves tends to generally diminish in all planes of measurement. However, in the Z direction, delay between fast and slow shear-waves approaches a minimum; this is diagnostic of polar anisotropy (VTI). In a polar anisotropy (specifically VTI symmetry) case, $Vs_{1(z)} = Vs_{2(z)}$ due to a single axis of symmetry.

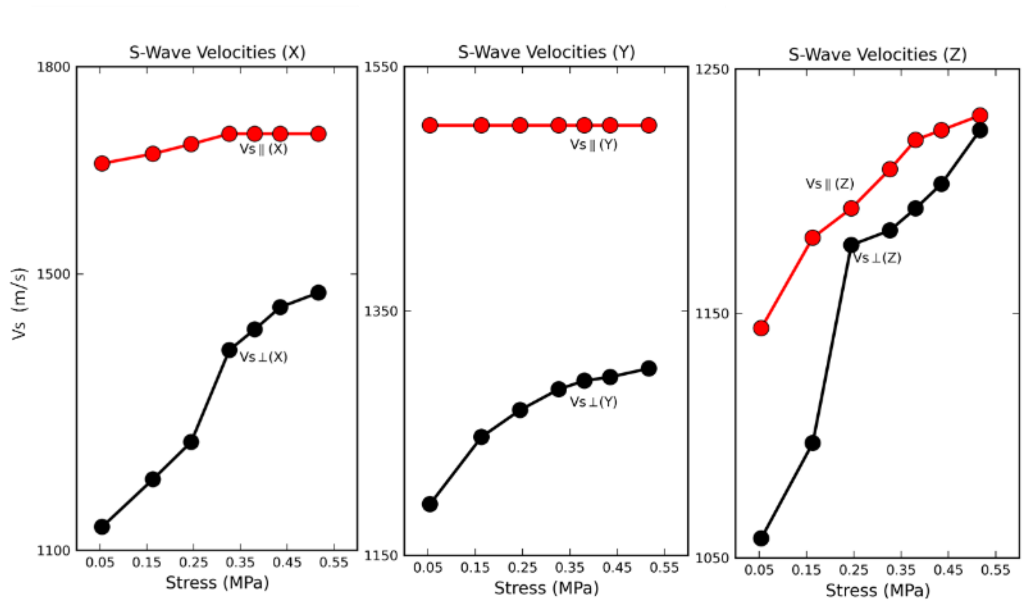

Figure 3.7: Fast and slow shear-wave velocities in X (1), Y (2) and Z (3) direction as a function of uniaxial stress. (S-wave velocity uncertainty is ± 1.5%)

3.4.3 Dynamic elastic stiffness and compliance matrices

Based on inherent physical properties and velocity measurements we can qualitatively describe our medium as orthorhombic.

From the generalized stress-strain law, $\boldsymbol{\tau_{ij}} = \boldsymbol{C_{ijkl}}\varepsilon_{\boldsymbol{kl}}$ (3.4)

In terms of compliance, the previous equation can be written as $\varepsilon_{\boldsymbol{kl}} = \boldsymbol{S_{ijkl}}\boldsymbol{\tau_{ij}}$ (3.5)

Where i, j = 1, 2 …6.

Using Voigt notation, equation 3.4 can be written as:

$$\begin{bmatrix} \tau_1 \\ \tau_2 \\ \tau_3 \\ \tau_4 \\ \tau_5 \\ \tau_6 \end{bmatrix} = \begin{pmatrix} \mathbf{C_{11}} & \mathbf{C_{12}} & \mathbf{C_{13}} & 0 & 0 & 0 \\ \mathbf{C_{12}} & \mathbf{C_{22}} & \mathbf{C_{23}} & 0 & 0 & 0 \\ \mathbf{C_{13}} & \mathbf{C_{23}} & \mathbf{C_{33}} & 0 & 0 & 0 \\ 0 & 0 & 0 & \mathbf{C_{44}} & 0 & 0 \\ 0 & 0 & 0 & 0 & \mathbf{C_{55}} & 0 \\ 0 & 0 & 0 & 0 & 0 & \mathbf{C_{66}} \end{pmatrix} \begin{bmatrix} \varepsilon_1 \\ \varepsilon_2 \\ \varepsilon_3 \\ \varepsilon_4 \\ \varepsilon_5 \\ \varepsilon_6 \end{bmatrix} \tag{3.6}$$

In terms of compliance, equation 3.6 (or equation 3.5) can be written as:

$$\begin{bmatrix} \varepsilon_1 \\ \varepsilon_2 \\ \varepsilon_3 \\ \varepsilon_4 \\ \varepsilon_5 \\ \varepsilon_6 \end{bmatrix} = \begin{pmatrix} \mathbf{S_{11}} & \mathbf{S_{12}} & \mathbf{S_{13}} & 0 & 0 & 0 \\ \mathbf{S_{12}} & \mathbf{S_{22}} & \mathbf{S_{23}} & 0 & 0 & 0 \\ \mathbf{S_{13}} & \mathbf{S_{23}} & \mathbf{S_{33}} & 0 & 0 & 0 \\ 0 & 0 & 0 & \mathbf{S_{44}} & 0 & 0 \\ 0 & 0 & 0 & 0 & \mathbf{S_{55}} & 0 \\ 0 & 0 & 0 & 0 & 0 & \mathbf{S_{66}} \end{pmatrix} \begin{bmatrix} \tau_1 \\ \tau_2 \\ \tau_3 \\ \tau_4 \\ \tau_5 \\ \tau_6 \end{bmatrix} \tag{3.7}$$

These elastic constants were computed from direct density and velocity measurements. P wave dependent stiffness coefficients were computed using the following equations,

$$\mathbf{C_{11}} = \boldsymbol{\rho}\mathbf{Vp}(\mathbf{x})^{\mathbf{2}} \quad , \mathbf{C_{22}} = \boldsymbol{\rho}\mathbf{Vp}(\mathbf{y})^{\mathbf{2}} \quad , \mathbf{C_{33}} = \boldsymbol{\rho}\mathbf{Vp}(\mathbf{z})^{\mathbf{2}} \tag{3.8}$$

Equally, shear-wave dependent elastic constants were calculated using Tsvankin (1997) extension of Thomsen's equation for orthorhombic models. In this case, it manifests as an averaging of fast and slow shear-wave velocities across adjacent axes according to the following equations,

$$\mathbf{C_{44}} = \boldsymbol{\rho}\left(\frac{\mathbf{V_{s2(y)}} + \mathbf{V_{s2(z)}}}{\mathbf{2}}\right)^{\mathbf{2}}, \mathbf{C_{55}} = \boldsymbol{\rho}\left(\frac{\mathbf{V_{s1(z)}} + \mathbf{V_{s2(x)}}}{\mathbf{2}}\right)^{\mathbf{2}}, \mathbf{C_{66}} = \boldsymbol{\rho}\left(\frac{\mathbf{V_{s1(y)}} + \mathbf{V_{s2(x)}}}{\mathbf{2}}\right)^{\mathbf{2}} \quad (3.9)$$

Diagonal stiffness coefficients however were computed using a polar anisotropy assumption in each block face (or principal axis). Unambiguously, VTI assumption in ZX and ZY axes and HTI in XY plane. Bearing in mind that we do not have exact 45^0 angle in some axes, we have used an angle dependent form of Thomsen's (1986) equation and this eventually collapses to the more common diagonal elastic constant equations when $\theta = 45^0$,

$$\boldsymbol{C_{13}} = \left[\frac{\boldsymbol{A-B}}{\mathbf{4}\sin^2\boldsymbol{\theta}\cos^2\boldsymbol{\theta}}\right]^{\mathbf{0.5}} - \boldsymbol{C_{44}} \quad (3.10)$$

where,

$$\boldsymbol{A} = [\mathbf{2}\boldsymbol{\rho V p_{zx}^2} - (\boldsymbol{C_{11}} + \boldsymbol{C_{44}})\sin^2\boldsymbol{\theta} - (\boldsymbol{C_{33}} + \boldsymbol{C_{44}})\cos^2\boldsymbol{\theta}]^{\mathbf{2}} \quad (3.11)$$

$$\boldsymbol{B} = [(\boldsymbol{C_{11}} - \boldsymbol{C_{44}})\sin^2\boldsymbol{\theta} - (\boldsymbol{C_{33}} - \boldsymbol{C_{44}})\cos^2\boldsymbol{\theta}]^{\mathbf{2}} \quad (3.12)$$

Equation 3.10 generally decomposes to the following when $\theta = 45^o$,

$$\mathbf{C_{13}} = \left[\frac{\left(\mathbf{4Vp45(zx)}^{\mathbf{2}} - \mathbf{C_{11}} - \mathbf{C_{33}} - \mathbf{2C_{44}}\right)^{\mathbf{2}} - (\mathbf{C_{11}} - \mathbf{C_{33}})^{\mathbf{2}}}{\mathbf{4}}\right]^{\mathbf{0.5}} - \mathbf{C_{44}} \quad (3.13)$$

Similar assumptions were used to calculate C_{23} and C_{12} (an HTI assumption was used to compute C_{12}). Figure 3.8 shows compressional and shear-wave dependent as well as diagonal stiffness coefficients as a function of uniaxial stress. Coefficient C_{33} is low (Figure 3.8a) in comparison to the rest due to the nature of the phenolic material being used.

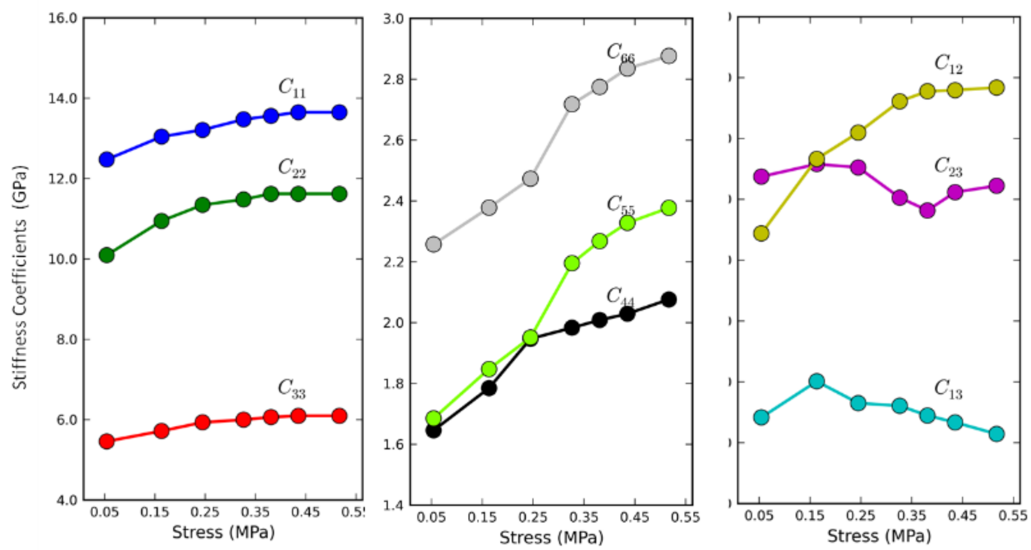

Figure 3.8: Stiffness coefficients as a function of uniaxial normal stress

Within the limit of this experiment, all stiffness coefficients tend to increase with uniaxial stress. There seem to be an exception to this trend for elastic constants C_{13} and C_{23} that tend to remain constant or reduce. Significant or large errors are expected in computation of diagonal elastic constants due to the sensitivity of angle dependent velocities to transducer directivity. However, diagonal elastic C_{33} increases significantly with stress.

This may be due to an unknown preferred orientation within the wave fabric of the phenolic model.

We also computed compliance parameters from the stiffness matrix using the following equations,

$$\mathbf{S_{11}} = \left(\frac{\mathbf{C_{22}C_{33}-C_{23}^2}}{\mathbf{D}}\right),\ \mathbf{S_{22}} = \left(\frac{\mathbf{C_{11}C_{33}-C_{13}^2}}{\mathbf{D}}\right),\ \mathbf{S_{33}} = \left(\frac{\mathbf{C_{11}C_{22}-C_{12}^2}}{\mathbf{D}}\right) \tag{3.14}$$

$$\mathbf{S_{12}} = \left(\frac{\mathbf{C_{13}C_{23}-C_{12}C_{33}}}{\mathbf{D}}\right), \mathbf{S_{13}} = \left(\frac{\mathbf{C_{12}C_{23}-C_{13}C_{22}}}{\mathbf{D}}\right), \mathbf{S_{23}} = \left(\frac{\mathbf{C_{12}C_{13}-C_{11}C_{23}}}{\mathbf{D}}\right) \tag{3.15}$$

where D = $\mathbf{C_{11}C_{22}C_{33} + 2C_{12}C_{13}C_{23} - C_{11}C_{23}^2 - C_{22}C_{13}^2 - C_{33}C_{12}^2}$

For shear-wave dependent compliance,

$$\mathbf{S_{44}} = \left(\frac{\mathbf{1}}{\mathbf{C_{44}}}\right), \mathbf{S_{55}} = \left(\frac{\mathbf{1}}{\mathbf{C_{55}}}\right), \mathbf{S_{66}} = \left(\frac{\mathbf{1}}{\mathbf{C_{66}}}\right) \tag{3.16}$$

Figure 3.9 shows all elastic compliances as a function of uniaxial normal stress.

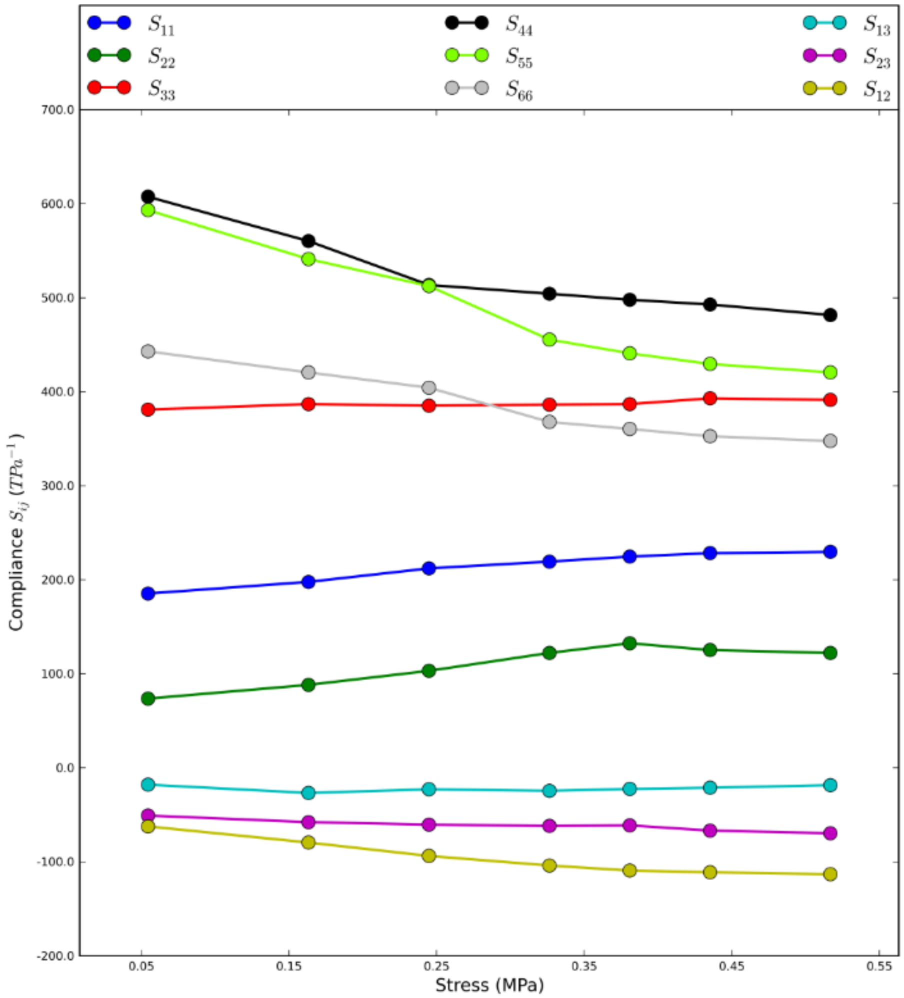

Figure 3.9: Elastic compliance as a function of uniaxial normal stress

3.4.4 Anisotropic parameters

To quantify the anisotropy in our measurements, anisotropic parameters ε and γ (compressional and shear-wave anisotropies respectively) were computed using the same extension of Thomsen's parameter (Tsvankin, 1997). The equations are listed as the following,

$$\varepsilon_{\mathbf{xz}} = \frac{1}{2}\left(\frac{V_{px}-V_{pz}}{V_{pz}}\right) = \varepsilon^{1}\ ,\ \varepsilon_{\mathbf{yz}} = \frac{1}{2}\left(\frac{V_{py}-V_{pz}}{V_{pz}}\right) = \varepsilon^{2}\ ,\ \varepsilon_{\mathbf{xy}} = \frac{1}{2}\left(\frac{V_{px}-V_{py}}{V_{py}}\right) = \varepsilon^{3} \qquad (3.17)$$

$$\boldsymbol{\gamma_x} = \frac{1}{2}\left(\frac{\boldsymbol{Vs1}(x)^2}{\boldsymbol{Vs2}(x)^2} - \mathbf{1}\right) = \boldsymbol{\gamma^1} \qquad (3.18)$$

$$\boldsymbol{\gamma_y} = \frac{1}{2}\left(\frac{\boldsymbol{Vs1}(y)^2}{\boldsymbol{Vs2}(y)^2} - \mathbf{1}\right) = \boldsymbol{\gamma^2} \qquad (3.19)$$

$$\boldsymbol{\gamma_z} = \frac{1}{2}\left(\frac{\boldsymbol{Vs1}(z)^2}{\boldsymbol{Vs2}(z)^2} - \mathbf{1}\right) = \boldsymbol{\gamma^3} \qquad (3.20)$$

Some earlier publications on orthorhombic anisotropy expressed these equations as ε^1, ε^2, ε^3 and γ^1, γ^2, γ^3. Figure 8 shows compressional (ε) and shear-wave (γ) anisotropies as a function of uniaxial stress. Anisotropic parameter ε (Figure 3.10a) tends to remain constant within the limit of the experiment. The reason for the difference in ε_{yx} value is once more due to the nature of the composite phenolic material in the Z (or 3) direction. There is a large difference in compressional wave velocity in X or Y direction compared to Z which explains the large values of ε_{xz} and ε_{yz} compared to ε_{yx}. Anisotropic parameter γ (Figure 3.10b) largely diminishes with increasing stress. In the Z direction (γ_z) it tends towards zero at higher stress states. This is once again diagnostic of VTI symmetry. In a VTI polar anisotropy case, $\gamma_z = 0$

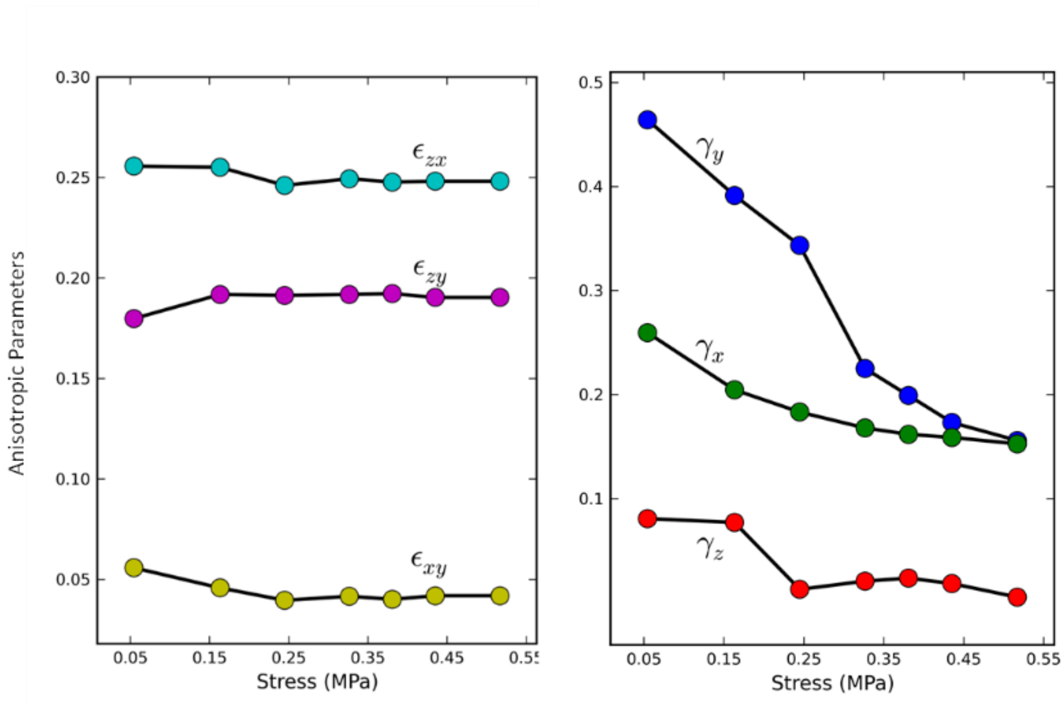

Figure 3.10: Anisotropic parameter ε (Compressional wave anisotropy) and **γ** (shear-wave anisotropy) as a function of uniaxial stress

3.5 Conclusions

This experimental study has investigated changes in velocity, elastic properties and anisotropic parameters in an orthorhombic medium as function of uniaxial stress. Based on our experimental results, we can make the following inferences:

1. From the stress-strain curve showing uniaxial loading and unloading, we observe an unusual strain trend during unloading. This may be due to low frequency heterogeneity or anisotropy within the composite model..
2. P- and S-wave velocities increased generally with increasing uniaxial stress
3. Shear-wave splitting was observed on all faces and axes of the model, however the magnitude of this seismic birefringence seem to reduce with increase in uniaxial stress. This phenomenon was observed with varying intensity on all faces/axes.
4. Polar anisotropy (specifically VTI) symmetry appear to dominate the character of anisotropy in the Z (or 3) direction as uniaxial stress increases. This is particularly significant because this direction represents the direction normal to stratification and the plane of most interest to exploration geophysics
5. Elastic stiffness coefficient C_{55} and C_{66} seem very sensitive to increase in stress, suggesting slow shear-waves in the X-direction are quite sensitive to increasing stress.

   $$\mathbf{C_{55}} = \boldsymbol{\rho}\left(\frac{\mathbf{V_{s1(z)}} + \mathbf{V_{s2(x)}}}{\mathbf{2}}\right)^{\mathbf{2}}, \mathbf{C_{66}} = \boldsymbol{\rho}\left(\frac{\mathbf{V_{s1(y)}} + \mathbf{V_{s2(x)}}}{\mathbf{2}}\right)^{\mathbf{2}} \qquad (3.21)$$

   Also, direct slow shear-wave velocity in the X-direction appear most sensitive to stress

6. A practical application of this type of experiment is for modeling intrinsically orthorhombic rocks under stress. Velocity and elastic parameters can serve as input parameters for such numerical models.

Acknowledgements

This physical modeling project was made possible by the financial support of Allied Geophysical Laboratories, University of Houston. The authors are grateful Dr. Evgeny Chesnokov at the University of Houston for his expert advice.

3.6 References

Cheadle, S.P., R.J. Brown., and D.C. Lawton., 1991. Orthorhombic anisotropy: A physical modeling study. Geophysics. **56**, 1603 – 1613

Ebrom, D. A., R. H. Tatham, K. K. Sekharan, J. A. McDonald, and G. H. F. Gardner, 1990, Hyperbolic transmission analysis of first arrivals in an azimuthally anisotropic medium: A physical modeling study. Geophysics. **55**, 185–191.

Ebrom, D., J.A. McDonald, 1994, Seismic physical modelling. Geophysics Reprint Series. Vol **15**, 1-3.

Far, M. E., J. J. S, de Fegueiredo., R. R, Stewart., J. P, Castagna, D. Han and N, Dyaur, 2014, Measurements of seismic anisotropy and fracture compliances in synthetic fractured media. Geophysical Prospecting. **197**, 1845-1857

Hornby, B.E., 1998. Experimental laboratory determination of the dynamic elastic properties of wet, drained shales. Journal of Geophysical Research. **103** (B12), 29945–29964.

Jones, L.E.A., Wang, H.F., 1981. Ultrasonic velocities in Cretaceous shales from the Williston basin. Geophysics. **46** (3), 288–297.

Jones, L. E., and H. F, Wang., 1981, Ultrasonic velocities in Cretaceous shale from the Williston Basin. Geophysics, **46**, 288-297.

Omoboya, B., J. J. S, de Fegueiredo., N, Dyaur., and R. R, Stewart., 2011, Uniaxial stress and ultrasonic anisotropy in a layered orthorhombic medium. SEG Expanded Abstracts. **30**, 2145-2149.

Pervukhina, M., and D. Dewhurst., 2008, Stress-dependent elastic properties of shales: Measurement and modeling. Leading Edge. **27**, 772-779.

Podio, A.L., Gregory, A.R., Gray, K.E., 1968. Dynamic properties of 16 dry and water-saturated green river shale under stress. Society of Petroleum Engineers Journal. SPE. 1825.

Rathore J.S., Fjaer E., Holt R.M. and Renlie L. 1995. P- and S-wave anisotropy of a synthetic sandstone with controlled crack geometry. Geophysical Prospecting. **43**, 711-728.

Sarout, J., L. Molez., Y. Gueguen., and N. Hoteit. 2006. Shale dynamic properties and anisotropy under triaxial loading: Experimental and theoretical investigations. Physics and Chemistry of the Earth. **32**, 896-906.

Sayers C.M. 2002. Fluid-dependent shear-wave splitting in fractured media. Geophysical Prospecting. **50**, 393 - 401.

Stewart, R.R., N. Dyaur., B. Omoboya., J. J. S. de Figueiredo., M. Willis., and S. Sil, 2013. Physical modeling of anisotropic domains: Ultrasonic imaging of laser-etched fractures in glass. Geophysics. **78**, 11-19

Tatham, R. H., M. D. Matthews, K. K. Sekharan, C. J.Wade, and L. M. Liro, 1992, A physical model study of shear-wave splitting and fracture intensity. Geophysics. **57**, 647–652

Thomsen, L.,1986, Weak elastic anisotropy. Geophysics. **51**, 1954-1966.

Tsvankin, I., 1997, Reflection moveout and parameter estimation for horizontal transverse isotropy. Geophysics. **62**, 614-629.

Yin, H., 1992. Acoustic velocity and attenuation of rocks: isotropy, intrinsic anisotropy, and stress-induced anisotropy. Ph.D. dissertation. Stanford University, Palo Alto, CA, USA.

CHAPTER FOUR

Anisotropic characterization by NMO ellipses in the Williston Basin

Bode Omoboya[1] and Robert R. Stewart[1]

[1]- University of Houston, Department of Earth and Atmospheric Sciences, Houston-Texas, USA: Email: bodeomoboya@gmail.com, and rrstewart@uh.edu

4.1 Summary

Using 3D wide-azimuth data from Ross field area of the Williston Basin in North Dakota, we present seismic processing steps and workflows for elliptical fitting of NMO velocities for subsurface characterization. An NMO ellipse can be loosely defined as a plot of the trend of NMO velocity with azimuth. Via this velocity-based method, we demonstrate a potential for using wide-azimuth P-wave seismic data as a tool for subsurface characterization in shale reservoirs. If automated, we believe this method can help create a general overview of anisotropic trends in the subsurface in a relatively short time. Principal subsurface anisotropic alignment seem consistent with results from microseismic data within the limited scope of this study.

4.2 Introduction

With the advent of unconventional tight shale oil and gas, acquisition and analysis of land wide-azimuth seismic data have become more important, (Sonnenberg, 2013). The current challenge is to effectively extract useful sub-surface information from these wide-azimuth datasets to assist drilling and completion decisions. Unconventional shale plays are sometimes viewed as a mining problem rather than an exploration problem (Sonnenberg, 2013). A general goal is to demonstrate ways in which geophysics can assist with these well planning and field development decisions, as is routinely done in many conventional oil and gas developments. This should help reduce drilling risk and increase the overall profitability of the process.

Attributes such as brittleness, organic richness, and water saturation are important in these plays. Also important are the directions, orientations and intensity of minimum and maximum *in-situ* horizontal stresses because these can influence drilling decisions significantly. If natural fractures are present, qualitative and quantitative analysis of these fractures are equally important. Well data can provide useful insight into nature of *in-situ* stress and fractures, but only wide-azimuth seismic data can give a relatively less expensive yet broader view of the nature of the subsurface (*in-situ* stress and/or fractures).

In this dissertation, we present a workflow for creating of NMO ellipses. We demonstrate the potential for using P-wave wide-azimuth data for subsurface characterization. The data used in this project were from Mountrail County in North Dakota, USA. The Red Sky 3D data cover an area of about 250 sq. miles (650 sq. km) and 6 townships (from T156N R90W to T156N R95W). It straddles the Ross, Beaver Lodge, Manitou, Baskin, and Alger fields, in North Dakota, USA.

4.3 Petroleum geology of the Williston Basin

The Williston Basin is a cratonic basin straddling the northern United States and southern Canada. The Williston Basin is approximately 133,000 mi^2 (345,000 km^2) in size. It occupies parts of Saskatchewan and Manitoba in Canada and the states of North Dakota, South Dakota and Montana in the United States. The Williston Basin is structurally straight forward and roughly elliptical in shape with its deepest part in the center. Figure 4.1 shows a location map of the Williston Basin. The red box shows the approximate location of the Red Sky survey area.

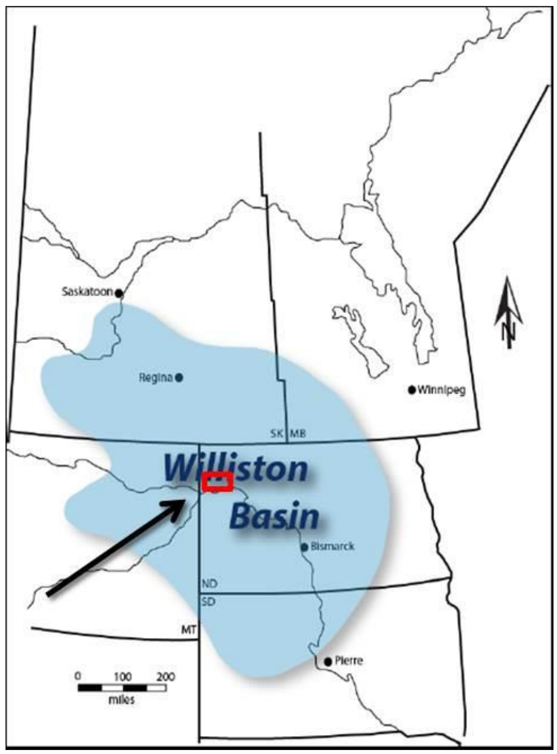

Figure 4.1: Location map of the Williston Basin (Modified after LeFever, 2013).

The Williston Basin contains a stratigraphic section containing mostly limestone and evaporite. There are many oil- and gas-producing zones within the Williston Basin. Figure 4.2 shows a stratigraphic column of the Williston Basin.

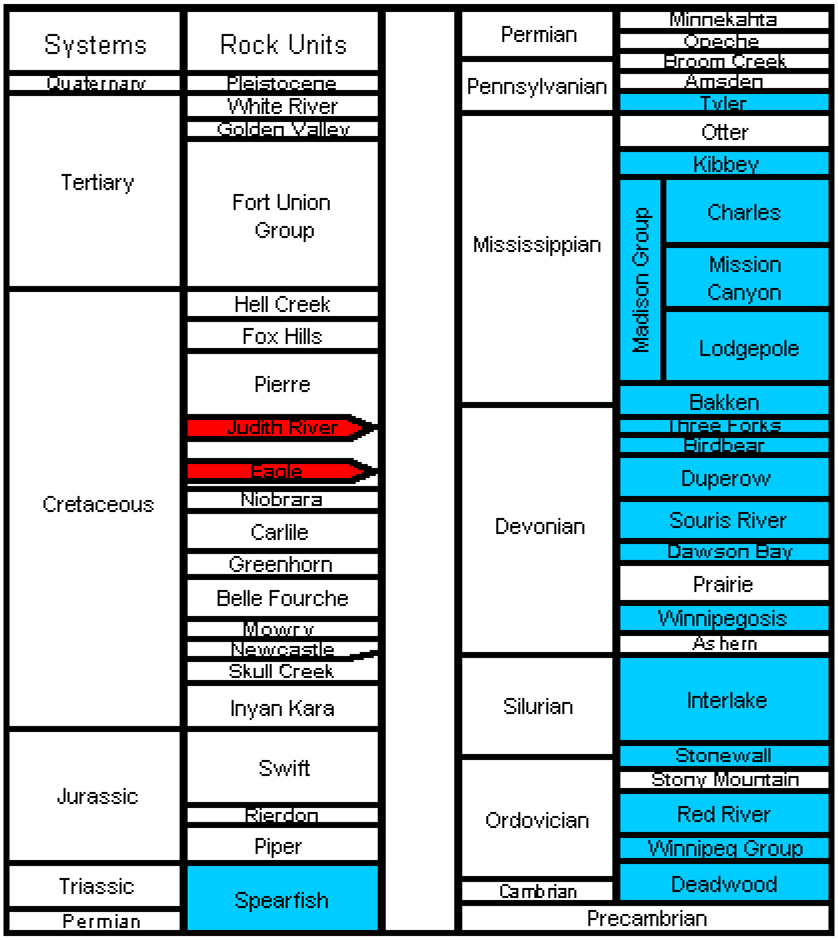

Figure 4.2: Generalized stratigraphic column of the Williston Basin with gas-producing zones in red and oil-producing zones in blue. (Source: North Dakota Industrial Commission).

In this study, our area of interest includes the Greenhorn Formation as well as the Bakken Petroleum System (Lodgepole Fm, Bakken Fm, and Three Forks Fm)

4.3.1 Greenhorn Formation

The Greenhorn Formation is a late Cretaceous mostly gray to black calcareous shale formation. It has a thickness ranging from 50 to 250 ft (15 to 75m). The Greenhorn and Pierre Formations together make an approximately 1000 ft (300m) thick shale unit over the study area.

4.3.2 The Bakken Petroleum System

The Bakken Petroleum System consists of the Mississippian Lodgepole Formation, the Devonian-Mississippian Bakken Formation, and the Devonian Three Forks Formation (Price and LeFever, 1994). The Bakken Formation is a closed, low-permeability petroleum system that has generated approximately 3 to 4.3 billion barrels of technically recoverable oil in place. The Bakken reaches a maximum thickness of 150 feet (46 m) in the central portion of the Williston Basin and it is easily recognizable on well logs (circled in Figure 4.3). The Bakken Formation overlies the Three Forks Formation and underlies the Lodgepole Formation (Figures 4.2 and 4.3).

The Lodgepole is made up of several shale-to-limestone cycles that are expressed as a progradational carbonate platform (Grover, 1996). The lower part of the Lodgepole limestone can be naturally fractured and act as a local reservoir.

The Three Forks consists of interbedded mudstone and dolomite that can also serve as an oil reservoir. Recently, well completions in the Three Forks have increased significantly (Sonnenberg, 2013). Figure 4.3 shows well logs alongside well cores for the Bakken petroleum system.

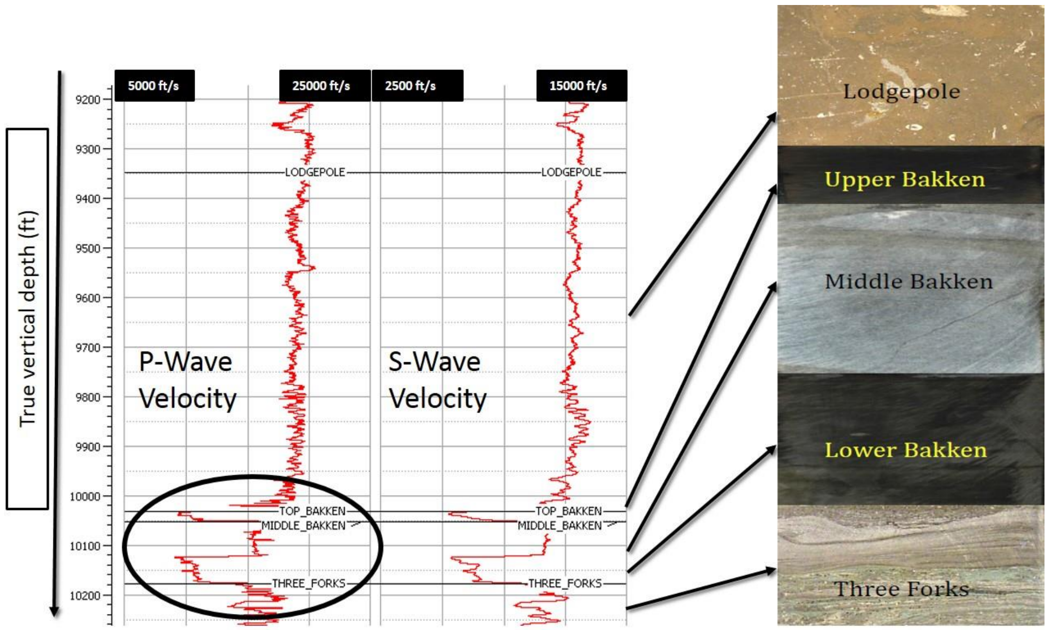

Figure 4.3: Well logs (compressional and shear-wave velocities) and well core images from the Bakken petroleum system.

The Bakken Formation has three distinct members: the Upper Shale Member, the Middle Clastic Member, and the Lower Shale Member (Figure 4.3). The Upper and Lower Members exhibit very high gamma ray readings (> 200 API), high sonic slowness (80 to 120 µs/ft.), and low resistivity readings (Pitman et al. 2001). The Middle Member is typically clastic or mostly carbonate rocks. The lithology of the Middle Member is highly variable and it consists of interbedded sequences of siltstones and sandstones with lesser amounts of shale, dolostones, limestone, and oolites (Pitman et al. 2001). Measured porosity in the Middle Member ranges from 1% to 16%, averaging about 5%. Permeability ranges from 0 to 20 mD as well, averaging around 0.04 mD. Pitman et al. (2001) conclude that higher permeability in the Middle Member corresponds to open and well-developed fractures. Most oil in the Bakken petroleum system is produced from the Bakken clastic Middle Member.

4.4 Red Sky seismic survey and wells

4.4.1 Red Sky 3D seismic survey

The Red Sky 3D survey is located in Mountrail County, North Dakota. The Red Sky 3D survey straddles Ross, Beaver Lodge, Manitou, Baskin, and Alger fields. In total, the 3D seismic area covers about 250 sq. mi (650 sq. km). Figure 4.4 shows a location map of the Red Sky 3D survey. Township range of the Red Sky survey is from T156N R90W to T156N R95W (approximately 6 townships in total. where 1 township = 6 miles X 6 miles or 9.6 km X 9.6 km area).

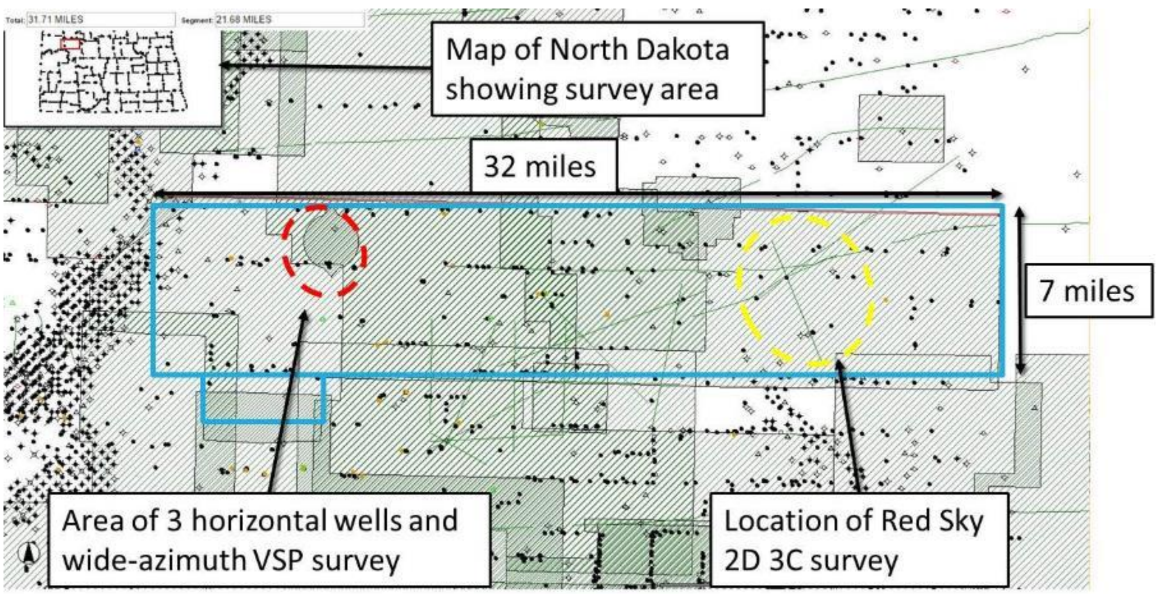

Figure 4.4: Location map of the Red Sky 3D survey (blue polygon) showing areas of Red Sky 2D-3C survey (yellow circle) and wide-azimuth VSP survey (red circle). Display from North Dakota Industrial Commission – NDIC

The maximum fold for the Red Sky survey is 110 with average fold at around 90.

Inline range is from 718 to 1145 while cross-line ranges from 481 to 2083. Survey spacing is 110 ft X 110 ft (33 m X 33 m). Figure 4.5 shows a fold map of the Red Sky 3D survey.

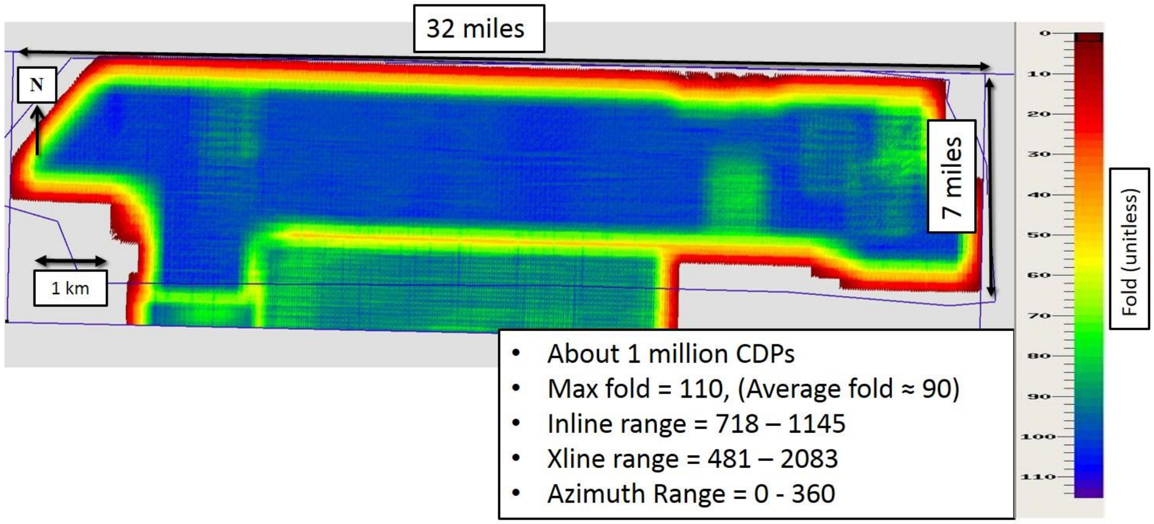

Figure 4.5: Fold map of the Red Sky 3D survey (display from Paradigm GeoDepth® software)

The azimuth and offset distribution in the Red Sky survey is robust enough for azimuthal and anisotropic studies (including far offset studies). Figures 4.6 and 4.7 show typical azimuth and offset distributions for the Red Sky 3D survey.

In the Red Sky survey, all azimuths are grid azimuths (i.e. azimuths are calculated from X and Y coordinates obtained from SEG-Y trace headers). The projection system used for the Red Sky seismic survey is North Dakota North State Plane 3301, NAD 1927.

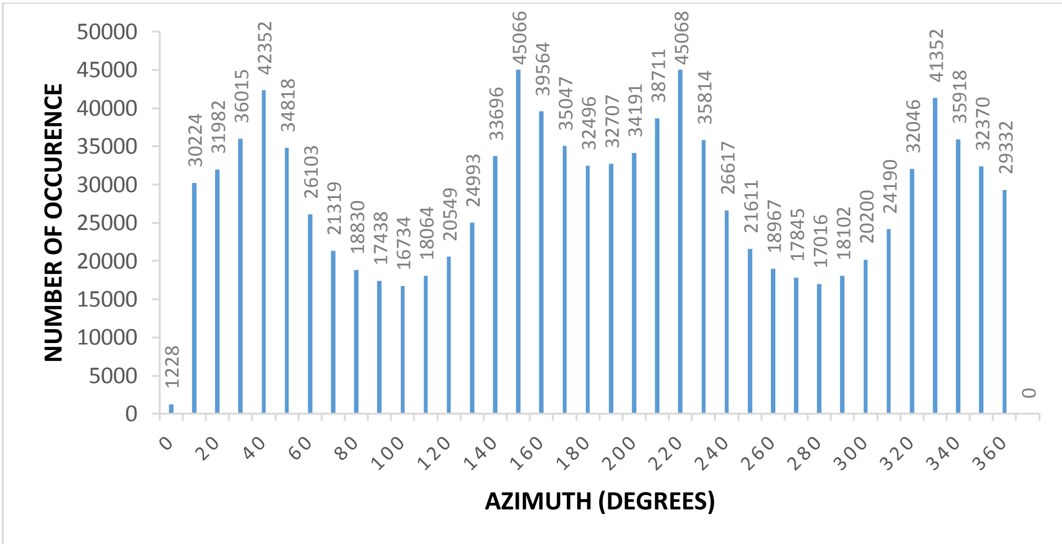

Figure 4.6: Frequency histogram of azimuth distribution from CDP gathers in the Red Sky survey.

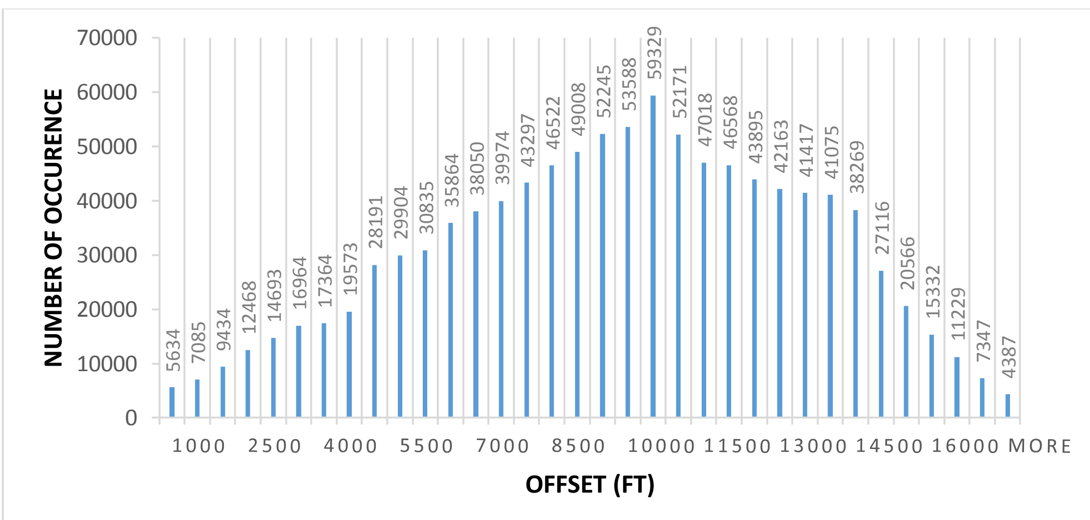

Figure 4.7: Frequency histogram of offset distribution from CDP gathers in the Red Sky survey.

Although the 40º azimuth (and corresponding orthogonal and mirror angles) seem to be the most abundant, other azimuths are sufficiently covered for a robust wide-azimuth study.

Figure 4.8 shows a map view of direction and azimuth of source-receiver pairs originating from one common mid-point (CMP).

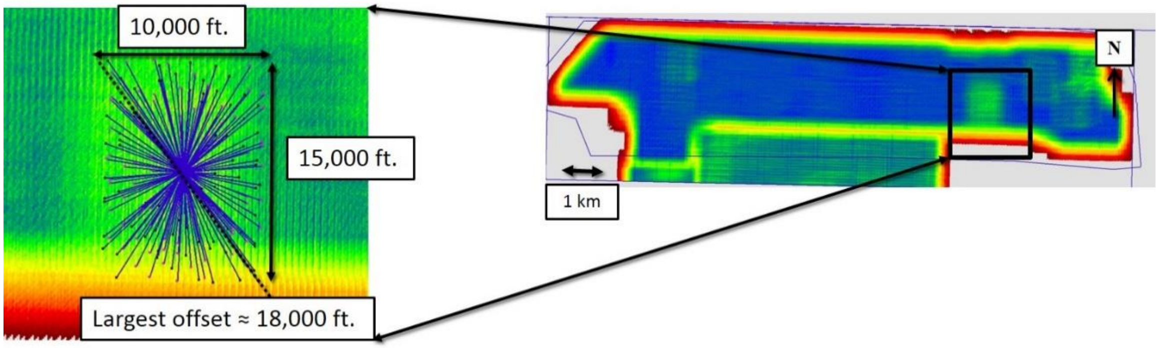

Figure 4.8: Azimuthal distribution of source-receiver pairs from one common mid-point.

The most abundant offsets ranges from about 8000ft (2400m) to 12000ft (3650m). This is appropriate for both normal and long offset anisotropic residual moveout studies since the maximum depth of interest is about 10,000 ft. (3000m) deep.

The Red Sky 3D survey has about 1 million CDP locations and the record length is 4s with a 2ms sample interval.

Shot and receiver acquisition parameters for the Red Sky survey are illustrated in Tables 4.1 and 4.2.

Receiver line spacing	880ft (268m)
Receiver spacing	220ft (67m)
Receiver array	6 per group
Receiver line azimuth	N 2.4° E (Grid Azimuth)

Table 4.1: Receiver geometry for the Red Sky 3D survey

Shot line spacing	1760ft (536m)
Shot point spacing	220ft (67m)
Source type	Vibroseis
Sweep frequency	8-120 Hz
Sweep length/listening time	10/4 seconds
Shot line azimuth	N 43° E (Grid Azimuth)

Table 4.2: Shot geometry for the Red Sky 3D survey

Figure 4.9 also shows orientation and azimuth of Red Sky 3D source and receiver lines.

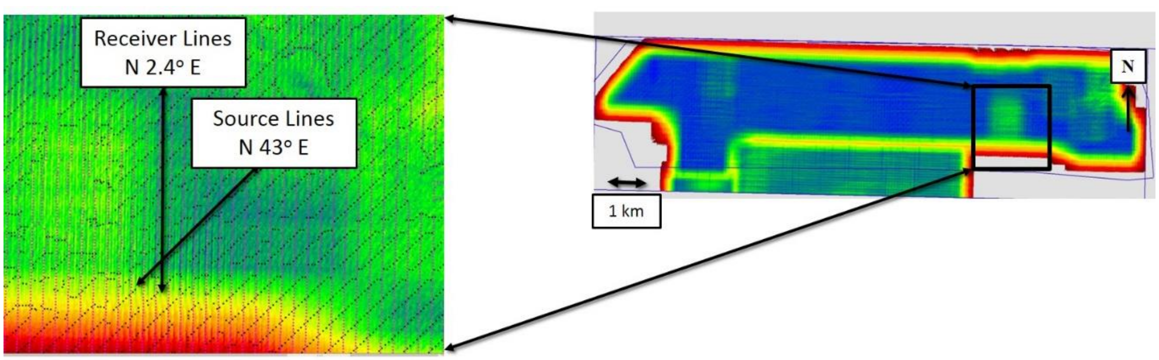

Figure 4.9: Azimuthal orientation of source and receiver lines in the Red Sky survey.

4.4.2 Red Sky wells

There are seven wells provided for the purpose of this study. Three of the wells are horizontal wells surrounded by four monitoring wells. Figure 4.10 shows a map view of all horizontal and vertical wells.

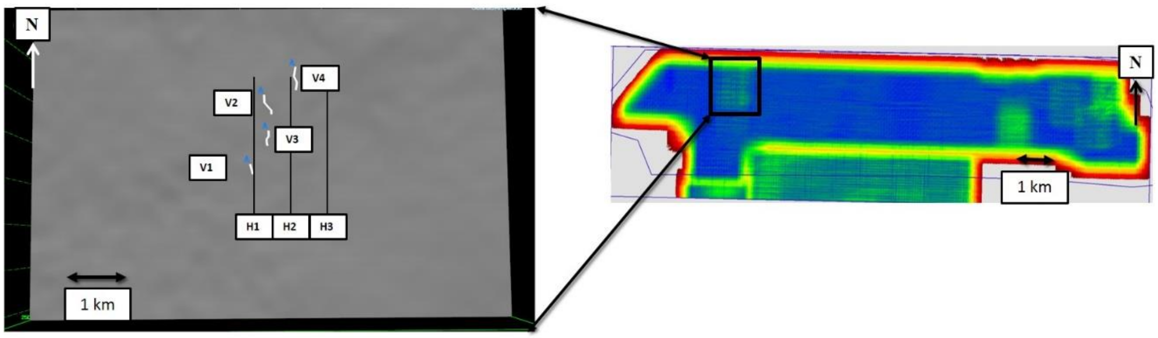

Figure 4.10: Location of seven wells (4 vertical, 3 horizontal) with reference to the Red Sky 3D survey.

Table 4.3 also shows details of wells used and analyzed in this study.

Well Name	TVD (ft.)	MD (ft.)	Easting (ft.)	Northing (ft.)	Kelly Bushing (ft.)	Vertical/ Horizontal
H1	10044	20109	1457249	497590	2248	H
H2	10028	20375	1457472	497586	2245	H
H3	10026	20448	1456689	497658	2261	H
V1	10516	10516	1456901	500385	2249	V
V2	10477	10477	1457565	503585	2198	V
V3	10439	10439	1458866	503117	2247	V
V4	10484	10484	1459029	504876	2218	V

Table 4.3: Details of the wells analyzed in the Red Sky survey

4.5 Red Sky seismic processing

The seismic processing techniques used for the Red Sky 3D survey were conventional and robust enough to incorporate wide-azimuth analysis in different stages. Most of the seismic processing was routine but careful enough to preserve key seismic attributes such as seismic amplitudes. Considerable care was taken to preserve true amplitudes while enhancing key reflectors. Acquisition details of Red Sky 3D survey were discussed in section 4.3.1.

4.5.1 3D processing

Since statics and deconvolution were already applied to the 3D Red Sky dataset, the next relevant processing sequence was noise attenuation and sorting. With a few exceptions, the processing flow applied for 2D-3C Red Sky survey was similar to that applied for the 3D dataset. Figure 4.11 shows the processing flow for the Red Sky 3D dataset (grey boxes represent pre-applied processing steps).

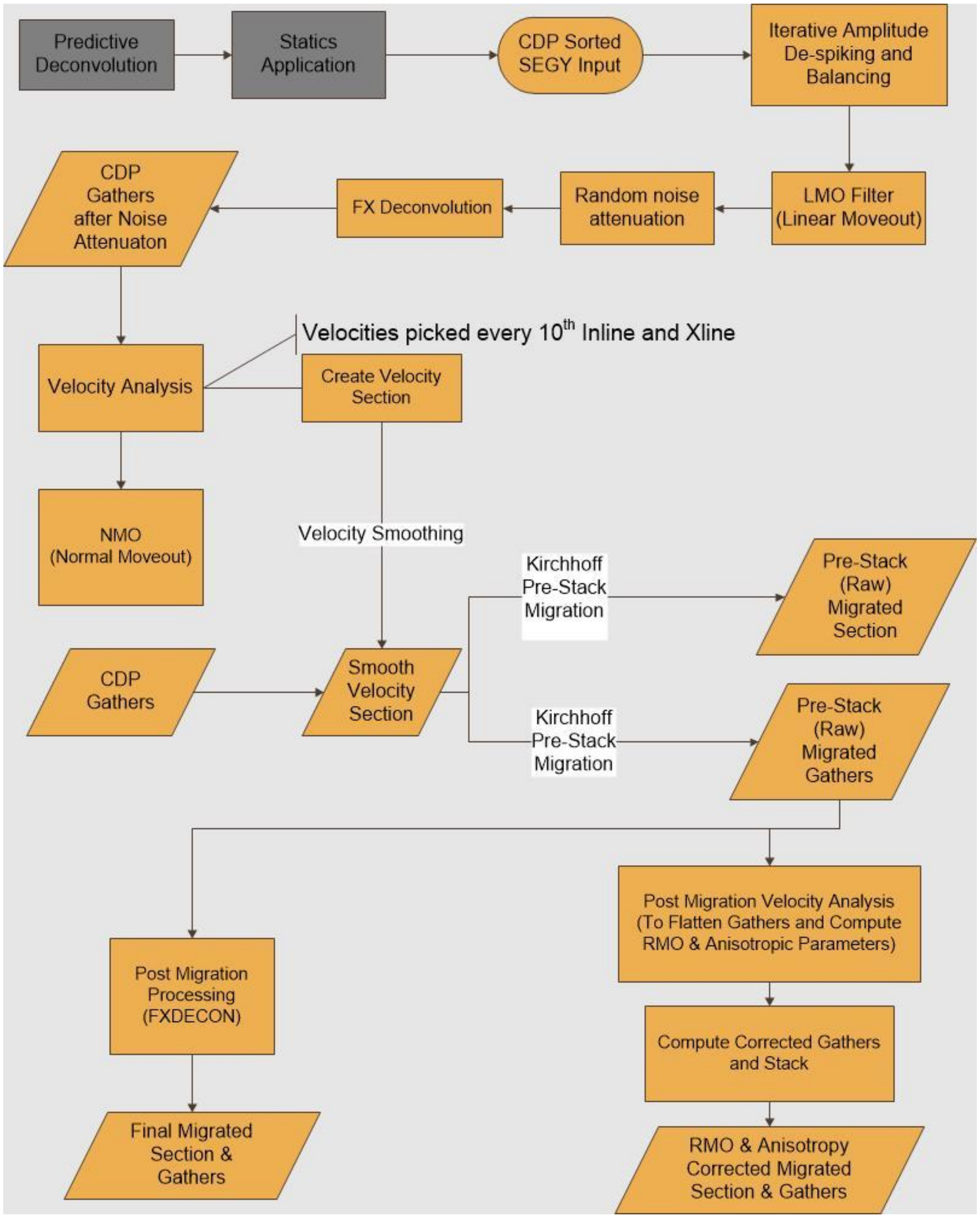

Figure 4.11: Processing flow diagram for Red Sky 3D seismic data (grey boxes represent pre-applied processing steps).

As a QC for the noise attenuation techniques, shot gathers were extracted from the position of the Red Sky 2D survey and the same noise attenuation workflow as the 2D dataset was applied to the 3D dataset. Figure 4.12 shows relative position of Red Sky 2D to 3D surveys.

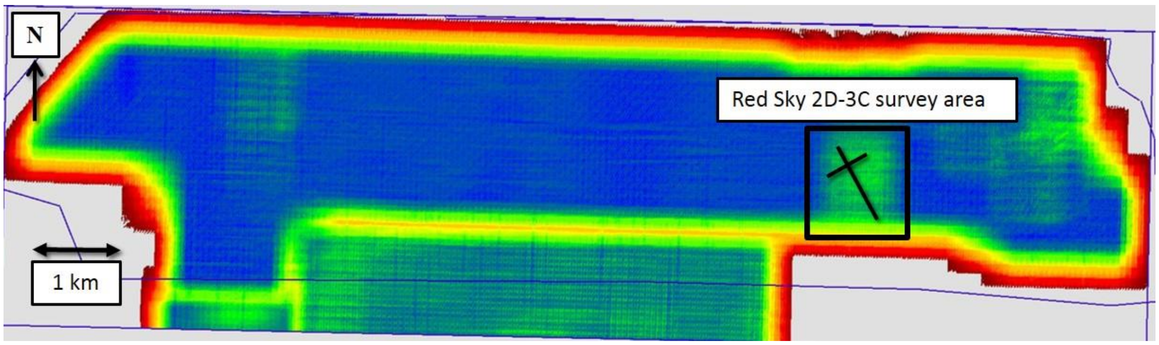

Figure 4.12: Location of Red Sky 2D survey relative to Red Sky 3D.

Figure 4.13 shows a raw CMP gather from the newly loaded 3D SEG-Y file. Its corresponding frequency spectrum is shown in Figure 4.14.

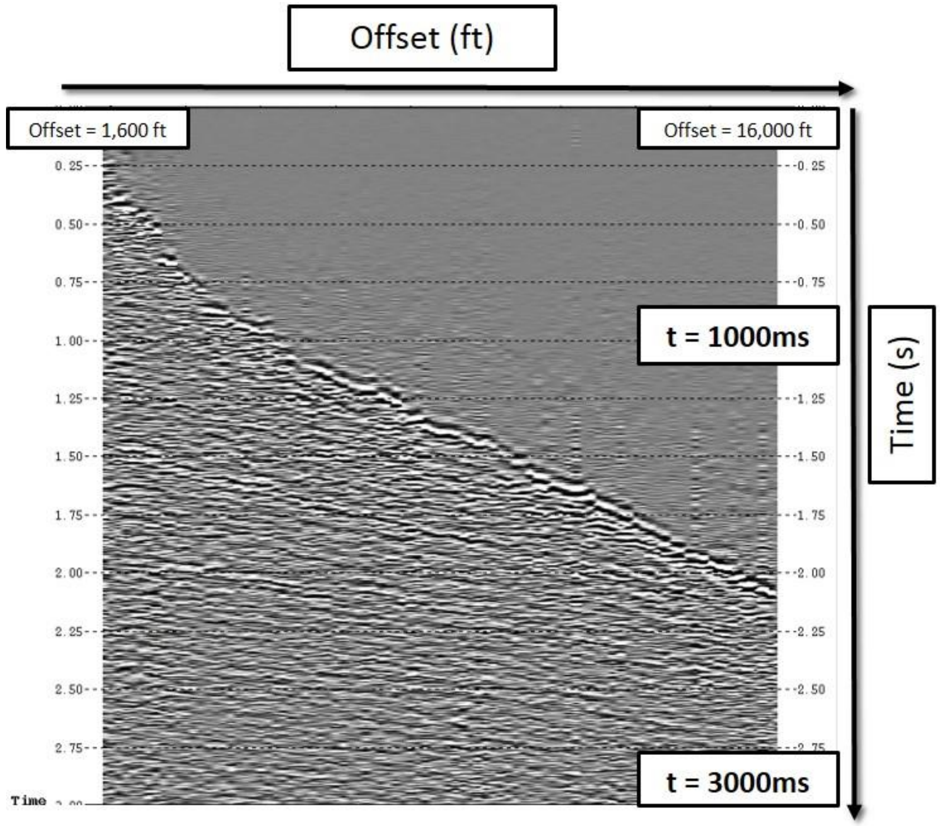

Figure 4.13: Raw CMP gather from Red Sky 3D dataset.

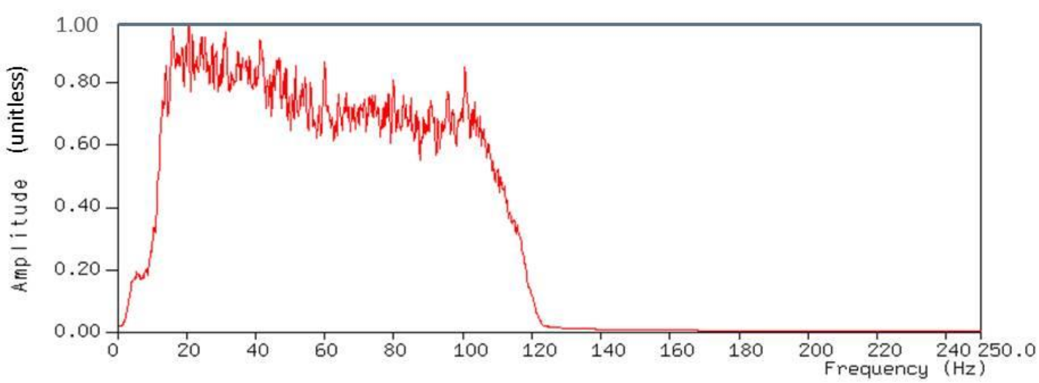

Figure 4.14: Corresponding frequency spectrum from CMP gather displayed in Figure 4.15.

On the 3D shot gathers, a band pass filter of 8, 16, 48, and 64 Hz corner frequencies was applied to remove high frequency noise introduced by deconvolution and low-frequency direct arrivals. An amplitude despiking module was also added to remove noise bursts and attenuate and air blast. Figure 4.15 shows a shot gather before and after band-pass filtering and amplitude despiking, it also shows a difference plot.

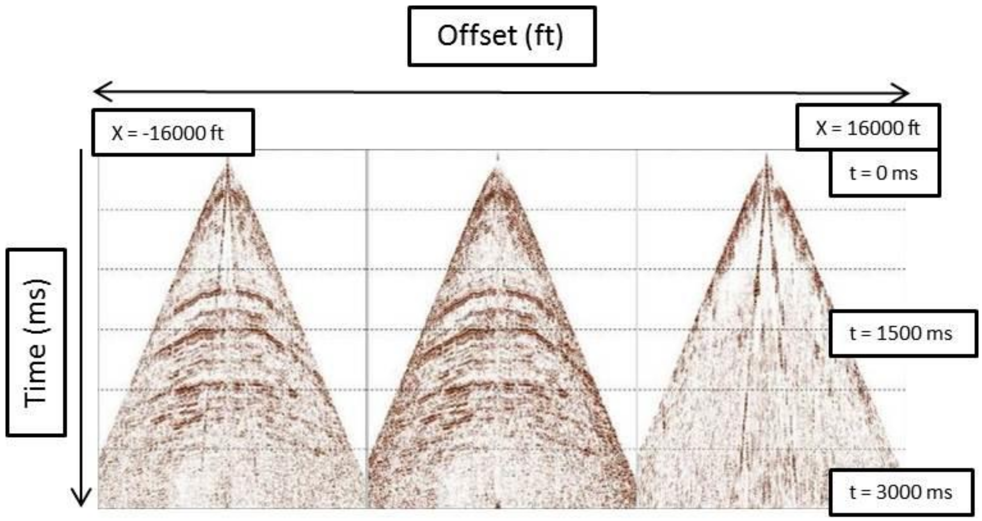

Figure 4.15: Shot gather. a) Before band pass filtering and amplitude despiking; b) after band pass filtering and amplitude despiking; c) difference plot A-B.

A time-frequency domain noise attenuation module was introduced to further remove random noise. This technique also eliminates residual direct arrivals in the data. Figure 4.16 shows the same shot gather before and after time-frequency domain attenuation and also a difference plot.

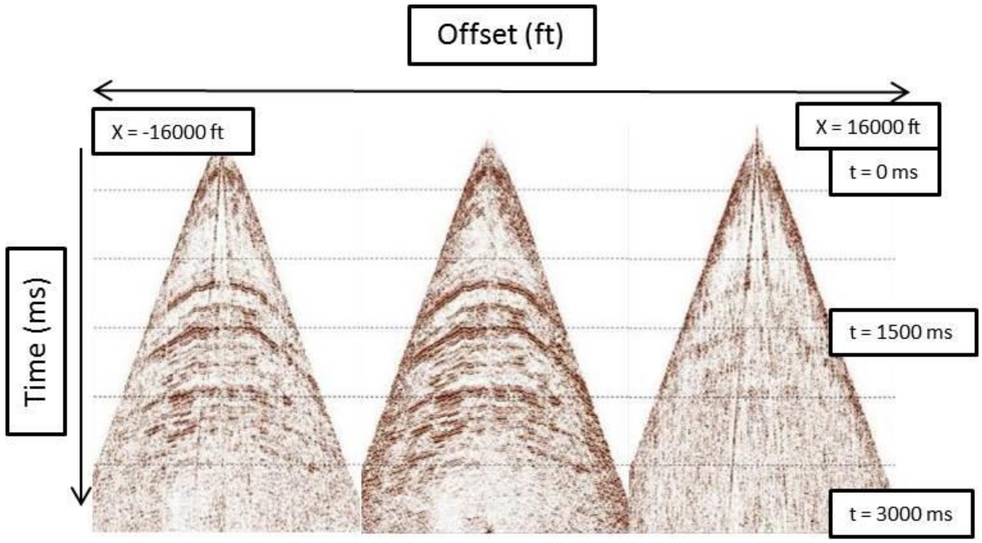

Figure 4.16: Shot gather. a) Before time-frequency domain attenuation; b) after time-frequency domain attenuation; c) difference plot A-B.

Finally, an FX deconvolution module was introduced to enhance signals and further attenuate random noise. Figure 4.17 shows the same shot gather before and after FX deconvolution, a difference plot is also displayed.

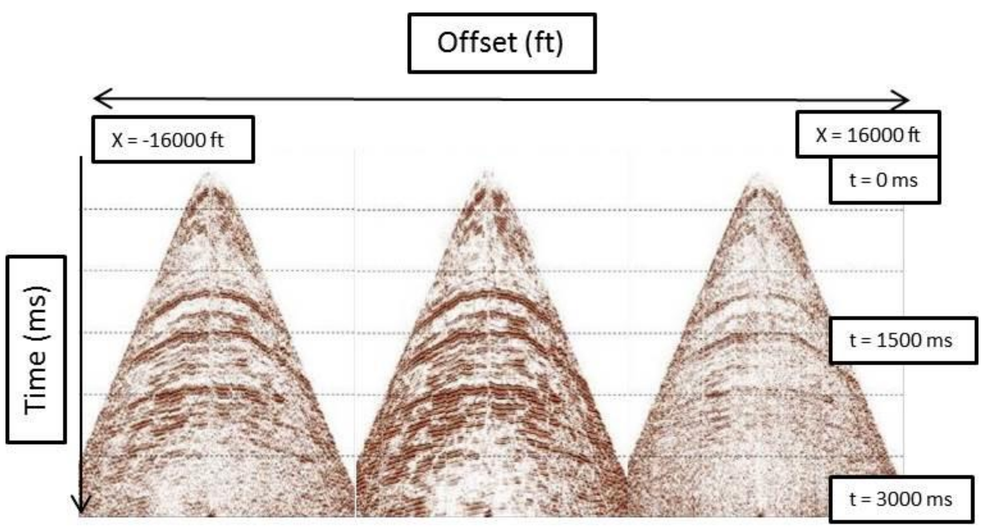

Figure 4.17: Shot gather. a) Before FX deconvolution; b) after FX deconvolution; c) difference plot A-B.

Red Sky 3D data was supplied with correct source-receiver geometry, as a result, CMP sorting was not necessary. Instead, data was imported with CMP as primary sort key when needed. Whenever shot domain processing was needed, the data was simply sorted by shot and input to the processing workflow.

Preliminary velocity analysis on CMP gathers yielded a similar velocity field to Red Sky 2D survey. The exception is the Western (North Western) part of the survey where there is significant dip in most of the reflectors over a large area. The dip itself was about only 0.5° (maximum) in the east-west direction. Velocity values ranged from 4400 to 15000 ft/s (1400 to 4500 m/s). Figure 4.18 shows the stacking velocity analysis window on raw CMP gather (Paradigm GeoDepth® software) from Inline 1070. Inline 1070 was chosen as our velocity line for all processing testing before production or batch processing. This is because of the location of inline 1070 relative to the Red Sky wells. Well V1 is located close to inline 1070. Figure 4.19 shows the stacking velocity field at Inline 1070. In Figure 4.20, we compare a brute stack using a single velocity function to the final Kirchhoff prestack migrated section.

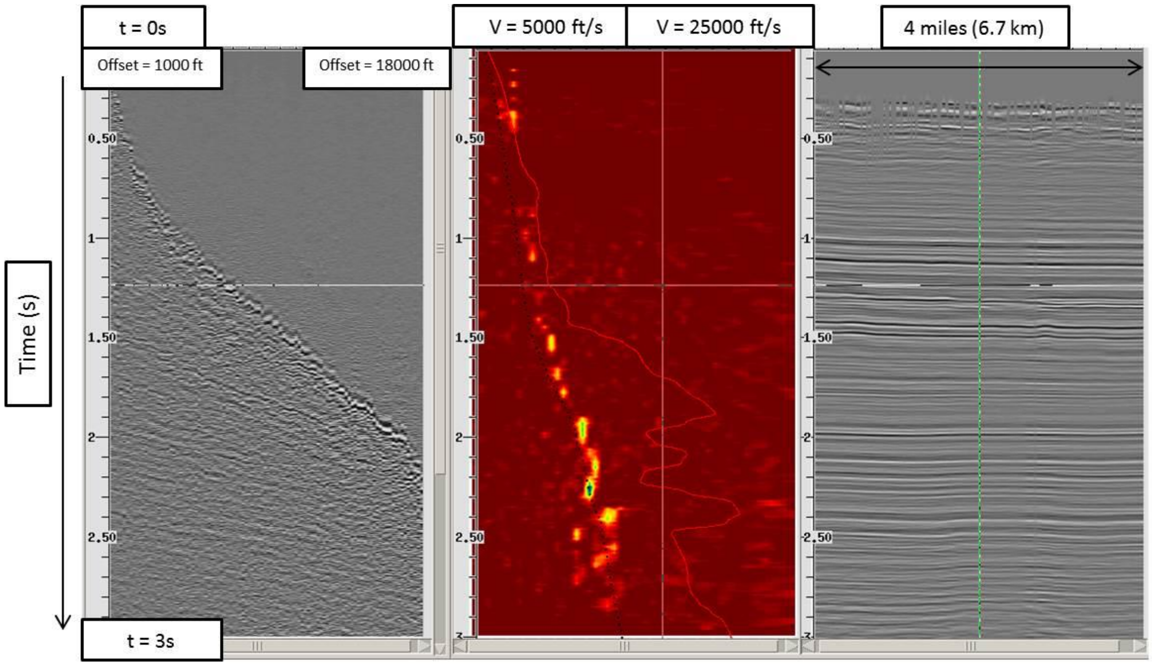

Figure 4.18: Stacking velocity analysis display for a raw CMP gather at Inline 1700 (Paradigm GeoDepth® software). a) CMP stack section; b) stacking velocity semblance plot; c) CMP gather with maximum offset of 18,000 feet (5500 m).

Stacking velocities were assumed to be RMS velocities and these (RMS velocities) were converted to interval velocities using the 1D Dix equation. RMS velocities were input to a Kirchhoff pre-stack time-migration application. The stacking velocity was used to create a brute stack after noise attenuation.

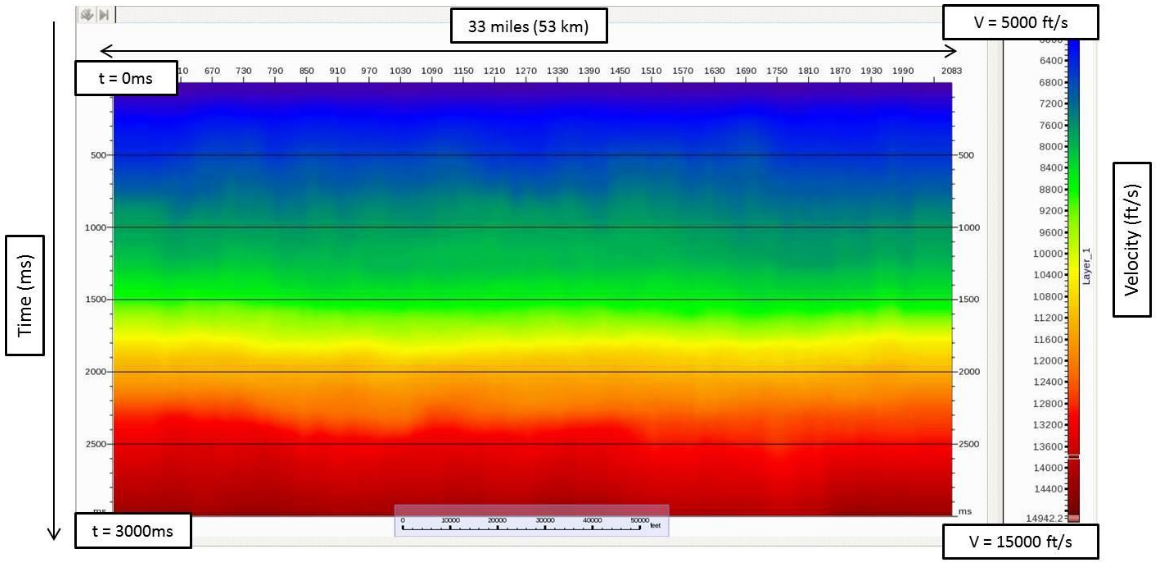

Figure 4.19: Final stacking velocity section for Inline 1070.

Figure 4.21 shows brute stack section as well as final migrated section from Inline 1070.

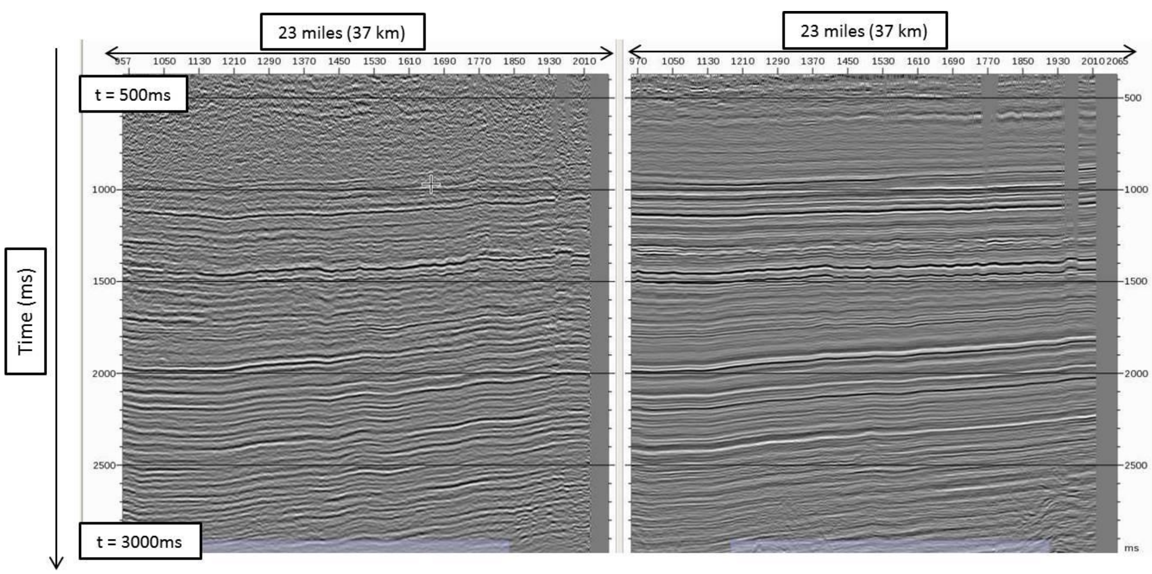

Figure 4.20: Processed sections from Inline 1070. a) Brute stack after noise attenuation; b) Final Kirchhoff PSTM migrated section.

Migrated gathers in the Red Sky survey show significant non-hyperbolic moveout due to the effects of long offset and VTI anisotropy. Figure 4.21 shows Kirchhoff-migrated PSTM gathers in Inline 1070. Notice the "hockey stick" effects at mid-far/far offsets. Normally, these long offset (or VTI) effects will be muted before stacking.

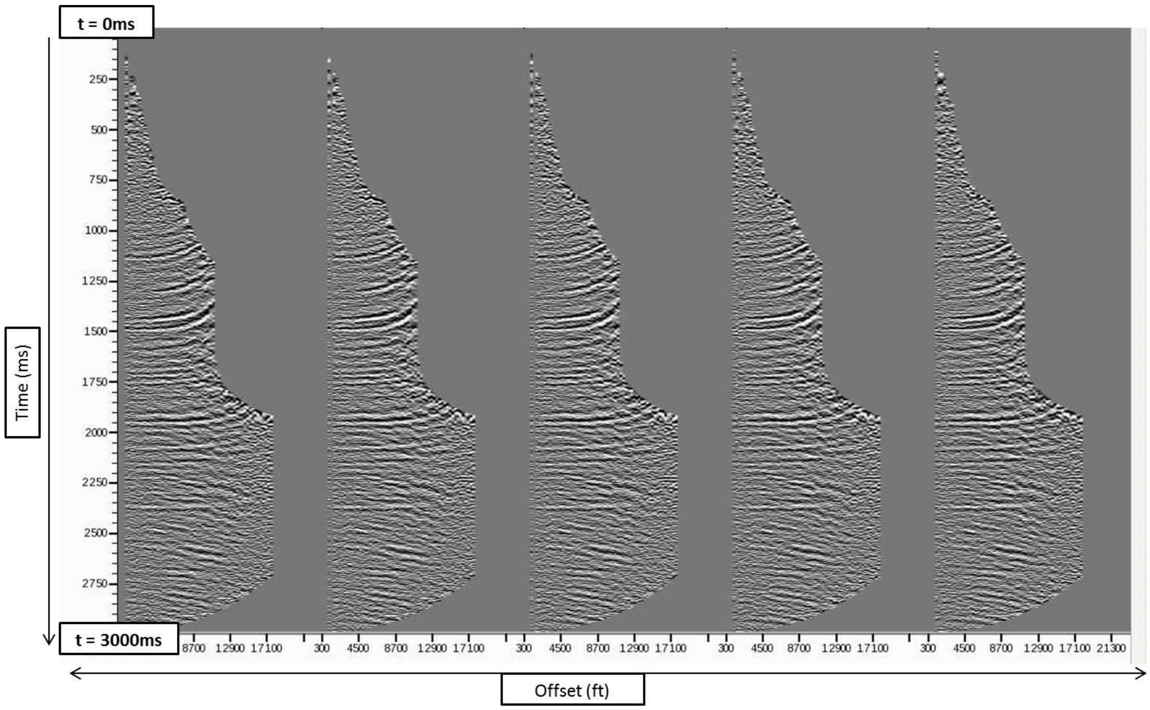

Figure 4.21: Kirchhoff-migrated PSTM gathers from Inline 1070. Offset range is from 300 ft (90 m) to 17100 ft (5200 m).

4.6 Seismic interpretation

To be able to accurately identify events on the Red Sky migrated section, a seismic-to-well tie workflow was initiated. After this process, seismic horizons corresponding to the Greenhorn, Base of Last Salt, Lodgepole, Three Forks, and the top Bakken Formations can be identified with a higher level of confidence. Figure 4.22 shows a seismic-to-well tie panel.

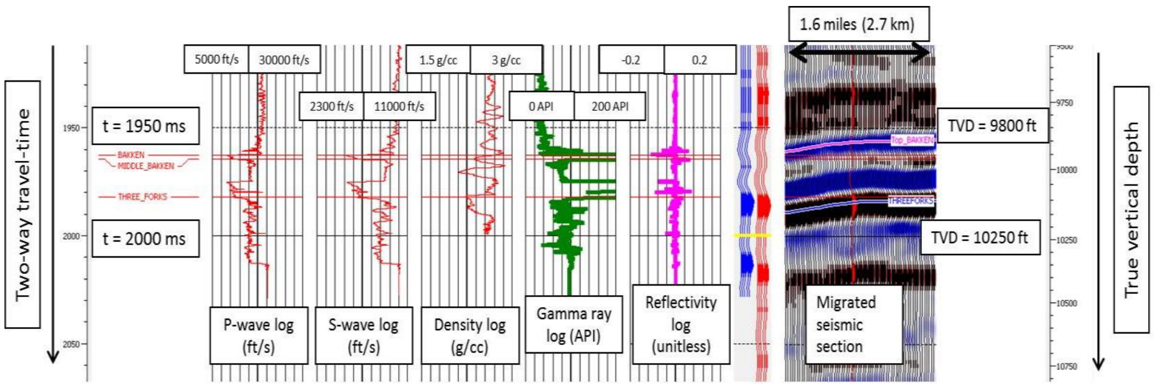

Figure 4.22: Seismic-to-well tie window showing logs and corresponding seismic section for well V1. Display from Hampson-Russell® software.

With the guidance of the seismic-to-well tie results, horizons were picked at the positions Greenhorn, Base of Last Salt, Lodgepole, Three Forks, and the top Bakken Formations. Figure 4.23 shows a time structure map of the Bakken with locations of all supplied wells.

.

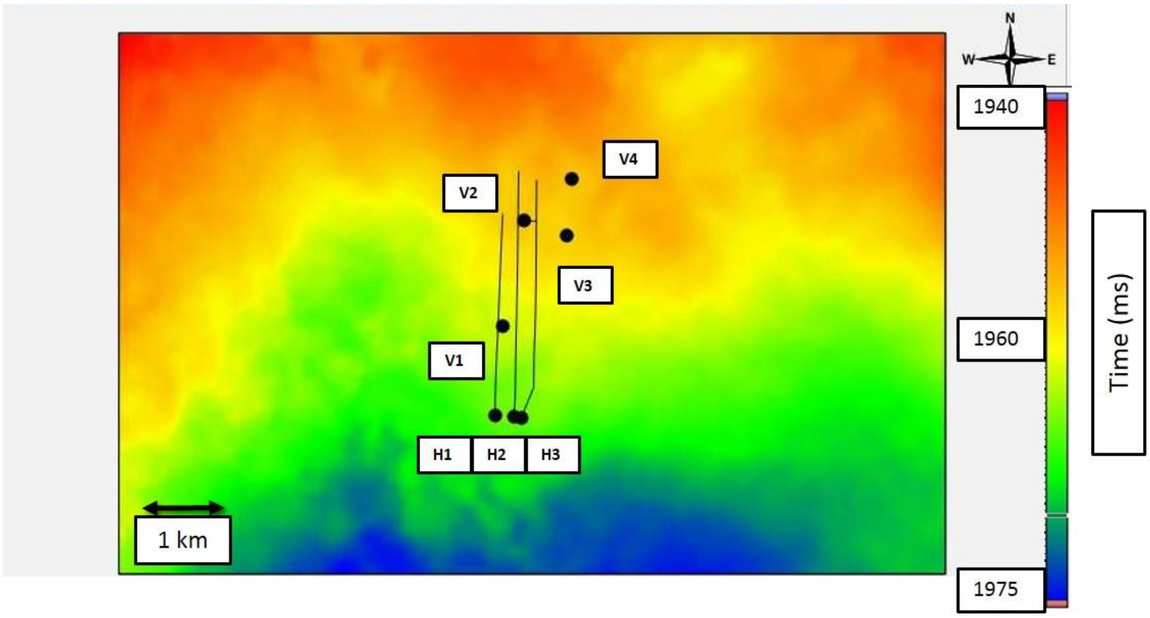

Figure 4.23: Time structure map of the Bakken showing position of all supplied wells in the Red Sky survey. Display from Paradigm GeoDepth® software.

Figure 4.24 shows a seismic section with picked horizons from the Greenhorn, Base of Last Salt, Three Forks and the top Bakken Formations.

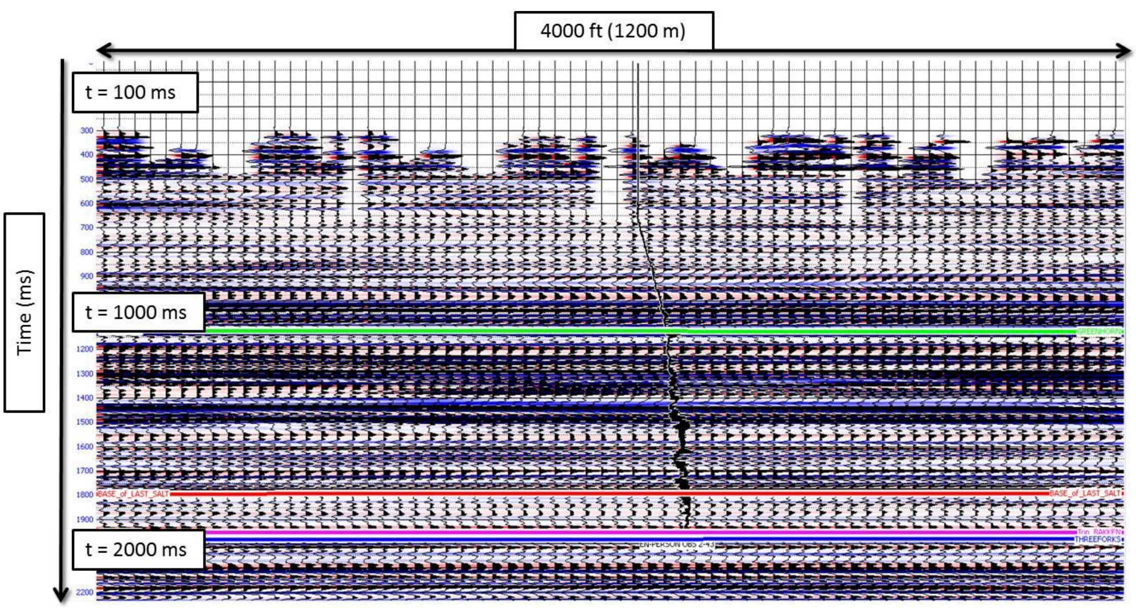

Figure 4.24: Migrated seismic section showing picked horizons from the Greenhorn, Base of Last Salt, Three Forks, and the top Bakken Formations.

Finally, amplitude (and other seismic attributes) was extracted along the picked horizons. Figure 4.25 shows extracted amplitude at the top Bakken.

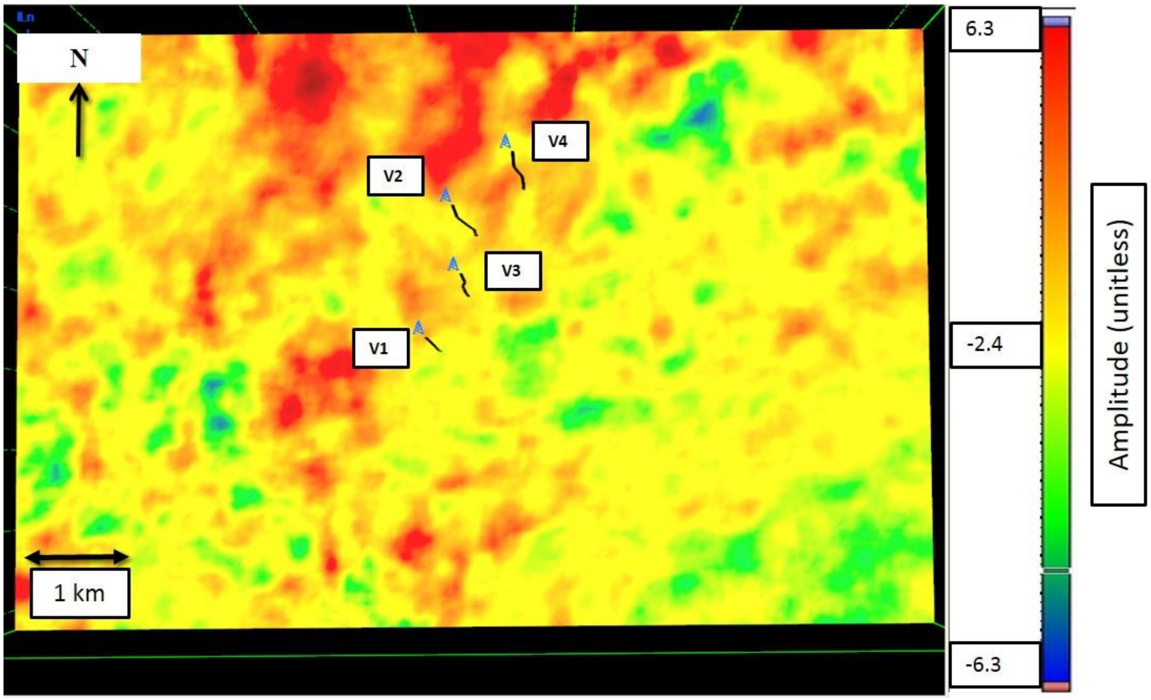

Figure 4.25: Amplitude map of the top Bakken showing position of supplied wells.

4.7 Analysis of NMO ellipses

The use of wide-azimuth prestack seismic data to uncover orientation and direction of fractures/stress has been gaining prominence, (Lynn et al., 1995). Also, advances in land and marine acquisition, as well as the onset of unconventionals or shale plays, have led to a rise in wide- or rich-azimuth seismic data acquisition. Here, we present workflows and processing steps for extracting NMO ellipses using wide-azimuth data from the Williston Basin (Bakken shale play).

An NMO ellipse can be loosely defined as a plot of the trend of NMO velocity with azimuth. Following Tsvankin and Grechka (2011), we analyzed normal moveout (NMO) patterns in the wide-azimuth Red Sky 3D data.

Azimuthal variation in NMO velocities can be caused by the following factors: 1) apparent azimuthal anisotropy, 2) dip and 3) lateral heterogeneity (Grechka and Tsvankin, 1998a). All three factors are important and weigh heavily on results. Since characterizing azimuthal anisotropy is almost always our desired goal, much care must be taken to compensate for dips and lateral heterogeneity when they are encountered. In our case study (Williston Basin), we find very little evidence of lateral heterogeneity and dip ranges mostly from 0.1 to 0.5 degrees. Figure 4.25 shows a view of the top Bakken event shaded in dip (dip legend on right). Notice most of the Top Bakken dip map is green to yellow (0.2 to 0.5 degrees).

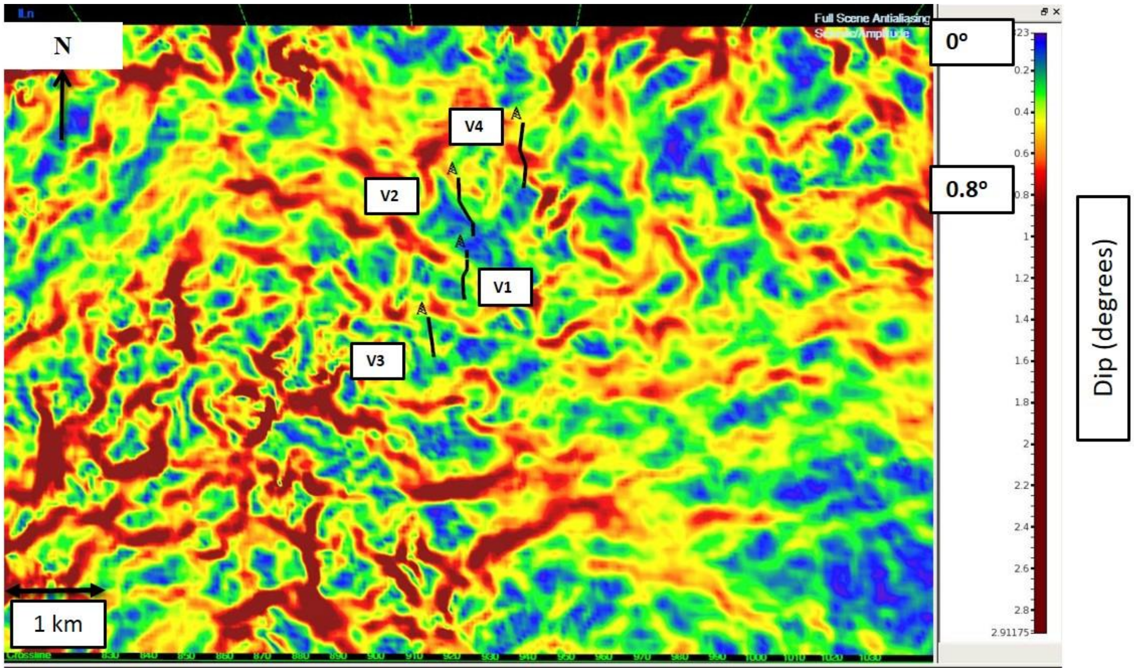

Figure 4.25: Dip map of the Top Bakken. Display from Paradigm GeoDepth® software.

Off all the wells analyzed (Figure 4.25), well V4 appears to be nearest to a feature of higher dip magnitude (dip ≈ 0.5°)

In the absence of a significant dip and lateral heterogeneity, we can express moveout time as a hyperbolic equation, (Grechka and Tsvankin, 1999b);

$$\mathbf{t^2(\phi) = t_0^2 + \frac{x^2}{V_{nmo}^2(\phi)}} \tag{4.1}$$

Where, x is the source-receiver offset, V_{nmo} is normal moveout velocity, t_o is the zero offset travel time and $\boldsymbol{\phi}$ is the source-receiver azimuth.

4.7.1 Data preparation and the NMO ellipse computation workflow

Azimuthal sectoring is a necessary prerequisite for azimuthal NMO analysis. Care must be taken during this stage to make sure azimuth sectors are robust enough to image desired anisotropic attributes. Very small azimuthal sectors tend to yield unstable results and there may not be sufficient offset coverage to compute NMO velocities (for example). Larger azimuthal sectors would also yield ambiguous results. An *a priori* knowledge of the orientation of desired structure/property (e.g. fracture/stress direction from outcrops) might help with the choice of azimuth sectors. More often, fold and azimuthal coverage of wide-azimuth data will determine what the minimum azimuthal sector will be.

In the Williston Basin case study, our chosen azimuthal sector is 20^o. This resulted from experimentation and detailed study of the wide-azimuth data. An illustration of a 20^o azimuthal sector from a single CDP location is provided in Figure 4.26. In all there were 9 azimuthal sectors. Sector 1 contained azimuths $0^o \rightarrow 20^o$ and $180^o \rightarrow 200^o$.

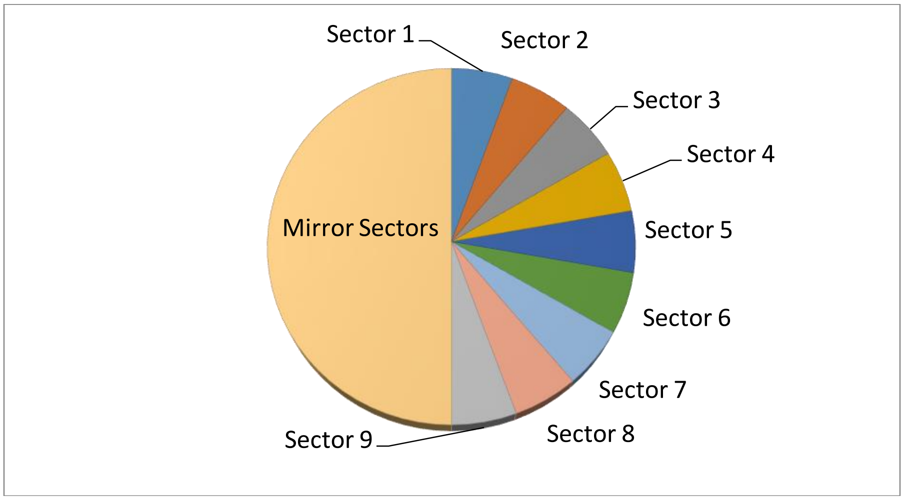

Figure 4.26: Pictorial illustration of chosen azimuth sectors in the Red Sky survey.

In the Red Sky survey, the average fold is 90 (maximum fold is 110). A 20^o azimuthal sector will mean a CMP gather with even distribution of source-receiver azimuths will have just 10 traces for every azimuth sector. Figure 4.27 shows source-receiver pairs from a single CMP gather in the Red Sky survey (overlaid on a fold map), blue lines are source-receiver pairs that fall into the first azimuth sector (black triangle): 0º to 20º (and 180º to 200º)

After the process of azimuthal sectoring, the need arises to increase the fold of the decimated dataset to enable stability in results. A super gather is commonly used in this case to boost the fold of the data.

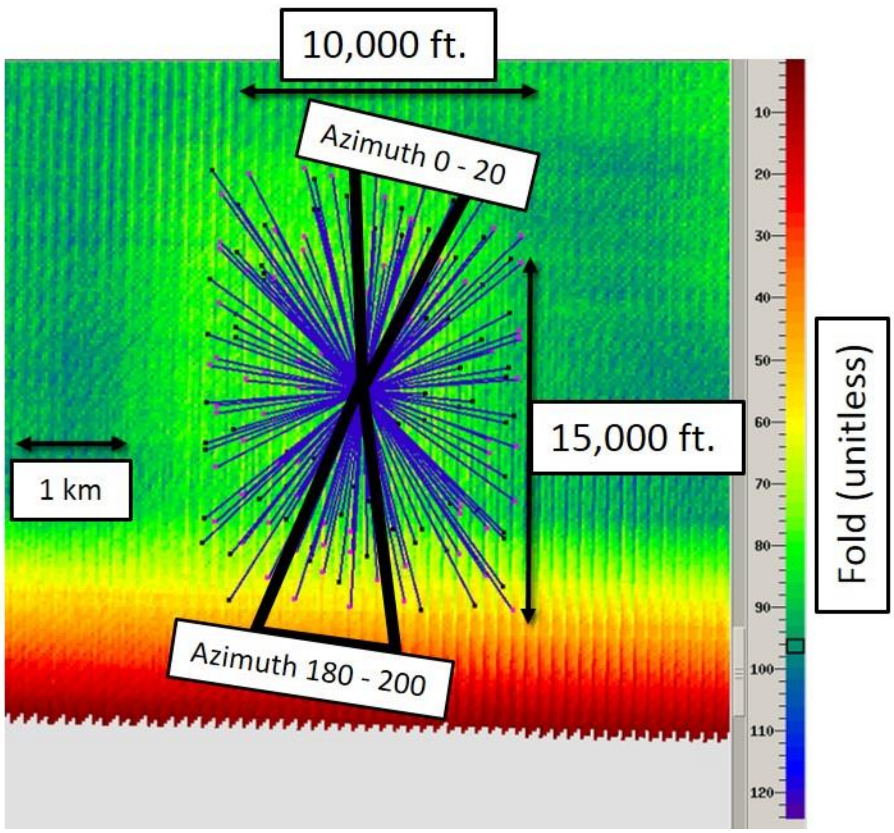

Figure 4.27: Fold map of a subset of the Red Sky survey showing source-receiver pairs and azimuthal sectors (0º to 20º and 180º to 200º).

In a super gather, neighboring CMPs are re-binned into the target CMP to increase fold and ensure stability of results. In our case, we re-binned all single surrounding bins to our target CMP bin. This makes our super gather the size of 9 CMPs (or 330 ft x 330 ft / 100m x 100 m).

We also introduce the concept of a sliding super gather for azimuthally sectored data. In a sliding super gather, we move the super gather bin window (330 ft x 330 ft OR 100 m x 100 m) across inline, xline or diagonal directions depending on what geologic feature we are trying to image. Figure 4.28 illustrates the concept of a sliding super gather; black stars indicate the position of target CMP/bin.

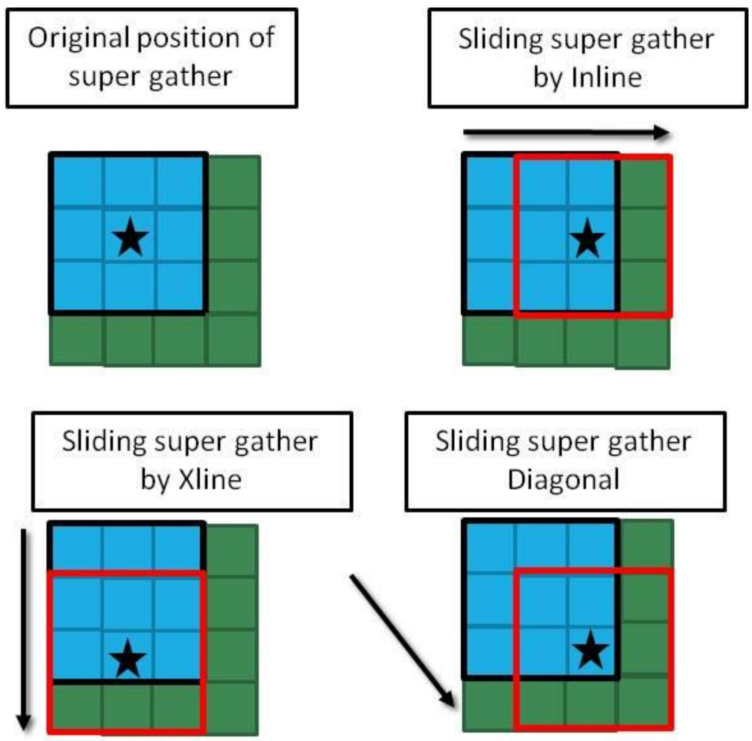

Figure 4.28: Sliding super gather for azimuthally sectored data, showing position of sliding window for inline, xline and diagonal directions. Black star represents position of target CMP/bin.

Using a sliding super gather, we can produce as many super gather CMP locations as conventional/normal CMP locations. Figures 4.29 and 4.30 shows frequency histograms of offset and azimuth distribution for an azimuthally sectored (0^o to 20^o and 180^o to 200^o) super gather.

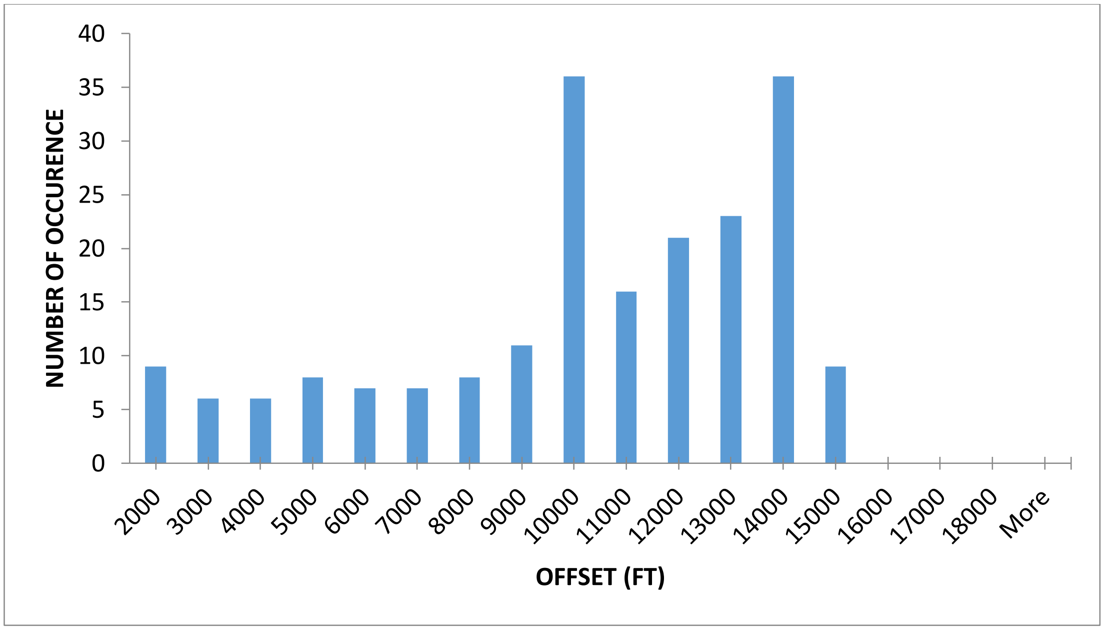

Figure 4.29: Frequency histogram of offset distribution in an azimuthally sectored CMP super gather (0^o to 20^o and 180^o to 200^o).

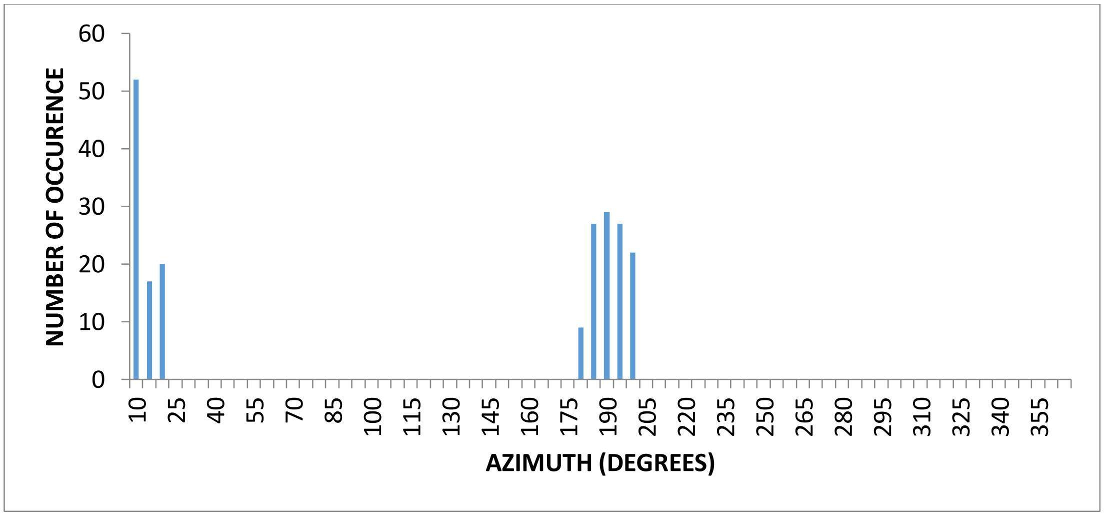

Figure 4.30: Frequency histogram of azimuth distribution in an azimuthally sectored CMP super gather (0^o to 20^o and 180^o to 200^o).

We can observe from the offset histogram that offset coverage seem sufficient for any azimuthal sector in a super gather. With the exception of very far offsets (above 15000 ft / 4500 m), we seem to have a good enough offset representation per azimuthal sector for a stable NMO analysis. Azimuth distribution histogram also shows only desired azimuth are in the dataset (Figure 4.30).

The process of data preparation and processing for creating NMO ellipses is a significant investment in both human and machine resources, but we suggest that the results will be worth the effort (as shown later in this chapter). The practice/workflow will be much smoother if automated, although it may still consume a significant amount of machine time. We now present the processing/workflow step for creating NMO ellipse from data in the Williston Basin in Figure 4.31.

The input to the workflow is CMP gathers from the Red Sky survey after minimal noise attenuation steps (listed in section 4.4.1). Offset-Depth ratio of 1:1 was used to design the mute. This was to ensure far offsets were avoided in the NMO analysis.

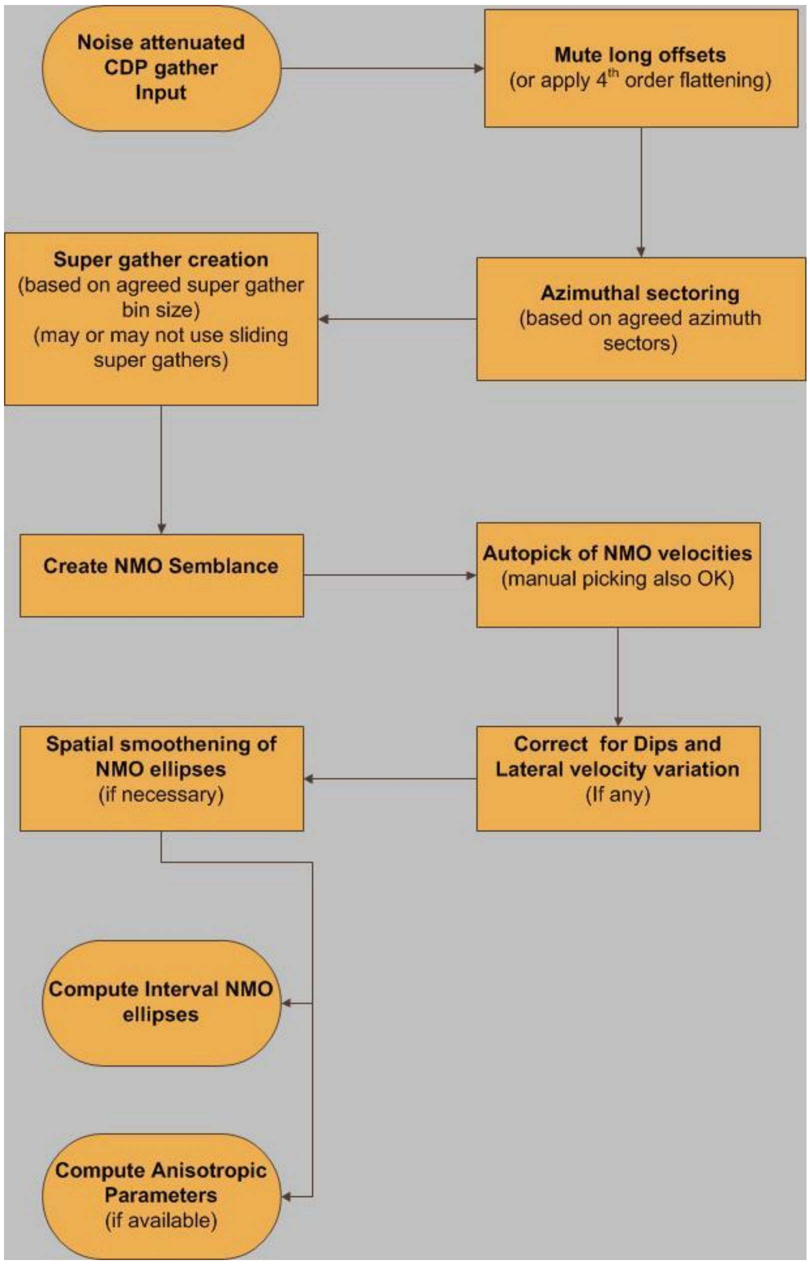

Figure 4.31: Workflow for producing NMO ellipse using data in the Williston Basin.

Figure 4.32 shows NMO semblance panels of slow and fast azimuthally sectored super gathers from the Red Sky survey (Around Well V1). Notice the changes in semblance positions and coherence values at areas near the Base of Greenhorn and Bakken Formations.

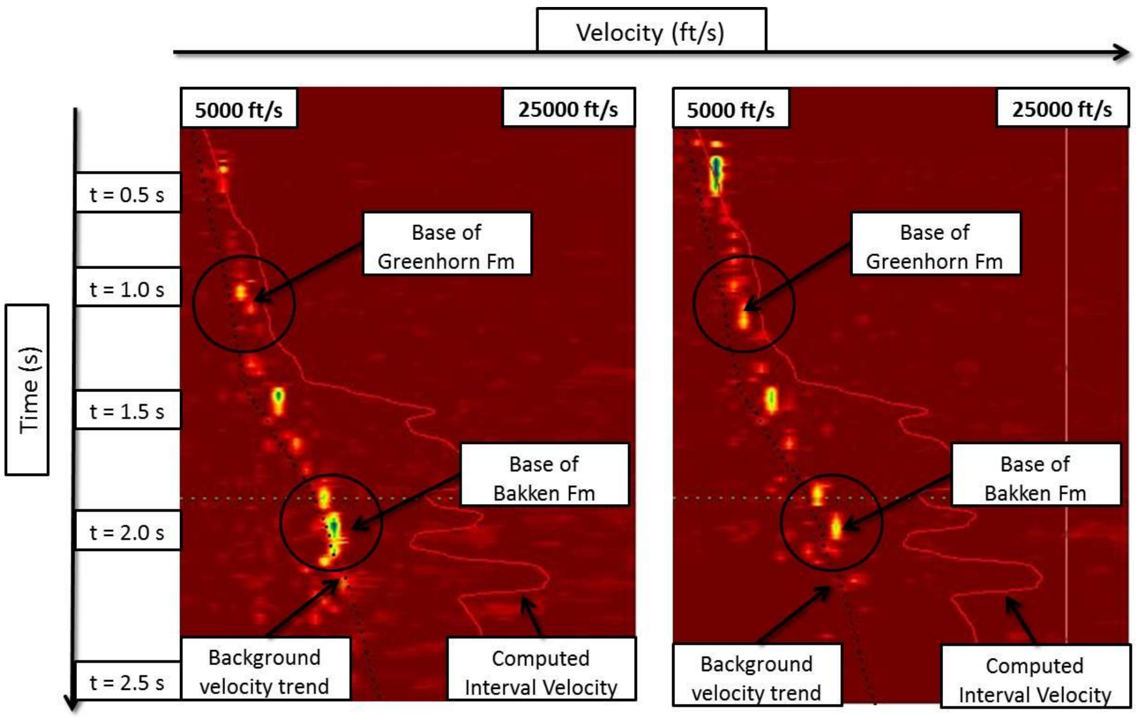

Figure 4.32: Semblance panels computed from slow (left) and fast (right) azimuthally sectored super gathers (0^o to 20^o and 180^o to 200^o) in a CMP bin around well V1. Time range is from 0 to 2.5 seconds.

4.7.2 Results and interpretation of NMO ellipses

Here we present results of NMO ellipses in the vicinity of the four monitoring wells analyzed.

We computed NMO ellipse extracted at travel-times corresponding to the base of the Greenhorn Formation at the nearest CMP (super gather) location to well V1. Figure 4.33 shows the NMO ellipse for the Greenhorn Fm at well V1

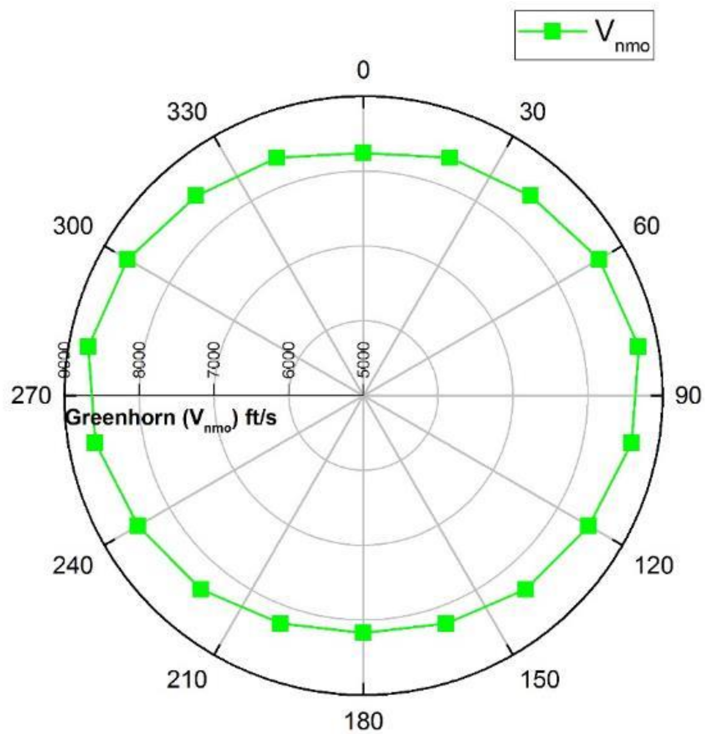

Figure 4.33: P-wave NMO ellipse at travel-times corresponding to the Greenhorn Fm around well V1 (velocity in ft/s).

According to the P-wave NMO ellipse, we can infer the nominal fast direction lies in the 60^{o} to 80^{o} azimuthal sector. Slow direction is approximately orthogonal to the fast direction. The slowness variation (percentage difference between the major and minor axes) is approximately 6%. P-wave NMO ellipses at travel-times corresponding to the base Bakken Formation are presented in Figures 4.34, 4.35, 4.36, and 4.37.

At well location V1, (Figure 4.34) nominal fast direction is about 60º and slowness variation is 3%. At well V2, (Figure 4.35) fast direction remains the same and magnitude of slowness increases to 4%. At nearby well V3 (near to well V2 – Figure 4.36), fast direction seems to change to 80º and magnitude of slowness increases to 5%. Finally at well location V4 (farthest well from the horizontal wells – Figure 4.37), nominal fast direction is at 100º and slowness magnitude is 4%.

In all well locations analyzed, the fast direction seemed to range from 60º to 100º and slowness variation generally ranged from 3% to 5% at the Bakken level.

When interpreting NMO ellipses, it is important to understand underlying assumptions made in the processing sequence that might affect results (Grechka and Tsvankin, 1999a). In our case study, we kept the processing steps to the most minimal and found no need to correct for dips and lateral heterogeneities.

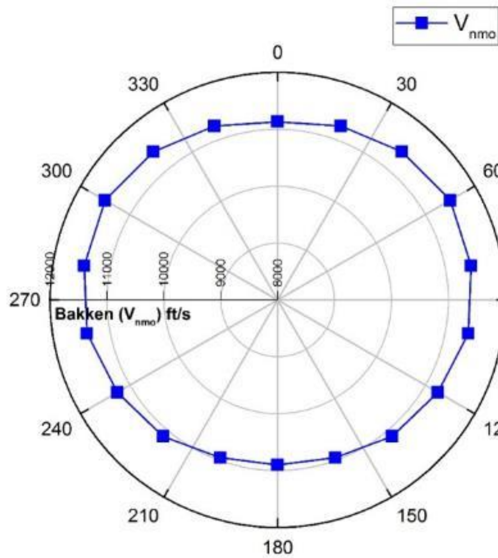

Figure 4.34: P-wave NMO ellipse at travel-times corresponding the Bakken Fm around well V1 (velocity in ft/s).

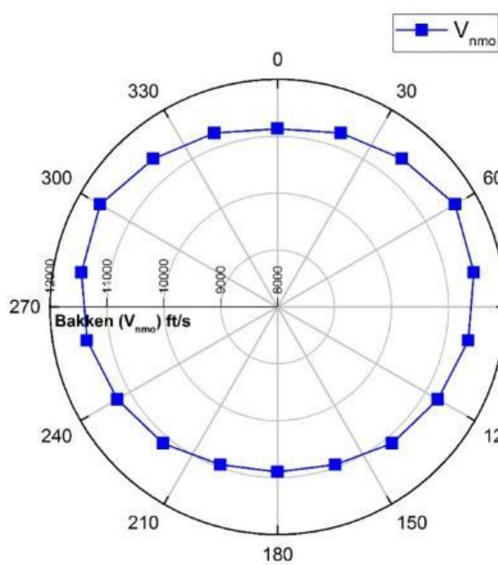

Figure 4.35: P-wave NMO ellipse at travel-times corresponding the Bakken Fm around well V2 (velocity in ft/s).

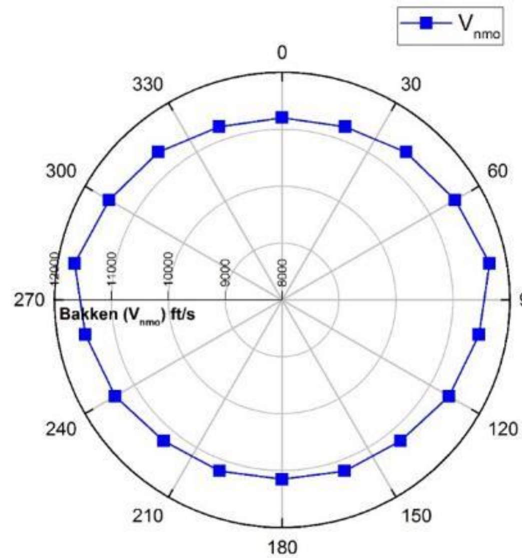

Figure 4.36: P-wave NMO ellipse at travel-times corresponding the Bakken Fm around well V3 (velocity in ft/s).

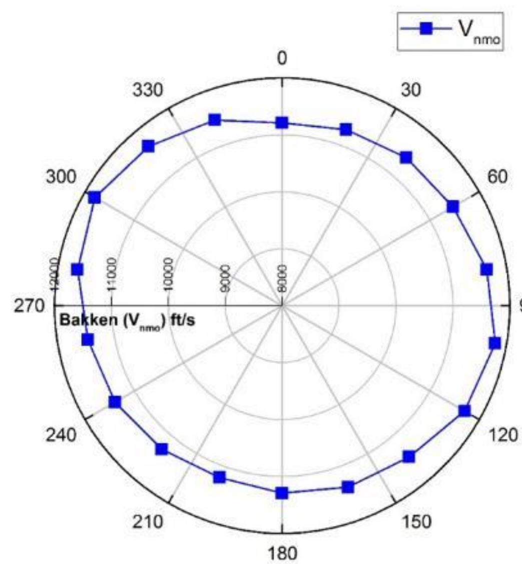

Figure 4.37: P-wave NMO ellipse at travel-times corresponding the Bakken Fm around well V4 (velocity in ft/s).

It is important to compare and calibrate results of NMO ellipses with other data such as outcrop observation, microseismic or VSP data etc. (Grechka and Tsvankin, 1999a). Results from microseismic data indicate the most common fast direction (or direction of maximum horizontal stress - σ_{max}) for the Red Sky survey area is within the range predicted by our P-wave NMO ellipses. Figure 4.38 shows a view of a microseismic stimulation stage showing direction of maximum horizontal stress between 50^o and 70^o. Also rose diagrams computed from FMI image logs near well V1 (Figure 4.39) confirm these directions of maximum horizontal stresses.

In a simplest earth model scenario (layered orthorhombic medium, for example), these percentage slowness of NMO ellipses could correspond to Thomsen's delta (δ^V in orthorhombic symmetry), Grechka and Tsvankin, (1999a).

$$\boldsymbol{\delta}^{\mathbf{v}} = \boldsymbol{\delta}^{\mathbf{3}} = \frac{(\mathbf{C_{12}} + \mathbf{C_{66}})^{\mathbf{2}} - (\mathbf{C_{11}} - \mathbf{C_{66}})^{\mathbf{2}}}{\mathbf{2C_{11}}(\mathbf{C_{11}} - \mathbf{C_{66}})} \qquad (4.2)$$

Definition of terms for orthorhombic symmetry (equation 4.2) can be found in Chapter 1 (section 1.1.2).

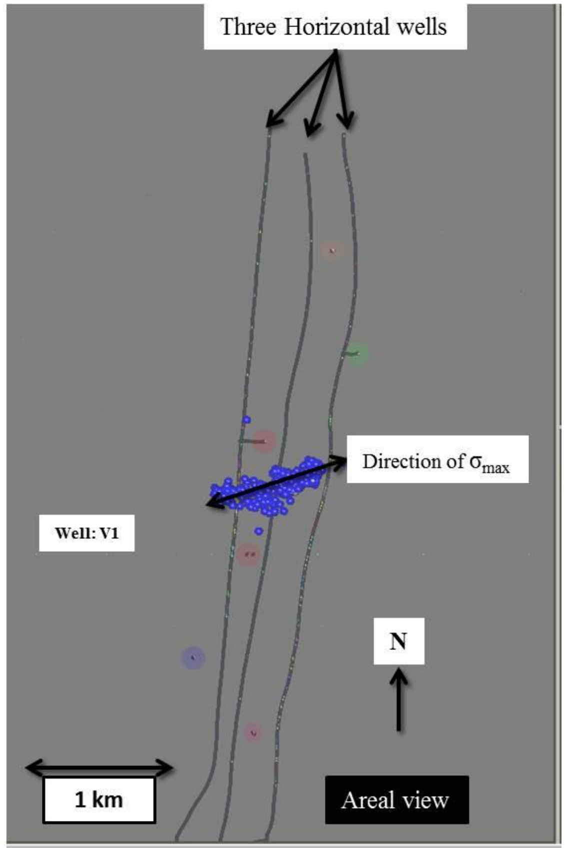

Figure 4.38: Areal view of microseismic event locations from a particular stimulation stage in horizontal well H2 showing direction of maximum horizontal stress.

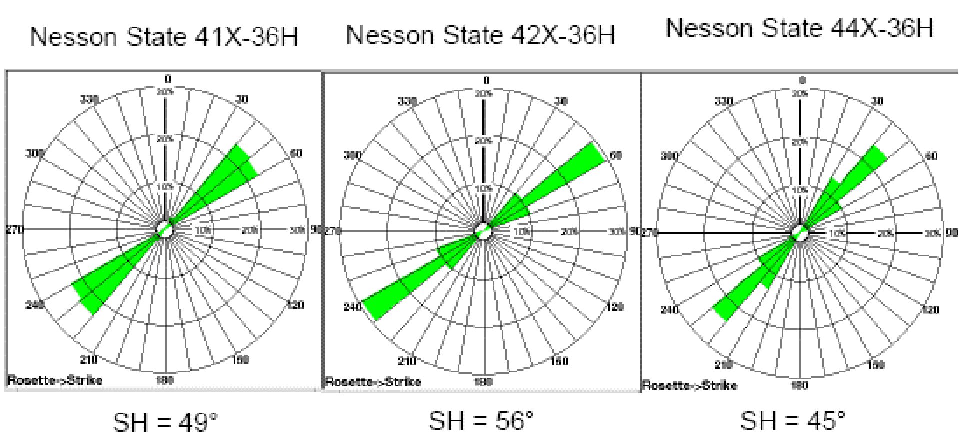

Figure 4.39: Rose diagram computed from FMI image logs in three nearby wells. Modified from Olsen et al., (2009).

Several factors could be responsible for the preferred orientation of the subsurface below the Bakken. Stress could be a factor. The regional stress direction in our area of study is believed to be approximately east-west (due to the proximity of our study area to the Nesson Anticline).

4.8 Contributions and future work

Our field study has investigated changes in NMO velocity as a function of azimuth in a wide-azimuth dataset from the Williston Basin. We also presented a practical production workflow for carrying out azimuthal velocity analysis study in wide-azimuth seismic data. If automated, we believe this method can help create a broad overview of anisotropic trend in the subsurface in a relatively short time and with minimal seismic processing steps needed.

The data analyzed in this chapter come from a frontier wide-azimuth experimental acquisition survey involving wide-azimuth surface seismic/VSP, microseismic data amongst others. One of the goals was to observe the azimuthal and anisotropic trends in the Williston Basin via wide-azimuth surface seismic and VSP. The Red Sky 3D survey is located in the Mountrail County, North Dakota and the survey is about 250 sq. mi in area. Future work on this project will be to create interval NMO ellipses from already created NMO ellipses. Using 1D DIX inversion and chosen geologic intervals of interest, interval NMO ellipses can also be converted to interval velocities in the interval of interest.

Acknowledgements

The authors are grateful to Hess Corporation for donating the dataset for this project. We are also grateful to Paradigm Geophysical and GEDCO for donation of software used for processing and interpretation of this project.

4.9 References

Grechka, V., and I, Tsvankin, 1998, Feasibility of nonhyperbolic moveout inversion in transversely isotropic media. Geophysics. **63**, 957-969

Grechka, V., and I, Tsvankin, 1999, Joint P- and Ps-waves in orthorhombic media: Theory and a physical modeling study. Geophysics. **64**, 146-161

Grechka, V., and I, Tsvankin, 1999, 3D moveout velocity analysis and parameter estimation for orthorhombic media. Geophysics. **64**, 820-837

Grover, P. W., 1996, Stratigraphy and diagenesis of the Mississippian Bakken Shale-Lodgepole Limestone sequence, Williston Basin, North Dakota. Ph.D. dissertation, Texas A&M University, College Station, TX.

Lynn, H. B., C. R. Bates, M. Layman, and M. Jones, 1995, Natural fracture characterization using P-wave reflection seismic data, VSP, borehole imaging logs, and the in-situ stress field determination, SPE paper 29595, presented at the SPE Rocky Mountain Regional/Low-Permeability Reservoirs Symposium, Denver, 20-22 March 1995.

North Dakota Industrial Commission website, accessed May, 2011 (https://www.dmr.nd.gov/ndgs/Resources/WBPetroleumnew.asp).

Pitman, J., L, Price., and J, Lefever., 2001, Diagenesis and Fracture Development in the Bakken Formation, Williston Basin, Implications on Reservoir Quality in the Middle Member. Denver: US Geological Survey, Professional Paper. **1653**.

Pollastro, R.M., L.N.R. Roberts, T. A. Cook, and M.D. Lewan, 2008, Assessment of Undiscovered Technically Recoverable Oil and Gas Resources of the Bakken Formation, Williston Basin, Montana and North Dakota, USGS Open-File Report 2008–1353 Sheet 3 of 3.

Price, L.C., and J. LeFever, 1994, Dysfunctionalism in the Williston Basin: the Bakken/mid-Madison petroleum system. Bulletin of Canadian Petroleum Geology. **42**, 187-218

Sonnenberg, S.A., and A, Pramudito, 2009, Petroleum geology of the giant Elm Coulee field, Williston Basin. AAPG Bulletin, **93**, 1127-1153.

Sonnenberg S.A. 2013. Interest, activity continue in the Bakken. Bakken/Exshaw, the 2103 Playbook. Hart Energy Publication.

Tsvankin, I., and V. Grechka, 2011, Seismology of azimuthally anisotropic media and seismic fracture characterization: SEG, Geophysical Reference Series. **17**.

CHAPTER FIVE

Azimuthally variant attributes and RMO analysis for anisotropic characterization in the Fort Worth Basin

Bode Omoboya[1], Robert R. Stewart[1] and Steven Peterson[2]

[1]- University of Houston, Department of Earth and Atmospheric Sciences, Houston-Texas, USA: Email: bodeomoboya@gmail.com, and rrstewart@uh.edu

[2]- Formerly Marathon Oil Corporation, Houston, Texas, USA: Email sdpeterson3@gmail.com

5.1 Summary

With the advent of unconventional oil and gas exploration in North America, wide-azimuth P-wave data acquisition has become standard practice. Usually the goal is to azimuthally characterize fractures and stress to inform the process of hydraulic fracturing. In the case of a fully developed shale play like the Barnett Formation, the goal is not only to characterize fractures and stress, but there is also need to characterize faults, karst, and chimney structures in both the Barnett and Ellenberger Formations to reduce drilling risk. Using fully processed wide-azimuth 3D dataset and wells from the Fort Worth Basin in Texas, we present a workflow that incorporates residual moveout analysis and azimuthally sectored impedance inversions for deducing the preferred orientation of subsurface anisotropy in the Barnett and Ellenberger Formations. Using *a priori* knowledge of the direction or orientation of natural fractures and stress in the Fort Worth Basin, we created azimuthally sectored seismic data and ran impedance inversion on two different azimuth sectors. We also analyzed residual delays on migrated data from the Fort Worth Basin. Our

residual moveout (RMO) analysis shows promising results: some high RMO values correlated with areas of high dip (around faults and karst), and some other high RMO values were more likely to be influenced by subsurface anisotropy. Attempts were made at using crossplots to help isolate observed anisotropy from the edge of fault and karst structures. Observed azimuthal anisotropic trends need to be investigated in the context of highly dipping structures.

5.2 Introduction

The Barnett Shale play is one of the largest natural gas plays in North America, with about 6 Tcf of natural gas in production and an estimated 20 to 39 Tcf of recoverable reserves (Remington and Simmons, 2009). The Barnett shale play is also an economically mature shale play, with over 11,000 producing wells. However, as is with most other shale plays, spacing and placement of wells can be a statistical process and may not be assisted by geophysics as much as conventional oil and gas developments (Trumbo and Rich, 2013). A general goal is to demonstrate ways in which geophysics can assist in optimizing well placement, as is routinely done in many conventional oil and gas developments.

The availability of wide-azimuth seismic data as well as advances in seismic processing and inversion techniques have made available reliable data necessary for understanding and quantifying seismic anisotropy. Recent studies have also shown that quantitative analysis of azimuthal anisotropy can help delineate orientation and intensity of fractures, as well as fluid infill of cracks.

In this chapter, we compare azimuthally sectored RMO analysis and azimuthally sectored impedance inversions for subsurface characterization. We demonstrate this workflow on the Harris 3D dataset using supplied well information.

We observe interesting trends from RMO analysis results. Some areas of high residual moveouts correspond to areas of highly dipping structures; some others are more likely due to a preferred subsurface orientation which may be due to stress or natural fractures.

The dataset used in this project was supplied by Marathon Oil Corporation.

5.3 Geology of the Fort Worth Basin

The Fort Worth Basin is a mature hydrocarbon basin where oil and gas exploration has been ongoing since the beginning of the 20th century (Pollastro et al. 2007). The Fort Worth Basin is located in the north-central part of the state of Texas. Figure 5.1 shows the location and extent of the Fort Worth Basin as well as the Barnett Shale.

The Barnett Shale is present across most of the Fort Worth Basin. A large share of production in the Barnett is limited to the northern part of the basin, where it is most thick. This area of higher Barnett production is usually referred to as the "core" area (Montgomery et al. 2005).

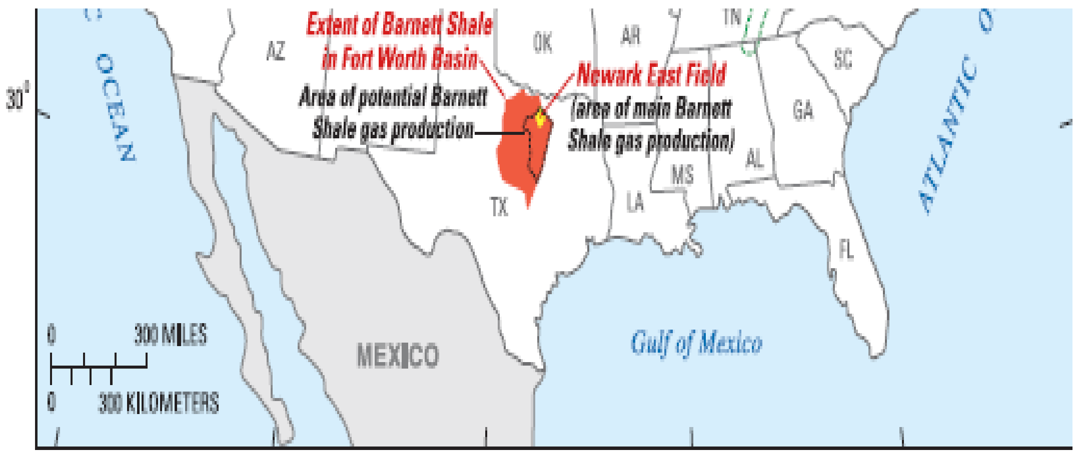

Figure 5.1: Map showing the Fort Worth Basin and extent of the Barnett Shale (modified after Bruner and Smosna, 2011).

The Barnett Shale lies in the Mississippian section of the Fort Worth Basin. Overlying the Barnett Shale in the Fort Worth Basin is the Marble Falls Formation. Within the Barnett, there exists the intervening Forestburg Limestone. In some areas, the Barnett Shale is divided into upper and lower members where the Forestburg Limestone is present. The presence of this limestone serves as a good hydraulic fracturing barrier which may help improve productivity. The Barnett Shale specifically consists of dense, organic-rich, thin-bedded shale (Bruner and Smosna, 2011). Figure 5.2 shows a generalized stratigraphic column of the Fort Worth Basin.

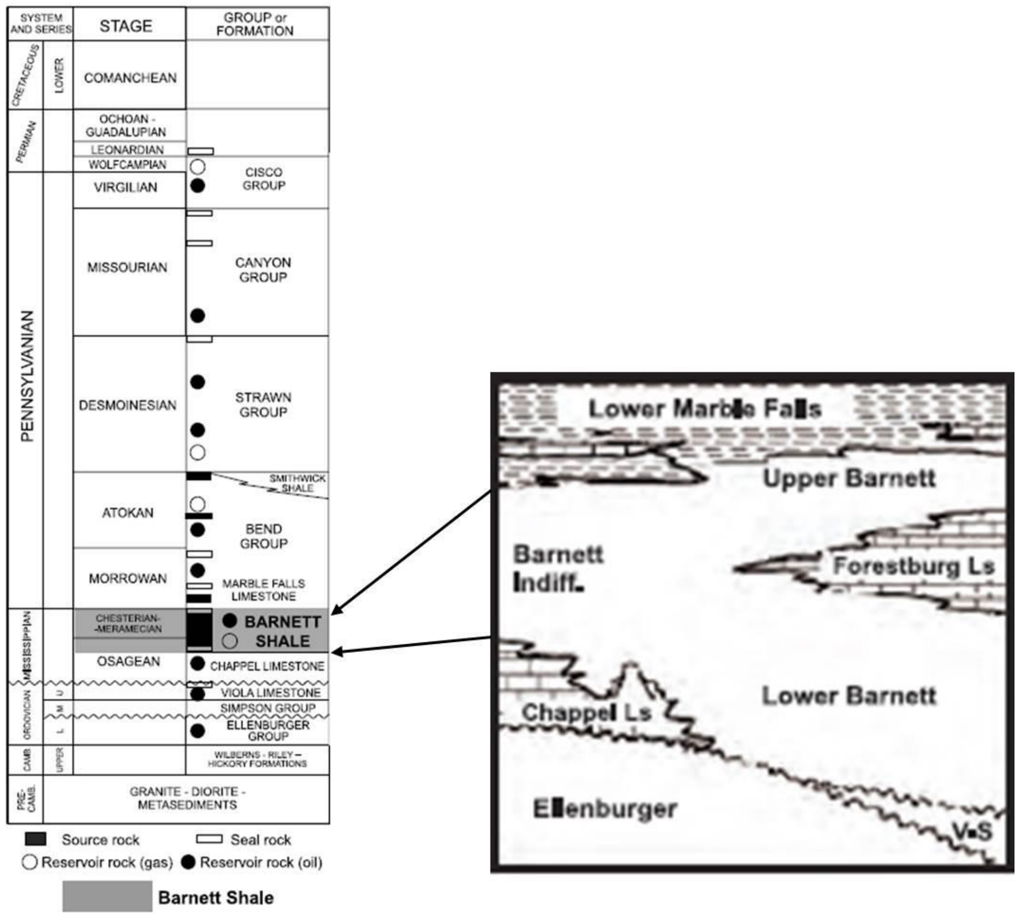

Figure 5.2: Generalized stratigraphic column of the Fort Worth Basin with the Barnett Shale in the expanded section on the right (modified after Montgomery et al. 2005).

The overlying Marble Falls Formation and underlying Ellenberger Formations also serve as seal rocks for hydrocarbon in the Barnett. The Barnett itself serves as both source rock and reservoir rock for oil and gas in the Fort Worth Basin.

Measured porosity in the Barnett is approximately 6%, and water saturation ranges from 20-30%. Thickness of the Barnett ranges from 50-1000 ft (15-300 m). Drilling depth in the Barnett ranges from 4000-8500 ft (1210-2600 m).

The overlying carbonate-rich Marble Falls Formation is mainly limestone. Underlying the Barnett is the karst-rich Ellenberger Formation; water encroachment from the underlying Ellenberger Formation is a drilling risk to production in the Barnett. The presence of karst in the Ellenberger Formation results in high-angle faults, fault chimneys, and subsidence features in the Barnett. These karst and other subsidence features are easily recognizable on seismic data from the Barnett. Dip- and curvature-based seismic attributes can help to adequately map these features as shown later in section 5.6.

Only one set of natural fractures (strike 100^o-120^o) is recognized in the Barnett (Bruner and Smosna, 2011). Natural fractures seem to be more common in limestone interbeds (e.g., the Forestburg Member). Artificial fractures in the Barnett are believed to be oriented in the direction of minimal stress, and their propagation seems to be perpendicular to the direction of prominent natural fractures (Bruner and Smosna, 2011).

5.4 Harris seismic survey and wells

5.4.1 Harris 3D seismic survey

The Harris 3D seismic survey covers an area of about 88 sq. miles (228 sq. km). There are about 34,500 production shots (at 110ft or 33m intervals) and 34,900 live receivers (also at 110ft or 33m intervals). Altogether, there are 1.33 million CDP locations at 55ft (16m) intervals. Inline numbers range from 233 to 1422 and crossline ranges are from 347 to 1468. Tables 5.1 and 5.2 illustrate shot and receiver acquisition parameters for the Harris survey.

Receiver line spacing	660ft (200m)
Receiver spacing	110ft (33m)
Receiver array	6 per group
Receiver line azimuth	NW-SE (Grid Azimuth)

Table 5.1: Receiver geometry for the Harris 3D survey

Shot line spacing	880ft (270m)
Shot point spacing	110ft (33m)
Source type	Vibroseis
Sweep frequency	6-120 Hz
Sweep length/listening time	10/4 seconds
Shot line azimuth	NE-SW (Grid Azimuth)

Table 5.2: Shot geometry for the Harris 3D survey

Figure 5.3 shows a fold map of the Harris survey. Most common fold ranges within the survey are from 40 to 90, while the maximum fold is 92.

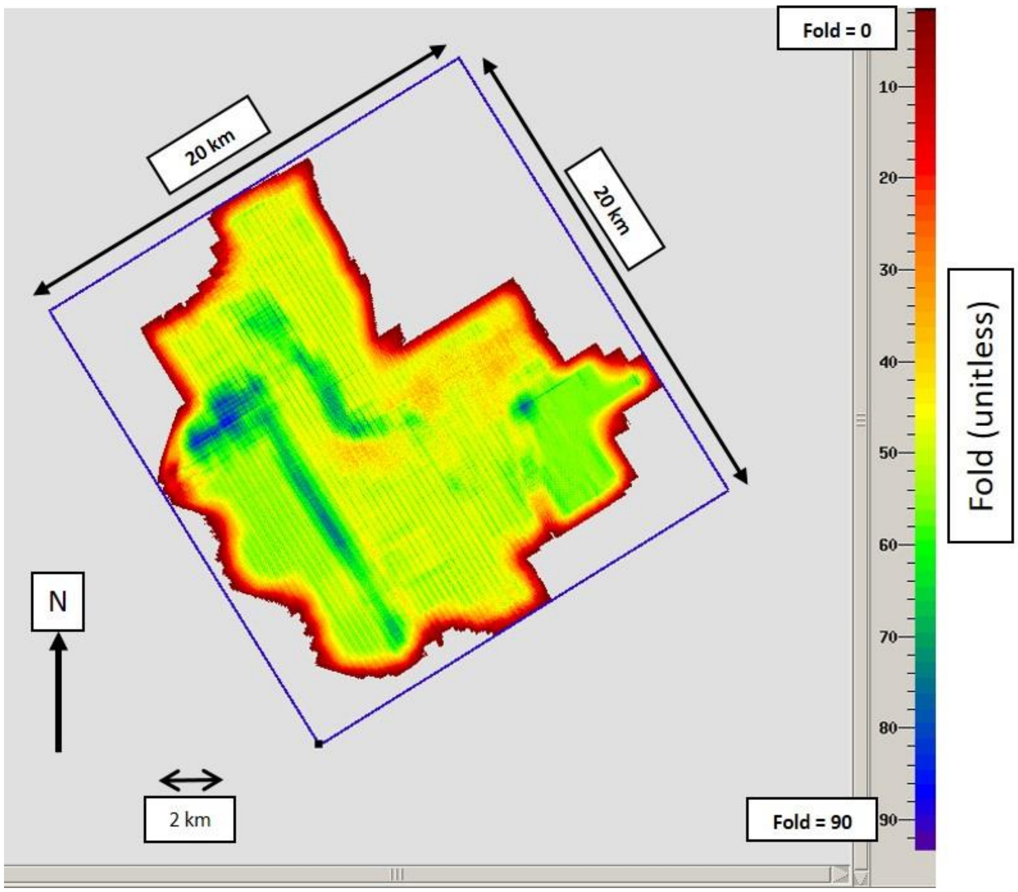

Figure 5.3: Fold map of the Harris 3D survey.

Azimuth and offset distribution in the Harris survey is robust enough for azimuthal and anisotropic studies (including far offset studies). Figures 5.4 and 5.5 show typical azimuth and offset distributions for the Harris 3D survey. The depth to the Barnett shale in our study area is about 3700ft (1130m). Most abundant offsets in the Harris 3D survey area range from 3000ft (915m) to 5500ft (1680m).

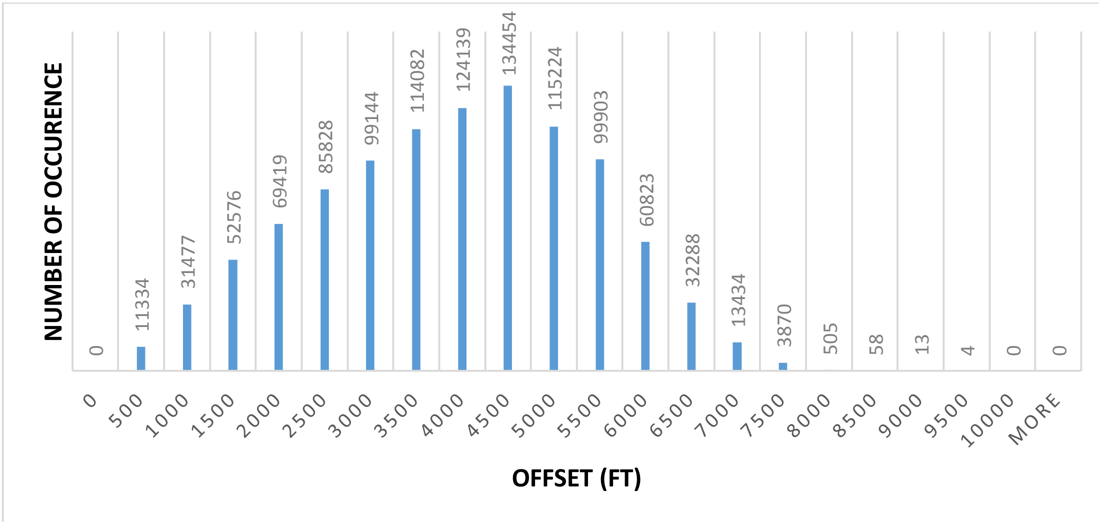

Figure 5.4: Frequency histogram of offset distribution from CDP gathers in the Harris 3D survey.

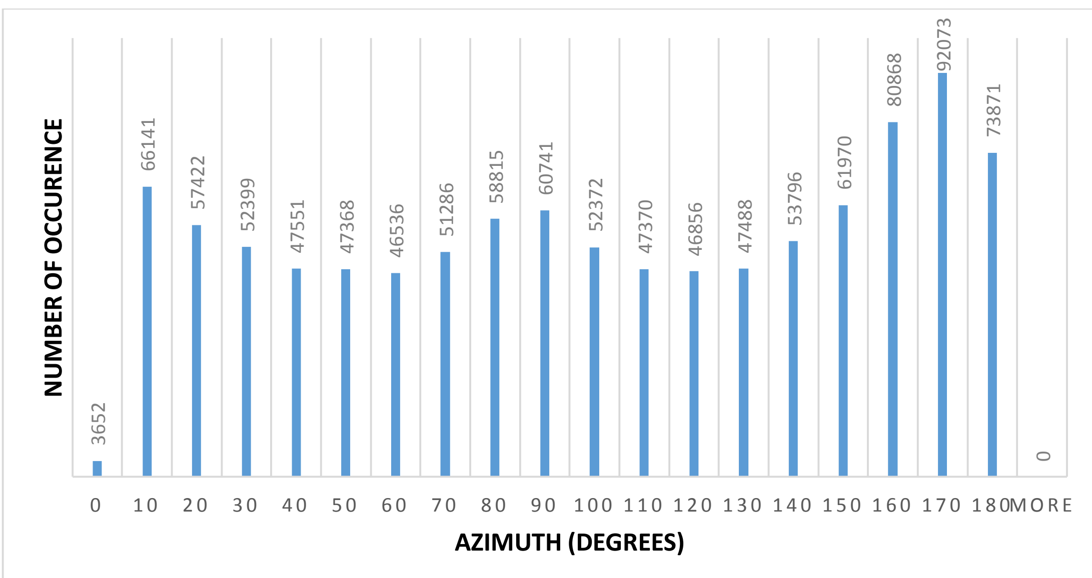

Figure 5.5: Frequency histogram of azimuth (0^o-180^o) distribution from CDP gathers in the Harris 3D survey.

All azimuths displayed in this dissertation are grid azimuths (i.e. azimuths are calculated from X and Y coordinates obtained from SEG-Y trace headers). Most azimuths are sufficiently covered for a robust wide-azimuth study in the Harris survey. Figure 5.6 shows the direction and azimuth of source-receiver pairs originating from one common mid-point (CMP) gather.

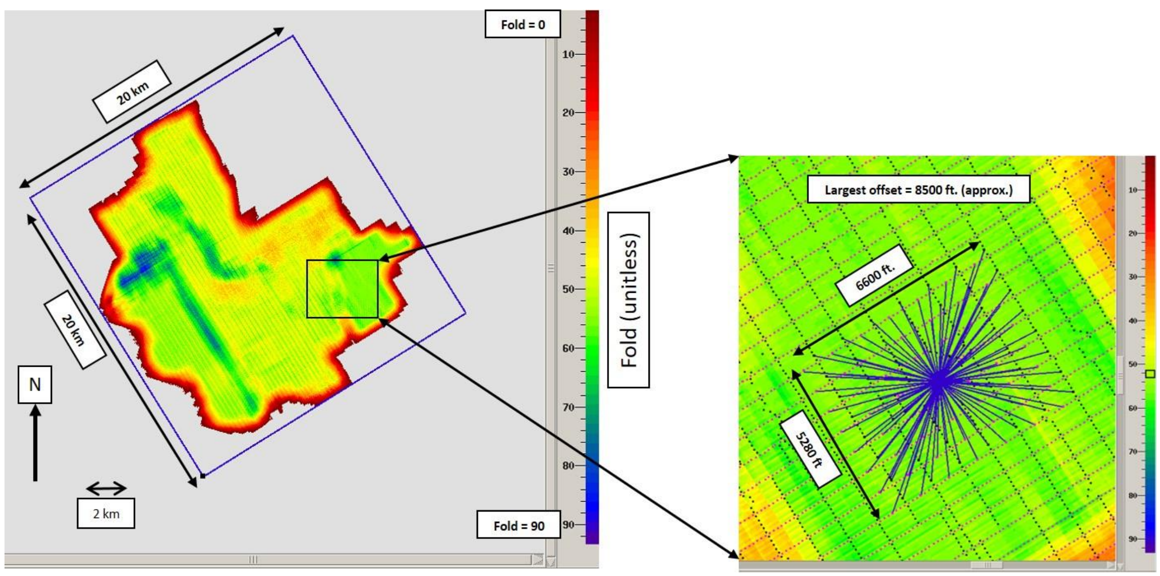

Figure 5.6: Azimuthal distribution of source-receiver pairs from one common mid-point. Background map is a fold map with fold ranging from 10 (red) to 90 (blue).

5.4.2 Harris wells

Three well datasets were supplied with the Harris survey. Table 5.3 shows these wells labelled wells X, Y, and Z, as well as displaying their information. Wells X and Y are about 8.5 miles apart in distance.

Well Name	**TVD**	**MD**	**KB**	**EPD**
X	4422 ft (1347 m)	7925 ft (2415 m)	1129 ft (344 m)	1108 ft (337 m)
Y	4179 ft (1273 m)	7116 ft (2168 m)	1099 ft (334 m)	1085 ft (330 m)
Z	5170 ft (1575 m)	5170 ft (1575 m)	1204 ft (366 m)	1183 ft (360 m)

Table 5.3: Well information for all supplied wells

5.5 Harris seismic processing

The seismic processing techniques undertaken for the Harris 3D survey were conventional and robust enough to incorporate wide-azimuth as well as anisotropic analysis in different stages (if needed). Considerable care was taken to preserve true amplitudes while enhancing key reflectors. The data had geometry already supplied and was CDP sorted. Figure 5.7 shows supplied raw CDP gathers from Inline 1267 (velocity or test line for most of the processing workflow). Figure 5.8 shows the processing flow for the entire Harris survey.

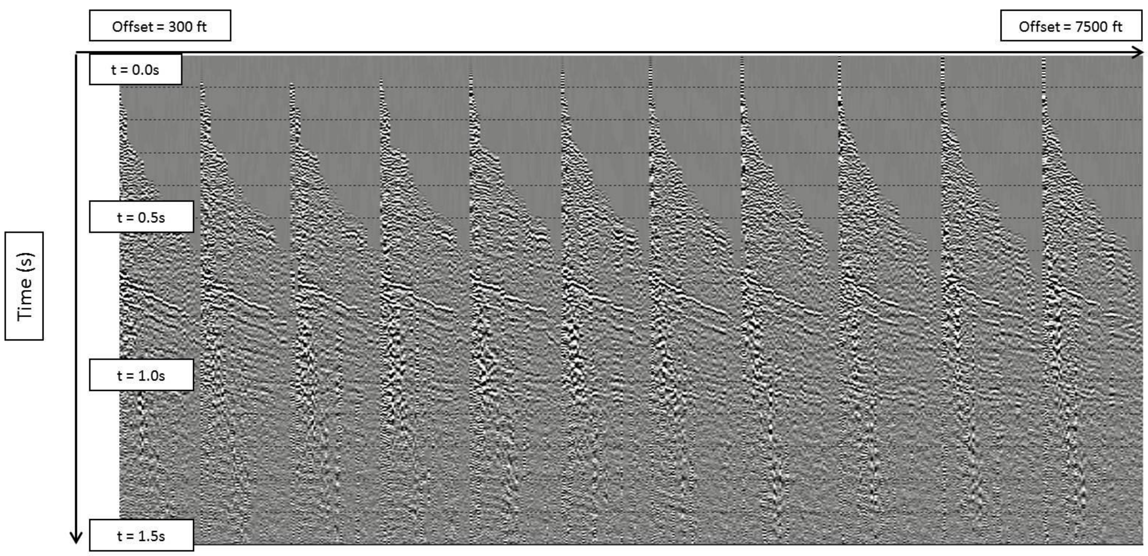

Figure 5.7: Raw CDP Gathers from IL 1267.

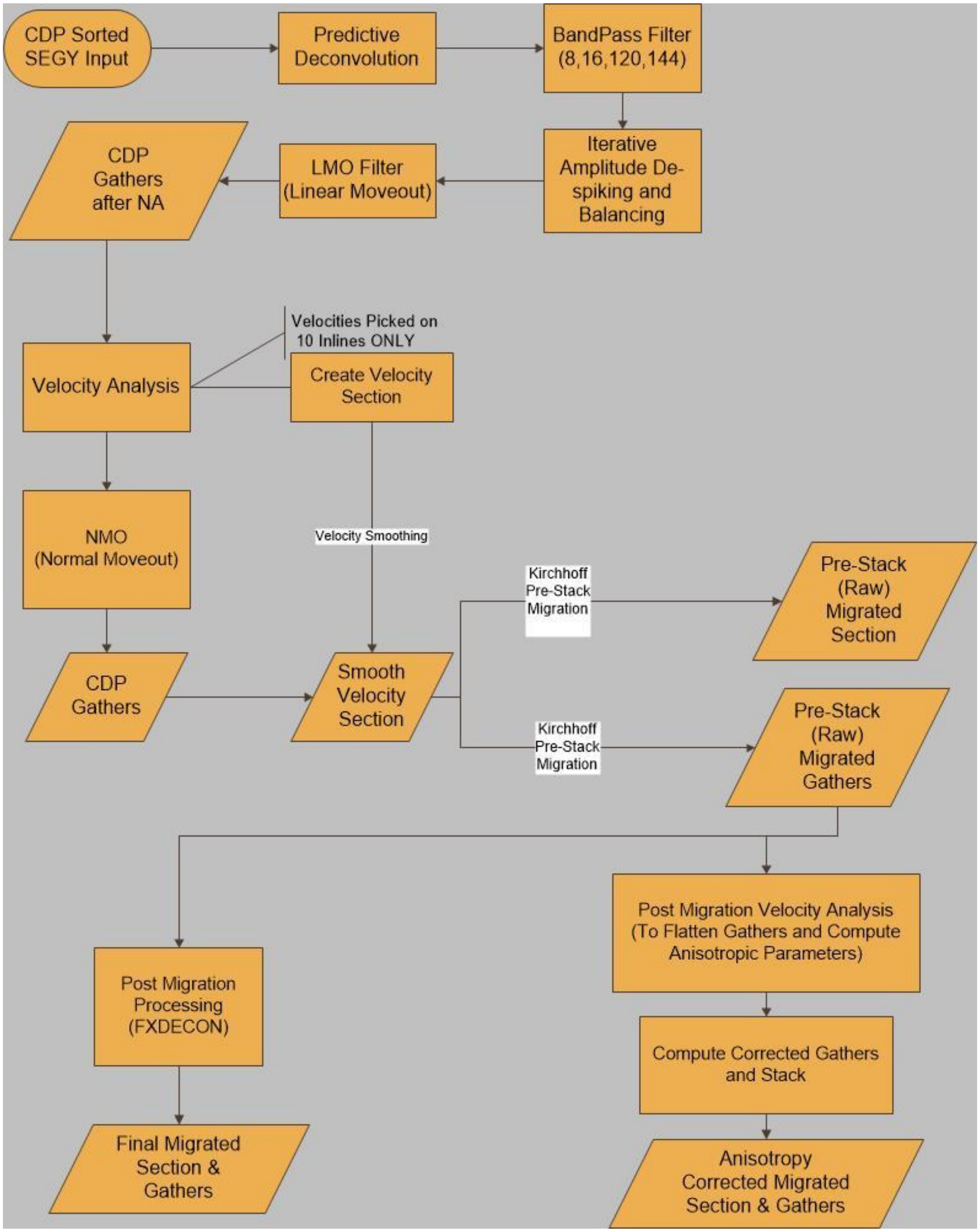

Figure 5.8: Processing flow for Harris 3D survey.

5.5.1 Deconvolution, filtering and noise suppression

Predictive deconvolution was applied to the raw gathers with the intent of preserving amplitudes and enhancing reflectors. Figure 5.9 shows both raw CDP gathers and the same gather after the application of decon and bandpass filtering.

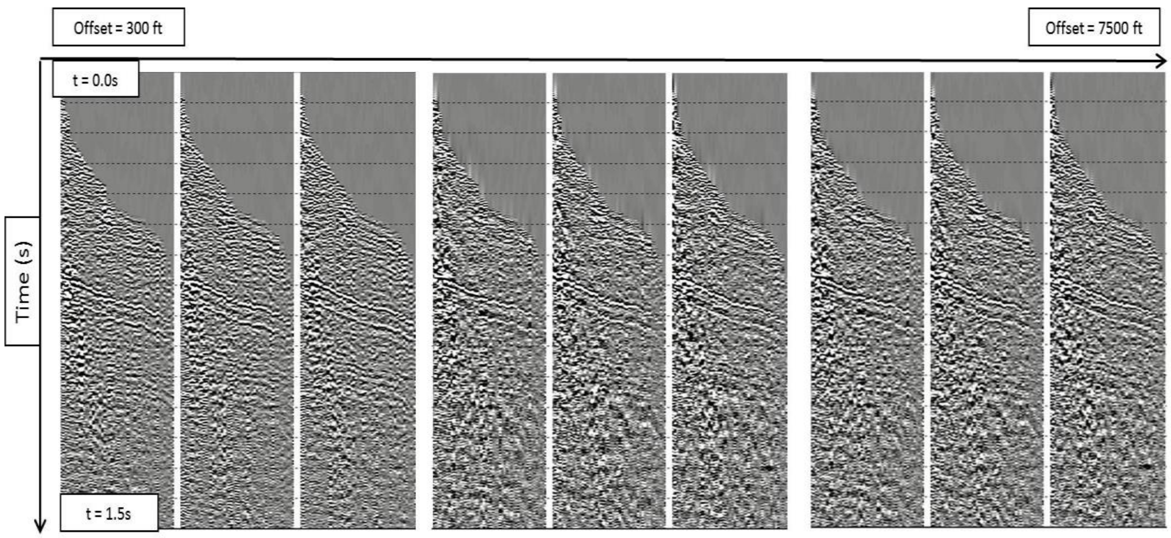

Figure 5.9: Raw CDP gathers before and after application of predictive deconvolution and band-pass filtering.

Iterative amplitude de-spiking was also applied to the dataset as the major noise attenuation technique. This technique was used instead of conventional bad trace editing which is usually labor-intensive and time-consuming. Results of amplitude de-spiking are displayed in Figure 5.10.

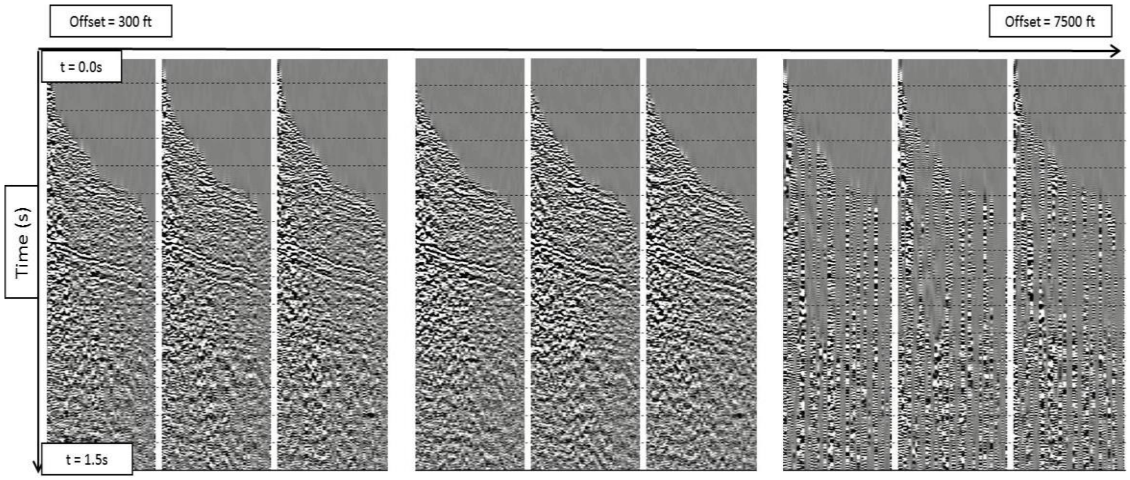

Figure 5.10: CDP gathers before and after iterative amplitude de-spiking and difference plot.

Lastly, Linear Move-out (LMO) filters were applied to remove ground roll and residual linear events. Results of the application of LMO filters are displayed in Figure 5.11.

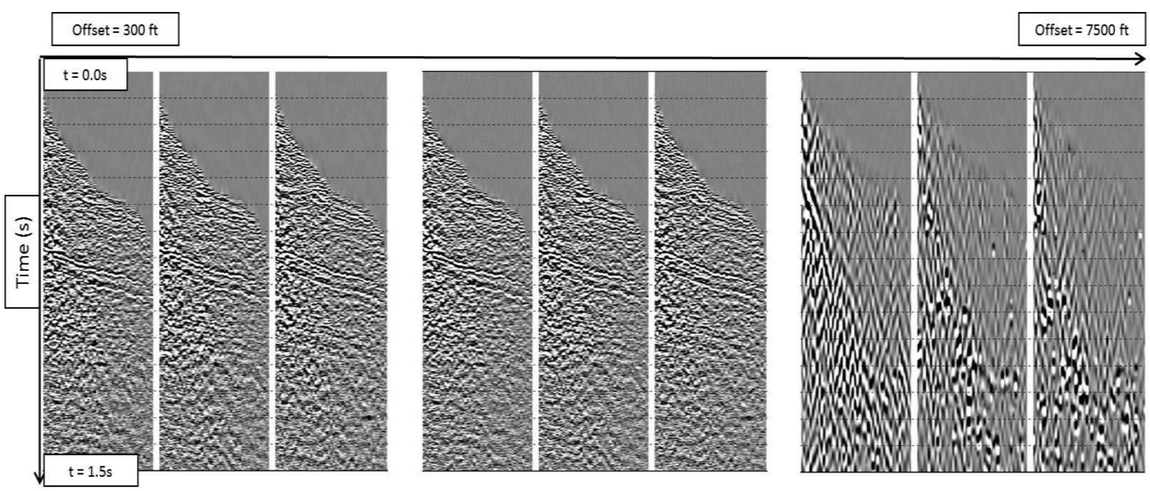

Figure 5.11: CDP gathers before and after LMO filter application and difference plot.

5.5.2 Velocity analysis

Velocities were picked for the entire survey area at 10 inline and 10 crossline intervals. Velocity picking around supplied wells X and Y was four times denser than in non-well areas (5 inline and 5 crossline intervals). Figure 5.12 shows an NMO velocity profile for a CDP gathers from Inline 1267.

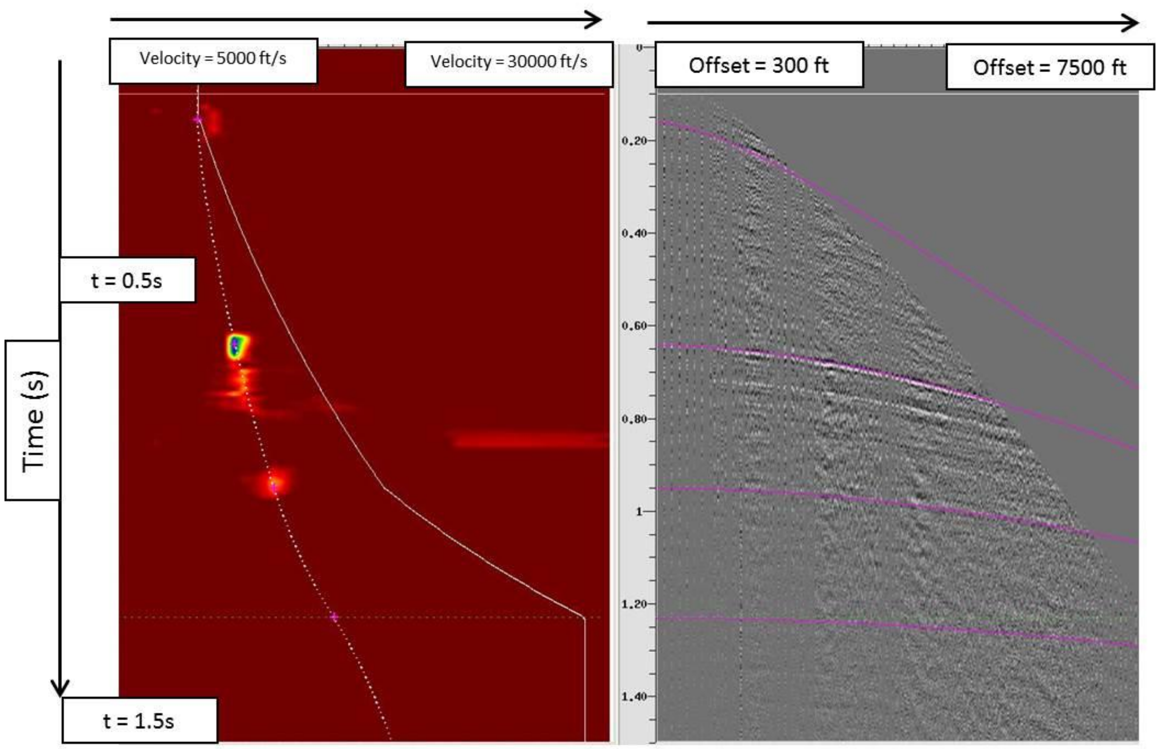

Figure 5.12: Semblance and CDP gathers showing NMO velocity profile.

On close inspection, coherence plots from the top and base of the Barnett can be identified on the semblance section (see section 5.6 for details of seismic interpretation of the Barnett). Figure 5.13 shows the same CDP gather as that in Figure 5.12 before and after NMO correction application. We observe from Figure 5.13 that there seems to be a distinguishable coherence plot for the top and base of the Barnett. This shows that conventional NMO velocity analysis may be adequate to resolve the top and base of the Barnett.

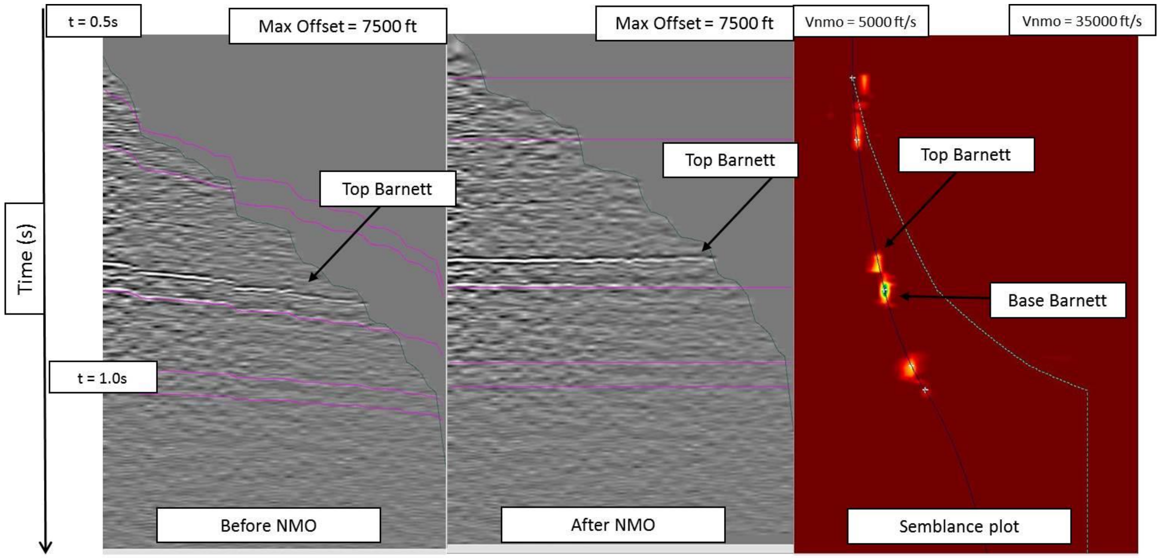

Figure 5.13: CDP gathers before and after NMO correction and corresponding NMO semblance showing coherence at top and base of the Barnett.

The picked NMO velocities were interpolated and smoothed to create a smooth RMS velocity volume. Figure 5.14 shows a smooth RMS velocity section from IL1267.

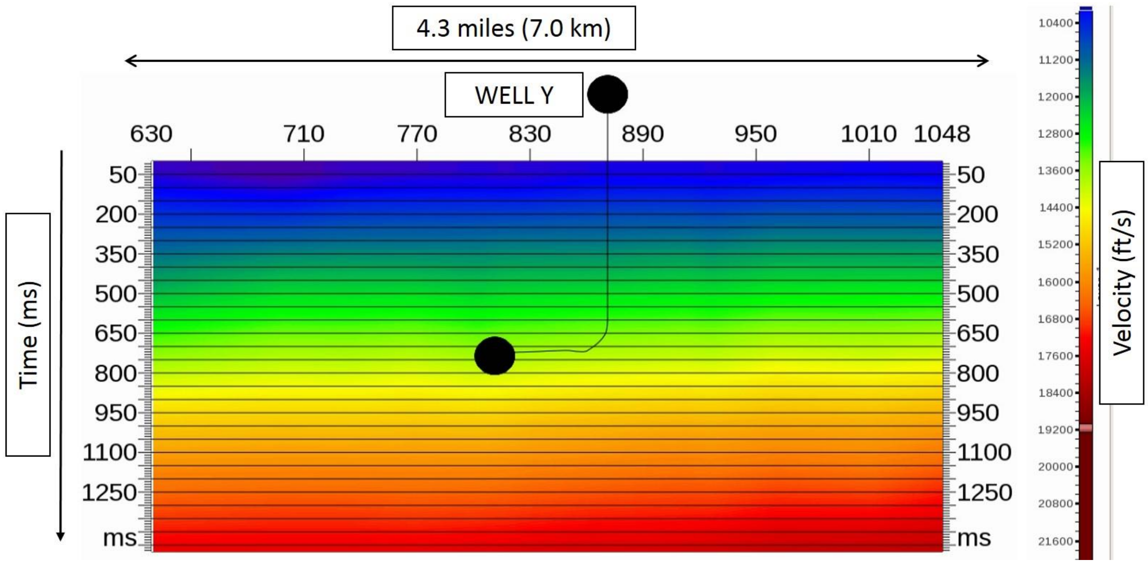

Figure 5.14: Smooth RMS velocity section from IL 1267 showing position of Well Y.

5.5.3 Migration

Kirchhoff prestack migration was run on the whole dataset with noise attenuated CDP gathers and smooth RMS velocity volume as input. Figure 5.15 shows a migrated section from IL 1267 after applying FXY deconvolution to the migrated section.

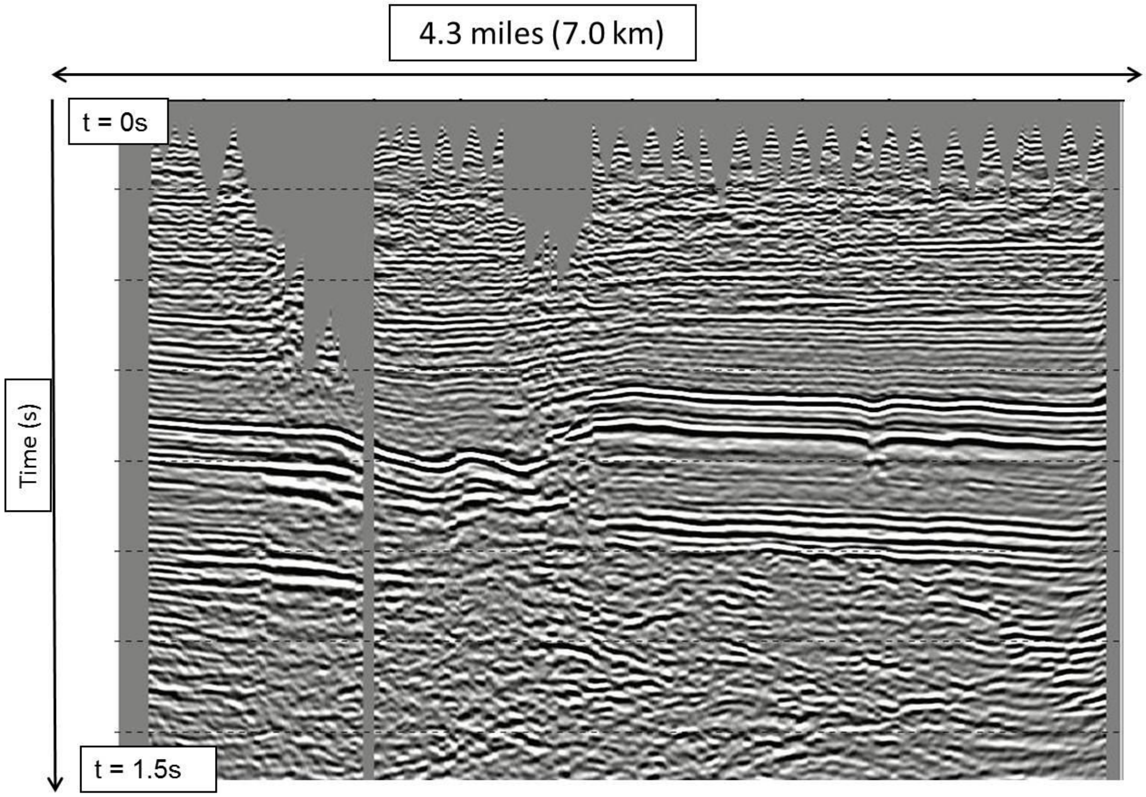

Figure 5.15: Kirchhoff prestack migrated section from IL 1267 after application of FXYdeconvolution.

Figure 5.16 shows Kirchoff-migrated gathers from IL 1267. Notice the difference in residual delay from reflectors representing the top and base of the Barnett.

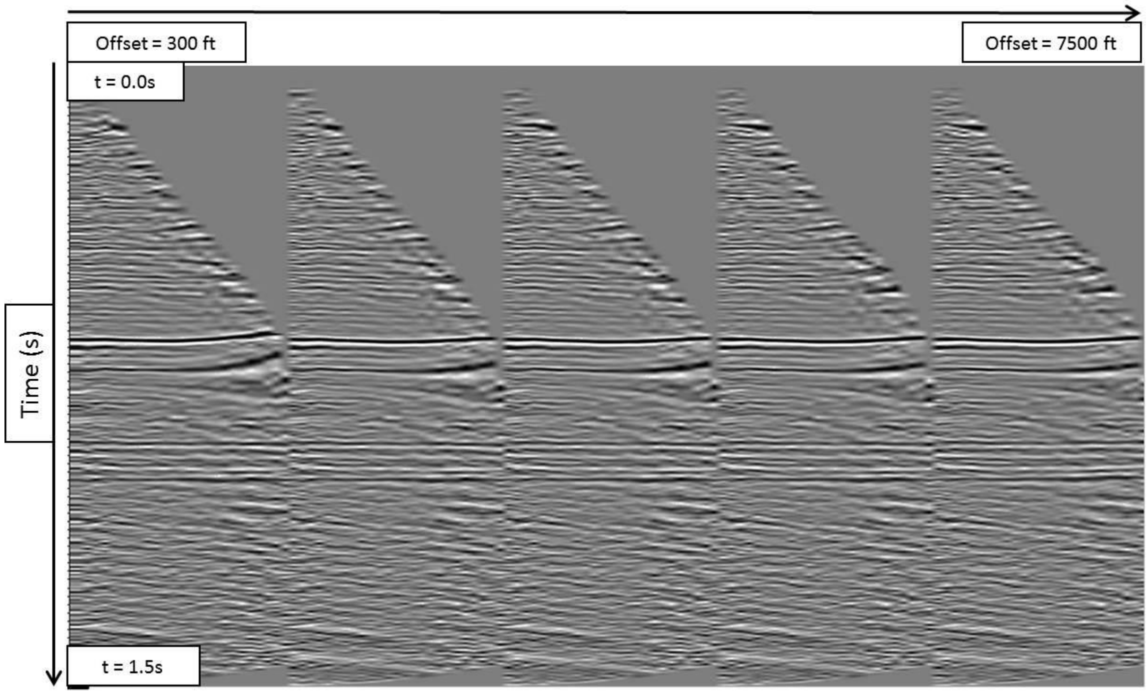

Figure 5.16: Final Migrated Gathers from IL 1267.

5.6 Seismic interpretation

To be able to accurately pick events from the migrated section, a seismic-to-well tie workflow was initiated. After this process, seismic events corresponding to the Marble Falls, Barnett and Ellenberger Formations were able to be characterized with a higher level of confidence. Figure 5.17 shows a seismic-to-well tie panel for well X.

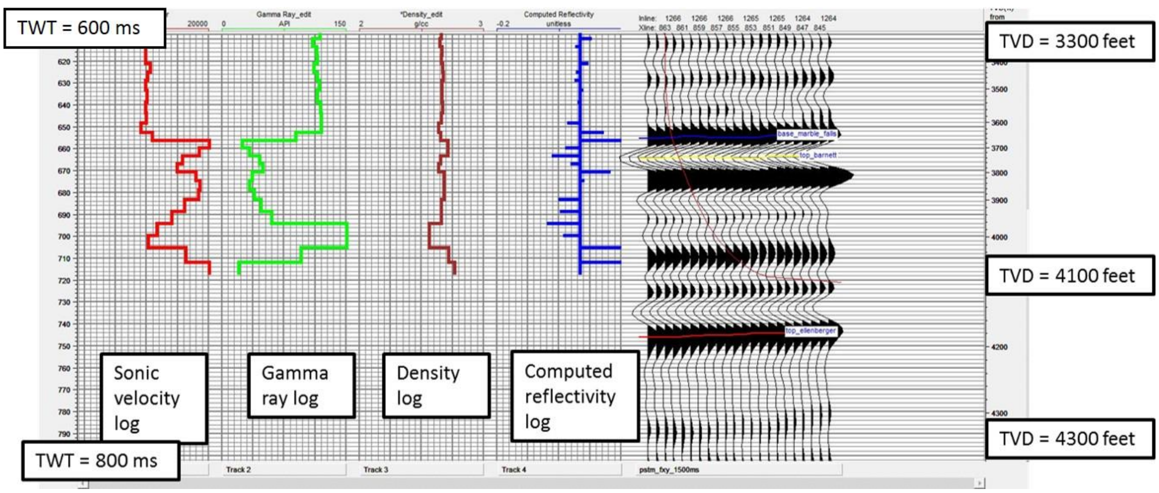

Figure 5.17: Seismic-to-well tie window showing 10m blocked logs and corresponding seismic section for Well X.

With the guidance of the seismic-to-well tie results, horizons were picked at the positions Barnett and Ellenberger Formations. Figure 5.18 shows a time structure map of the Barnett with locations of all supplied wells (wells X, Y and Z).

The presence of major fault structures, as well as karst, easily becomes apparent on close inspection of the Harris dataset. The presence of these structures plays a major role in interpretation, as well as in any anisotropic or azimuthal studies.

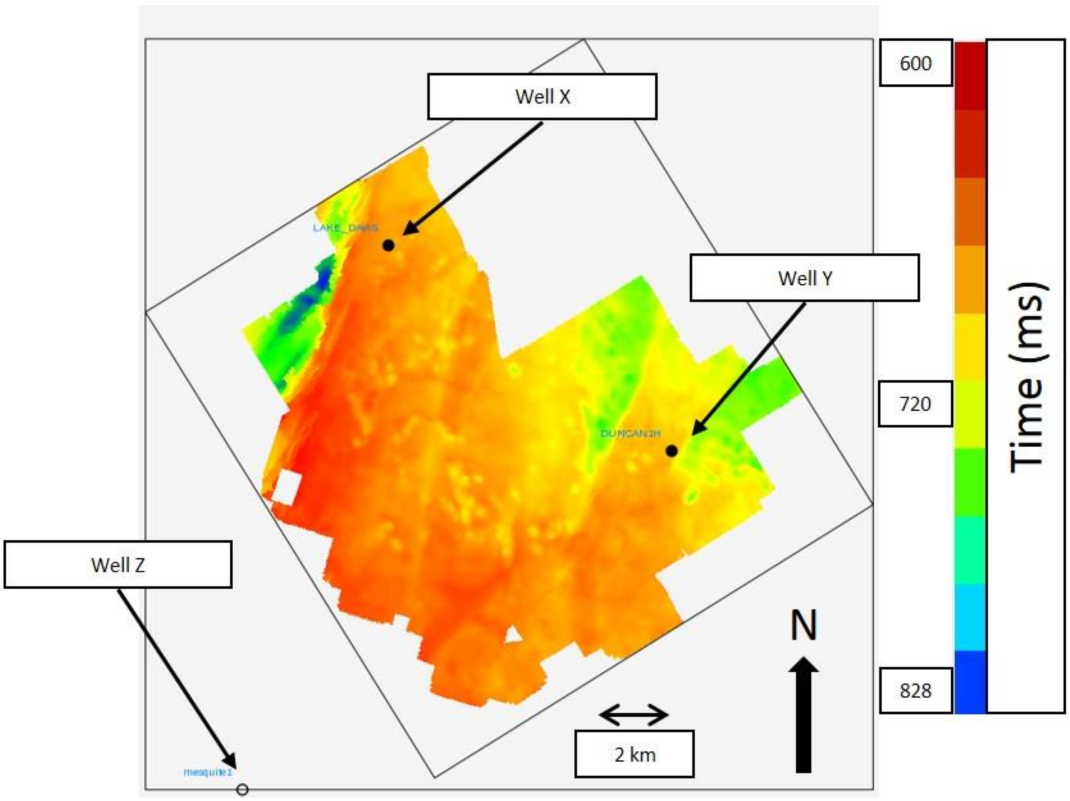

Figure 5.18: Time structure map of the Top Barnett. Display from Paradigm GeoDepth® software.

The highly karsted Ellenberger Formation presents a drilling risk to production in the Fort Worth Basin. Also, because of the importance of faults, dips, and sinkholes to seismic velocity measurements, we have decided to incorporate the Ellenberger Formation into our analysis in this chapter. Figure 5.19 shows a dip map from the top of the Barnett; red arrows point to positions of major fault structures and green arrows highlight approximate positions of sinkholes.

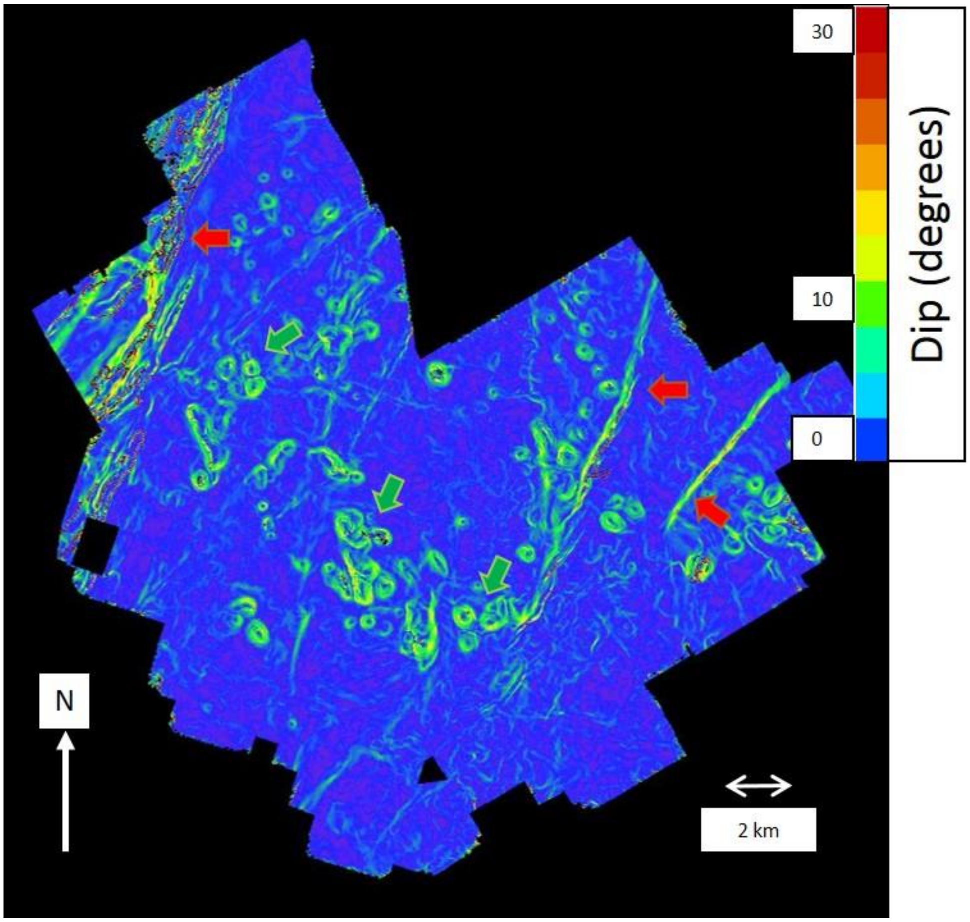

Figure 5.19: Dip structure map of the top Barnett. Red arrows show positions of major fault structures and green arrows show positions of sinkholes. Display from Paradigm GeoDepth® software.

Figure 5.20 shows a corresponding amplitude structure map of the Barnett draped on a time structure map. Figure 5.21 shows more sinkholes and fault structures on an amplitude map of the Ellenberger Formations.

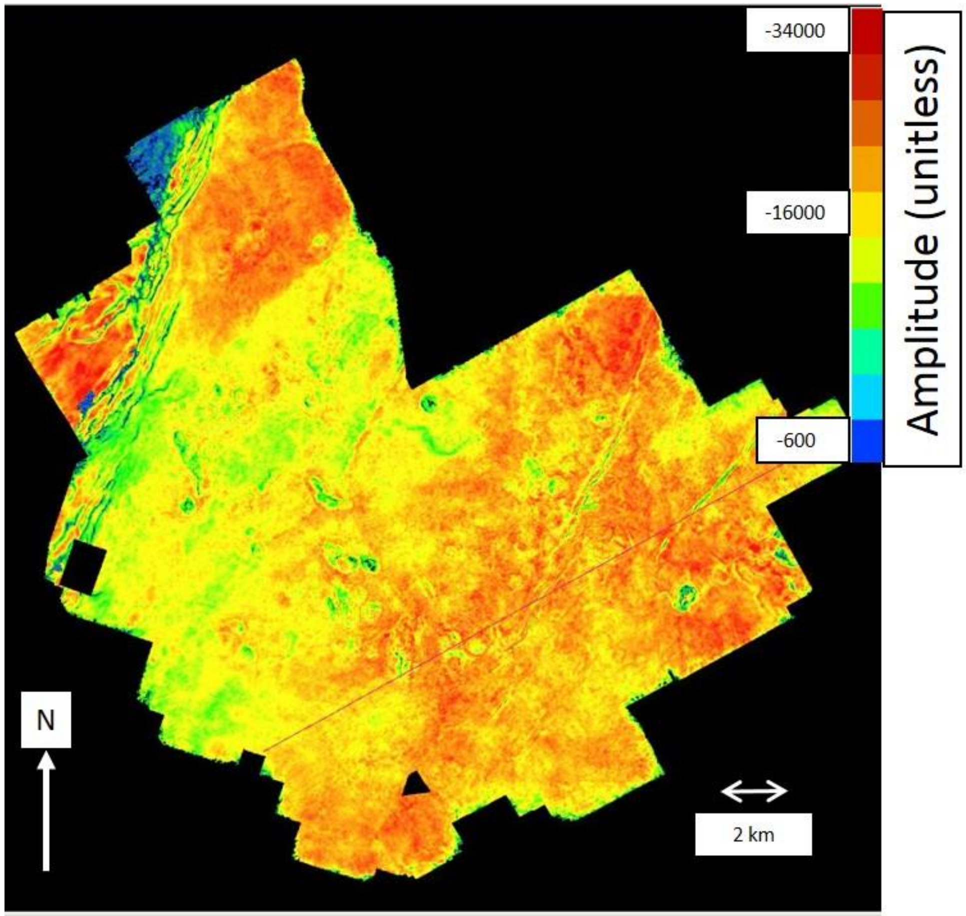

Figure 5.20: Amplitude map from time migrated seismic data draped on top Barnett interpretation.

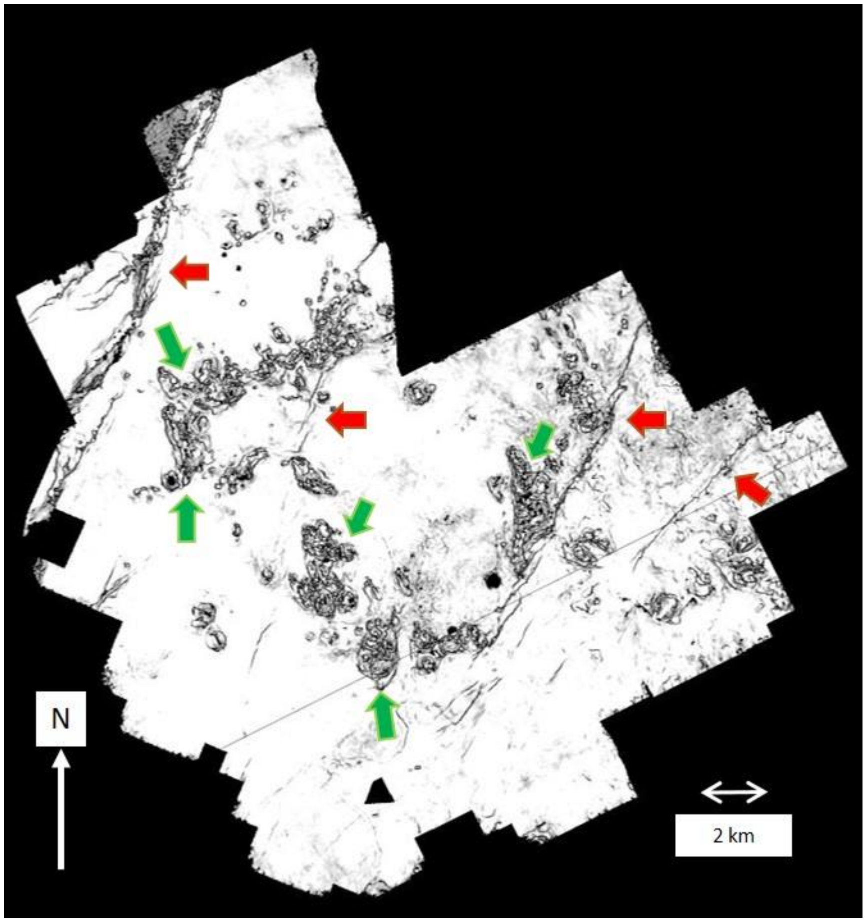

Figure 5.21: Amplitude map of the top Ellenberger (base Barnett). Red arrows show positions of major fault structures and green arrows show positions of sinkholes.

In Figure 5.22 we display 3D Kirchhoff-migrated seismic section around well X.

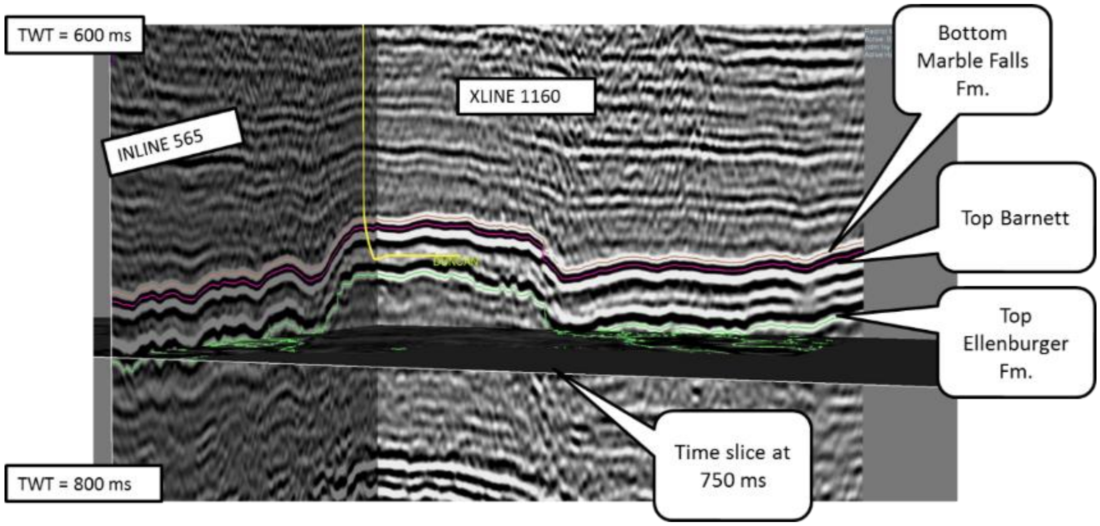

Figure 5.22: 3D display of Kirchhoff-migrated seismic and interpretations with well X.

5.7 P-impedance inversion

Impedance inversion was run on the seismic data to help delineate lithology and help characterize the Barnett and Ellenberger Formations. These studies were intended to serve as precursors and background models for azimuthally sectored inversions (discussed in sections 5.8). Preliminary results show that impedance inversion helps to adequately map lateral variation in rock property in the Fort Worth Basin. Also, attribute-aided impedance modeling will support the mapping of faults and karst features in the Ellenberger Formation. These inversions were run using well data from wells X and Y. Figure 5.23 shows a migrated seismic section at IL 1267 (input to the inversion) and the deviated well X, as well as seismic horizons corresponding to Base Marble Falls, Top Barnett, and Top Ellenberger Formations (Base Barnett).

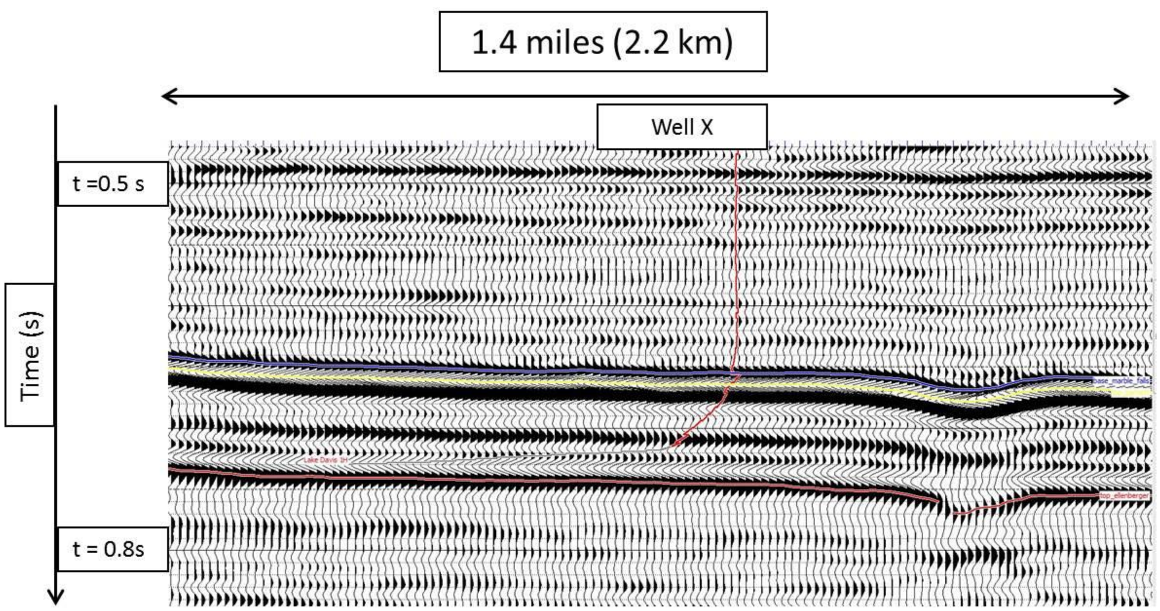

Figure 5.23: Migrated section from IL 1267 showing deviated well X as well as seismic horizons corresponding to Base Marble Falls, Top Barnett, and Top Ellenberger (Base Barnett) Formations.

Figures 5.24 and 5.25 show P-impedance maps for the Barnett and Ellenberger Formations respectively.

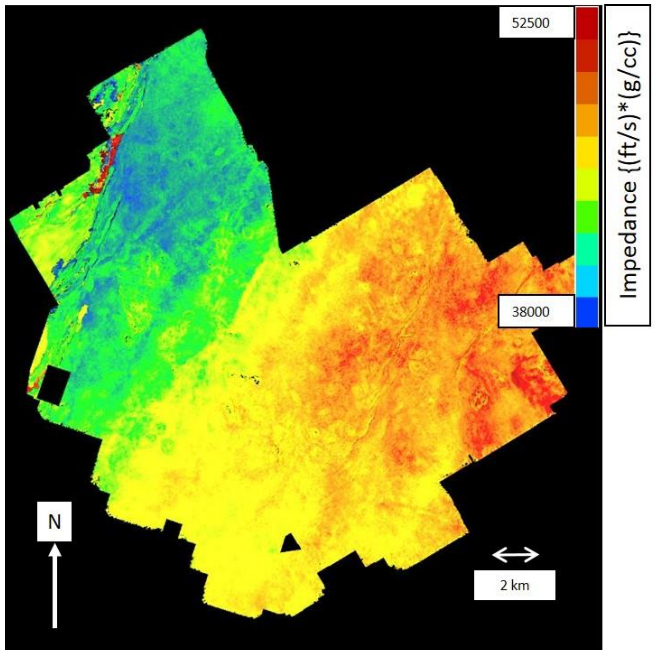

Figure 5.24: Inverted P-impedance for top Barnett (color range: 38000 – 52500 {(ft/s)*(g/cc)}).

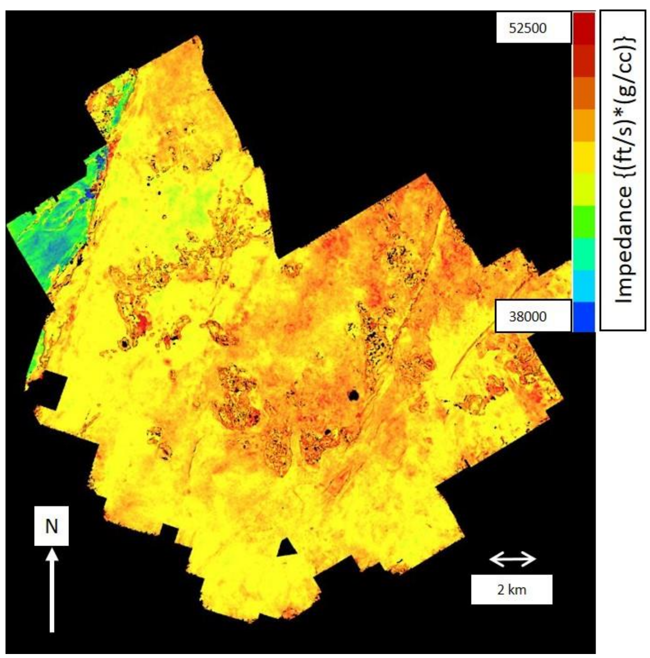

Figure 5.25: Inverted P-impedance for top Ellenberger (color range: 38000 – 52500 {(ft/s)*(g/cc)}).

5.8 Azimuthally sectored P-impedance inversion

In order to further characterize subsurface anisotropy in our survey area, we sectored the data into two broad azimuths based on *a priori* knowledge of stress and fracture direction in the Fort Worth Basin. Following Bruner and Smosna (2011), only one set of natural fractures (strike 100°-120°) is recognized in the Barnett.

In the Fort Worth Basin case study, our chosen azimuthal sector was 90°. This resulted from experimentation and detailed study of the wide-azimuth data. In all there were 2 azimuthal sectors. Sector 1 contained azimuths 0° → 90° and Sector 2 contained azimuths 91° →180°. Figure 5.26 is an illustration the azimuth sectors from a hypothetical single CDP location.

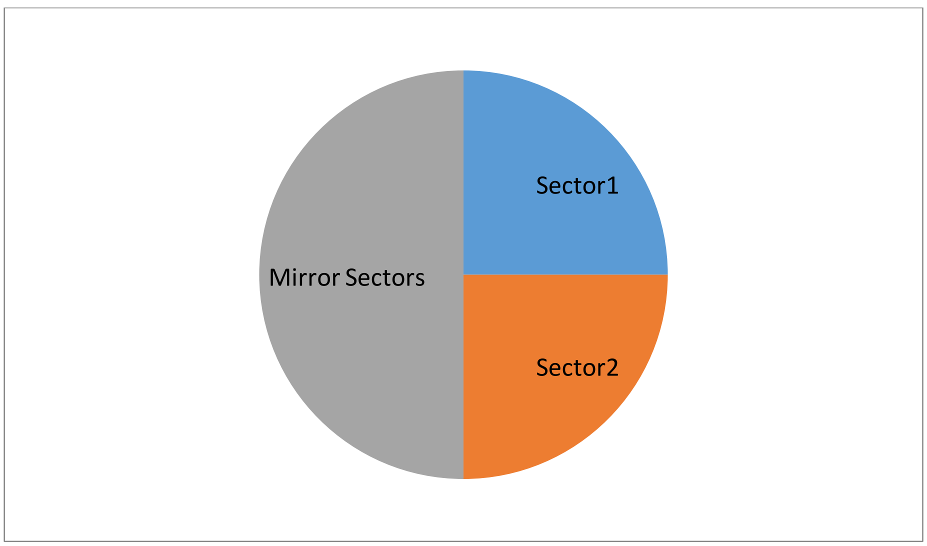

Figure 5.26: Illustration of chosen azimuth sectors in the Harris survey.

After azimuthal sectoring, P-impedance inversions using wells X and Y were run separately on each azimuth sector, to create azimuthally varying inversion results. Figure 5.27 illustrates results from the azimuthally sectored inversions.

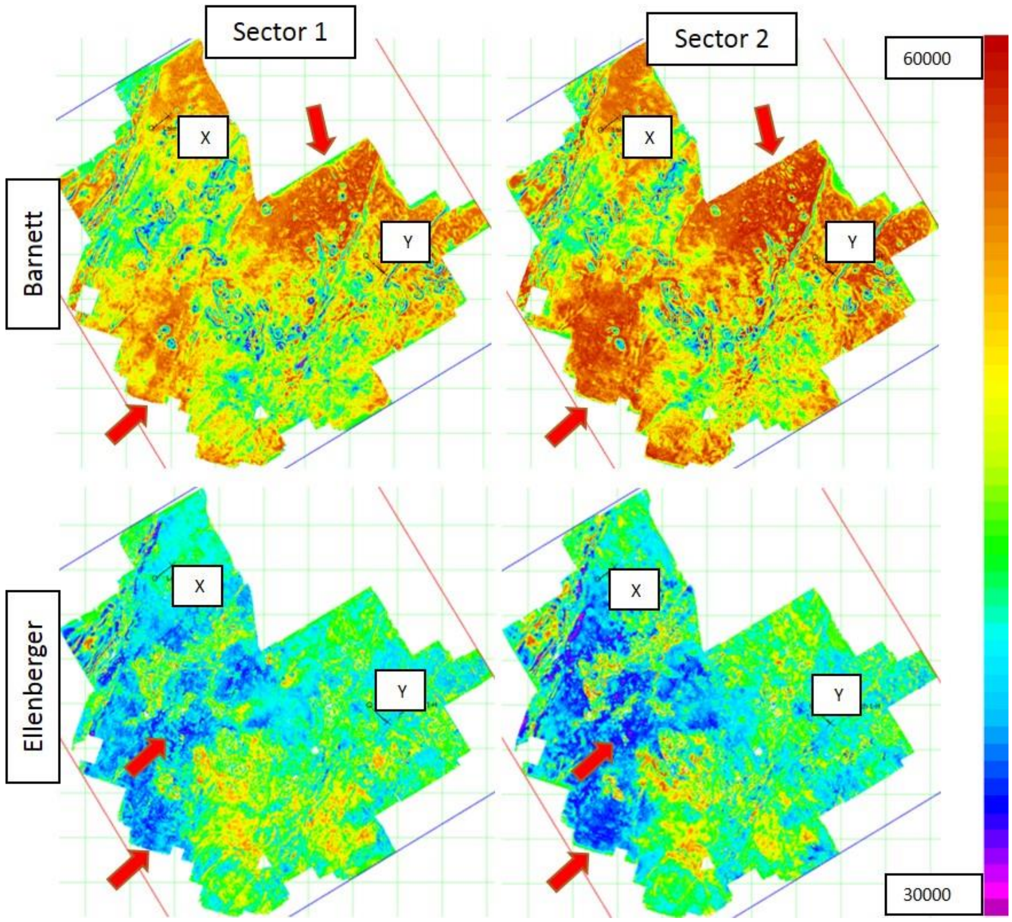

Figure 5.27: Inverted P-impedance for top Barnett and top Ellenberger from two different azimuth sectors (color range: 30000 – 60000 {(ft/s)*(g/cc)}). X and Y represent the positions of wells X and Y respectively. Display from Hampson-Russell® software.

From Figure 5.27, we can observe that in the case of the Barnett, azimuth Sector 2 seems to be the fast direction. This might not be the case for the Ellenberger, as we tend to observe an enlargement of areas of lower P-impedance values going from azimuth Sectors 1 to 2. Figure 5.28 shows the result of subtracting P-impedance values of azimuth Sector 2 from Sector 1 to observe the difference between these two azimuthal sectors.

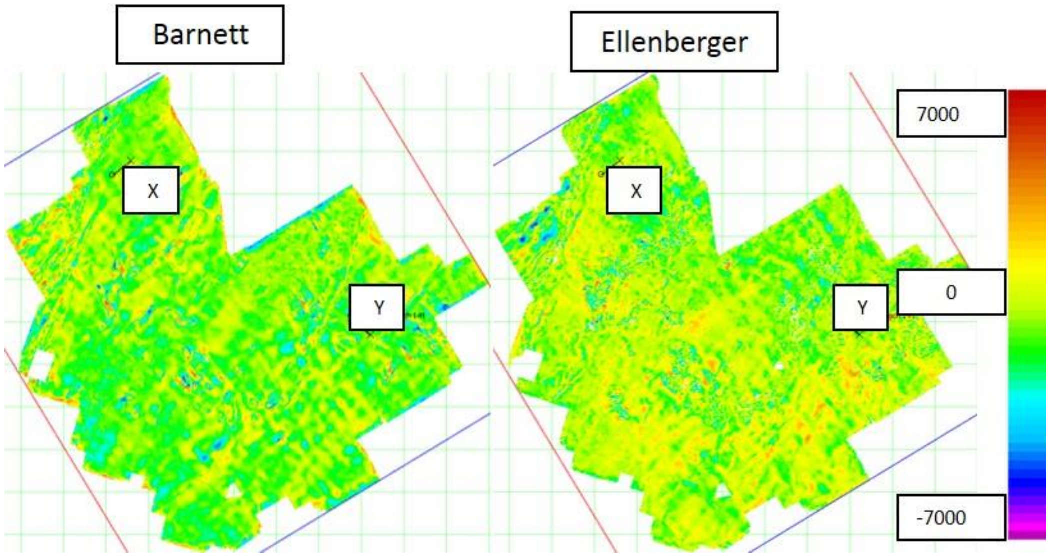

Figure 5.28: Difference in inverted P-impedance values between azimuth Sectors 1 and Sector 2 for top Barnett and top Ellenberger (color range: -7000 to +7000 {(ft/s)*(g/cc)}).

In order to understand the relationship that the volumes show in Figure 5.28 have with highly dipping structures on the Barnett, the difference volume (P-impedance difference volume between two azimuthal sectors) was crossplotted with dip (in degrees). Figure 5.29 shows a crossplot of P-impedance difference volumes between two azimuthal sectors and dip in the Barnett; it can be seen that many data are clustered in the middle part of the x-axis (the areas around the yellow polygon). This in effect means a sizeable portion of the data show zero or little difference in P-impedance from one azimuth to the other. Other parts of the data show high difference in impedance while having low dip (the areas around the green polygons). These data points around the green polygons might be good areas to investigate for anisotropy due to either stress and/or fractures.

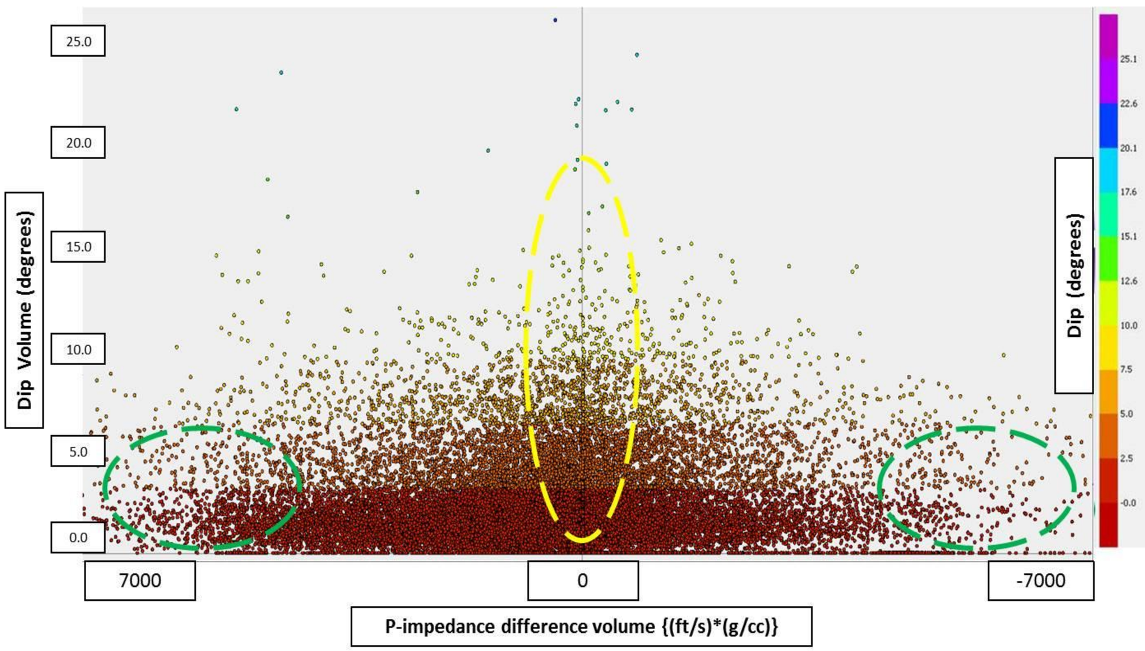

Figure 5.29: Crossplot of P-impedance difference volume between two azimuthal sectors and dip in the Barnett. Areas around yellow polygon are areas of low P-impedance difference and areas around green polygon are areas with low dip and high P-impedance difference.

5.9 Residual eta (η) analysis

An initial 4th order correction analysis on Kirchhoff-migrated gathers suggested that greater residual eta values are common at the base of the Barnett (top Ellenberger). These high 4th order correction values may be due to the presence of karst and fault structures in the Ellenberger. Also, in section 5.5.3 and Figure 5.16, we noticed significant residual delays on gathers in the Harris survey area. These delays were mostly associated with the top Barnett and top Ellenberger Formations (or Base Barnett). This confirms the already known fact of the presence of anisotropy (or preferred orientations) in these Formations.

In the absence of a significant dip and lateral heterogeneity, we can express moveout time as a hyperbolic equation, (Grechka and Tsvankin, 1999b);

$$(\boldsymbol{\alpha}) = \mathbf{A_0} + \mathbf{A_2}\mathbf{x}^2(\boldsymbol{\alpha}) + \mathbf{A_4}\mathbf{x}^4(\boldsymbol{\alpha}) \qquad (5.1)$$

where,

$$\mathbf{A_0} = \mathbf{t_0^2}, \quad \mathbf{A_2} = \frac{\mathbf{x^2}}{\mathbf{V_{nmo}^2}} \text{ and } \mathbf{A_4} = \frac{\mathbf{2\eta x^4}}{\mathbf{V_{nmo}^4 t_0^2}}$$

x is the source-receiver offset, V_{nmo} is normal moveout velocity, t_o is the zero offset travel time, $\boldsymbol{\eta}$ is residual eta and α is the source-receiver azimuth.

4th order or A_4 terms are long offset correction terms which may or may not be due to anisotropy. The A_4 (or 4th order) term is proportional to the $\boldsymbol{\eta}$ term in the absence of dips or significant lateral heterogeneities. However, in the case of the Fort Worth Basin (especially in the Ellenberger Formation), we suggest that some part of the observed eta values may be due to the presence of sinkholes and fault structures. In Figure 5.30, we present a workflow session of residual eta analysis of the Harris dataset from IL 1267. Residual eta analysis was performed on a decimated Harris 3D volume. This process was performed on the whole Harris 3D dataset but at every 10 inline by 10 crossline. Since the Harris survey contains up to 1.33 million CDPs (as described in section 5.4.1), RMO analysis was performed on 13,300 CDPs.

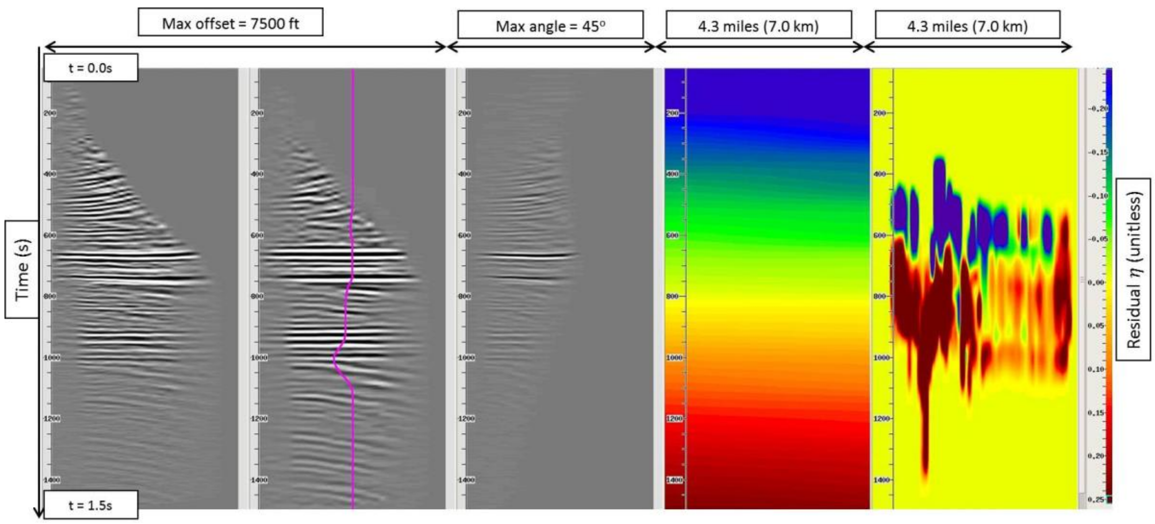

Figure 5.30: Residual delay analysis section from IL 1267 showing a) migrated gather; b) preconditioned gather (gather after applying 2nd and 4th order NMO corrections); c) corresponding angle gather (migration velocity was used to cover offset to angle gathers); d) Migration (or RMS) velocities, and; e) Residual eta (η) section, generally ranging from -0.25 (blue) to 0.25 (red). Display from Paradigm GeoDepth® software.

In Figure 5.30, we can also observe that positive residual delay values are more common around the Ellenberger, but the Barnett has both positive and negative residual delay values.

In a conventional seismic processing workflow, these residual delays (especially negative η) are usually corrected in various NMO correction iterations so as to adequately flatten the gathers. In this study, we decided to analyze these data and search for clues as to the orientation and nature of subsurface anisotropy. Figure 5.31 shows residual η map of the Ellenberger Formation; as it can be seen that some areas of high η values (circled in purple) correspond to areas with high dip (i.e. faults and sinkholes; compare to Figure 5.21). Figure 5.32 shows a residual η map of the Barnett Formation (adjusted to same color scale as Figure 5.31); notice there are more negative (generally lower) values at the Barnett.

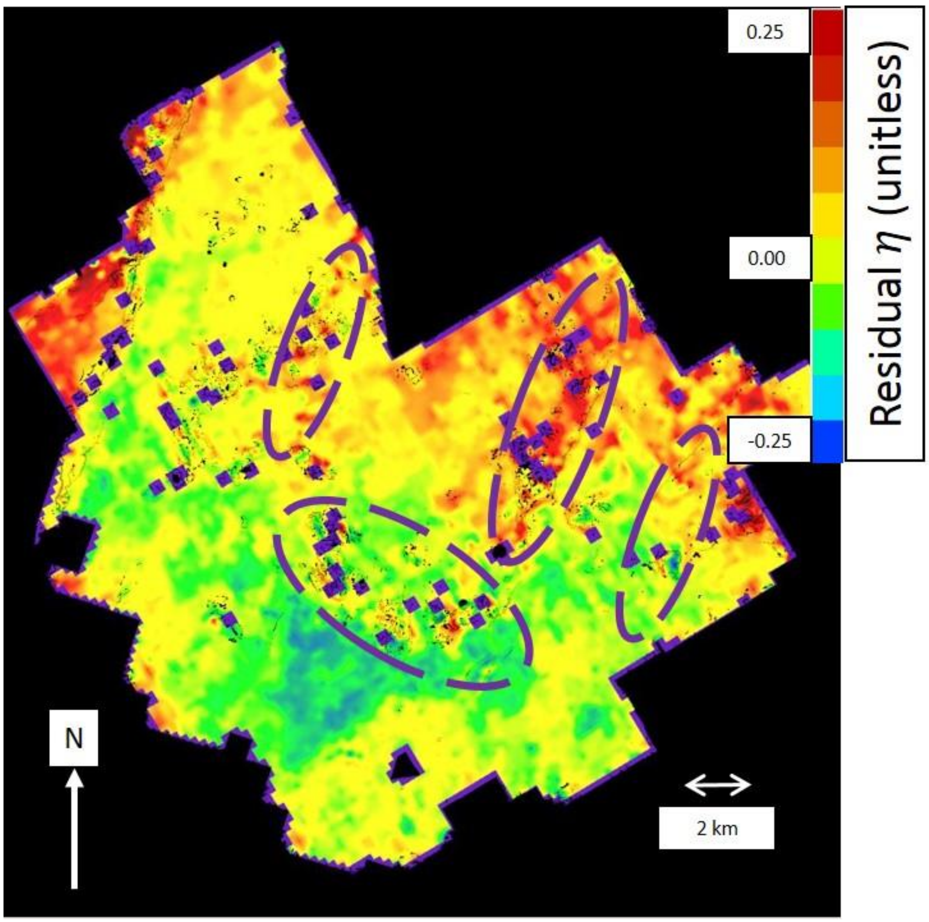

Figure 5.31: Residual η map of the Ellenberger Formation; areas circled in purple are approximate locations of major fault and karst structures in the survey area.

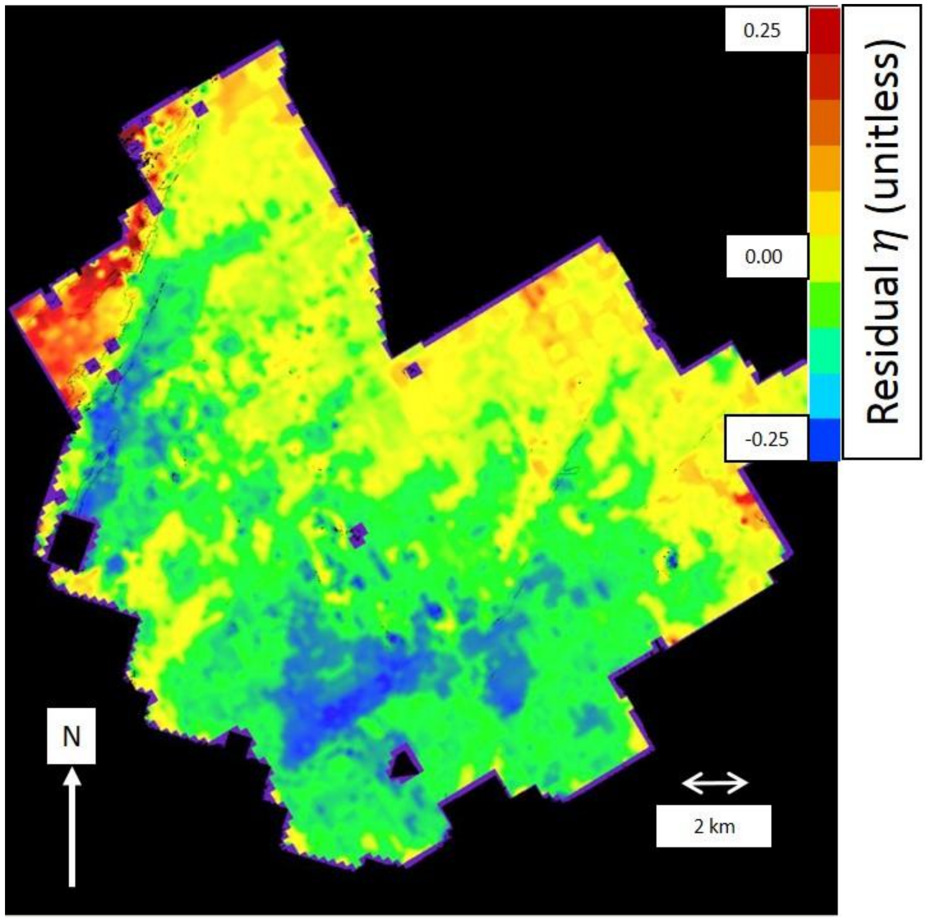

Figure 5.32: Residual η map of the Barnett.

In order to eliminate the effects of the high dips (faults and karst) on our residual delay readings, a crossplot of dip and residual eta was made at the Ellenberger interval. Figure 5.33 shows a crossplot of dip and residual η colored in dip values in the Ellenberger. Purple polygon areas represent areas of high dip (above 5°) and high η values. In these areas, there is a high likelihood these high η are strongly influenced by the faults and chimney structures of the Ellenberger. In the green polygon areas, there are high η but low dip. The η values in this area are more likely to be influenced by anisotropy (and/or stress).

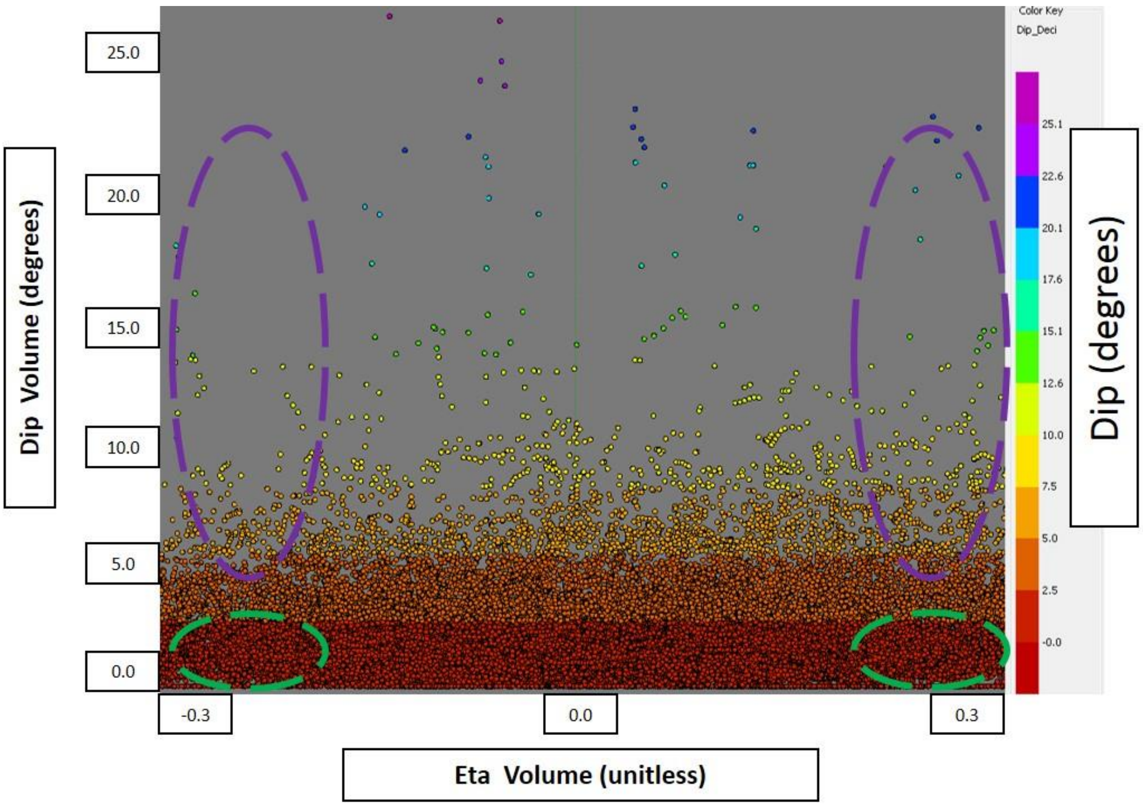

Figure 5.33: Crossplot of dip and residual $\boldsymbol{\eta}$ at the Ellenberger. Purple polygon areas represent areas of high dip and $\boldsymbol{\eta}$. Green polygon areas represent areas of high $\boldsymbol{\eta}$ and low dip (of more interest to this study because $\boldsymbol{\eta}$ is more likely to be influenced by anisotropy). Display from Hampson-Russell® software.

5.10 Azimuthally sectored RMO analysis

Using the same azimuthal sectors discussed in section 5.8, we performed RMO analysis and compared results for both the Ellenberger and the Barnett. These azimuth sectors were chosen because of an *a priori* knowledge of stress and fracture directions in the Fort Worth Basin. Following Bruner and Smosna (2011), only one set of natural fractures (strike 100^o-120^o) is recognized in the Barnett. Figure 5.35 illustrates results from the azimuthally sectored RMO analysis. Figure 5.34 shows there is a more subtle difference in RMO results in the Barnett. However, there are more apparent differences in RMO results (across two azimuth sectors) in the Ellenberger Formation.

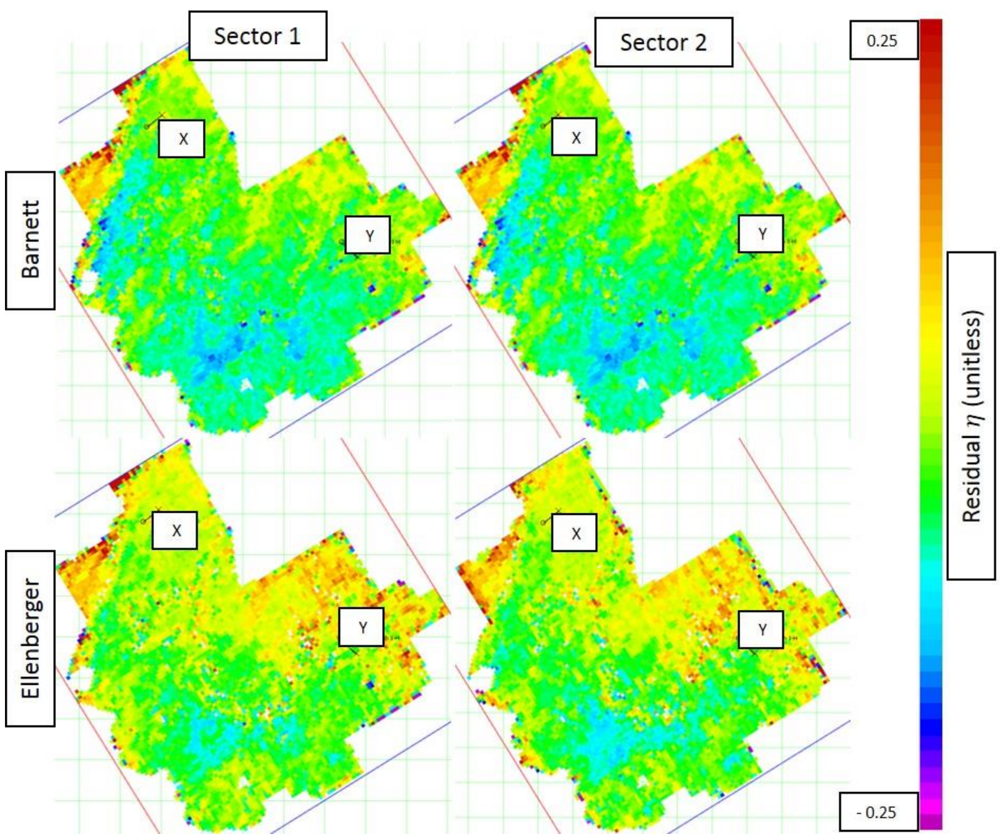

Figure 5.34: Residual $\boldsymbol{\eta}$ map for top Barnett and top Ellenberger from two different azimuth sectors (color range: 0.25 to -0.25). X and Y represents the positions of wells X and Y, respectively.

5.11 Conclusions

In this chapter we presented a practical but simple workflow for characterizing subsurface anisotropy in the Barnett shale play.

We presented a workflow for using azimuthally sectored P-impedance inversion to get a general overview of the anisotropic field in the Barnett. Naturally, some of these anisotropies are due to highly dipping structures. A future project will be to use these azimuthally sectored inversions to generate slowness ellipses for all CDP locations in the Harris survey.

We also presented results from analysis of residual moveouts in the Barnett and Ellenberger Formations. We observed a relationship between areas of high dip (areas of faults and karst structures) and high RMO values; we also observed areas of high RMO values but little to no dip structures. A future project will be to further investigate these areas (high RMO but low dip).

Most importantly in this chapter, we analyzed data from a frontier wide-azimuth seismic acquisition survey acquired in 2006. The goal was to understand the azimuthal and anisotropic response of the Barnett via the use of these wide-azimuth surface seismic data.

Acknowledgements

The authors are grateful to Marathon Oil Corporation for donating the dataset for this project. We are also grateful to Paradigm Geophysical and CGG/Hampson-Russell for the donation of software used for processing and interpretation of this project.

5.12 References

Bruner, K.R., and Smosna, R., 2011, A Comparative study of the Mississippian Barnett Shale, Fort Worth Basin, and Devonian Marcellus Shale, Appalachian Basin, US department of energy: National energy laboratory publication, **1478**.

Montgomery, S.L., Jarvie, D.M., Bowker, K.A., and Pollastro, R.M., 2005, Mississippian Barnett Shale, Fort Worth Basin, north-central Texas: Gas-shale play with multi-million cubic foot potential, American Association Petroleum Geologists Bulletin, **89**, 155–175.

Pollastro, R.M., L.N.R. Roberts, T. A. Cook, and M.D. Lewan, 2008, Assessment of Undiscovered Technically Recoverable Oil and Gas Resources of the Bakken Formation, Williston Basin, Montana and North Dakota, USGS Open-File Report 2008–1353 Sheet 3 of 3.

Remington, L., and J, Simmons., 2009. The legendary Barnett. Barnett Playbook. Hart Energy Publication.

Trumbo, A., and J.P, Rich., 2013, Azimuthal variations in attributes for induced fracture detection in the Barnett Shale. Interpretation. **1**, SB51-SB59.

CHAPTER SIX

CONCLUSIONS

In the first set of forward modeling experiments, we investigated the influence of different saturating fluids on anisotropy in an azimuthally anisotropic medium. Within the limits of our experiments, we found a relation between fluid type and the magnitude of shear-wave splitting. Physical properties such as P- and S-wave velocities as well as seismic birefringence were affected by changes in density and compressibility resulting from fluid substitution. Results also showed that the nature of the saturating fluid had a direct influence on the trend of azimuthal NMO (NMO ellipses). We also observed that slow shear-waves seem more sensitive to fluid changes than fast shear-waves. As fluid saturants changed in our synthetic HTI medium, we detected a decrease in anisotropic parameter ε (as water and glycerin saturations were increased). The reverse was the case for anisotropic parameter γ.

In the second set of experiments, we investigated the dynamic elastic properties of a layered orthorhombic medium as a function of uniaxial stress. In most cases, we detected a general increase in measured velocities with uniaxial stress. We observed an unusual strain trend during unloading from the stress strain curve. This may have been due to low-frequency heterogeneity or anisotropy within the composite model. Also, we observed anisotropic behavior *a priori* to both orthorhombic and VTI symmetries in different principal axes of the model as uniaxial normal stress increased.

In our first field analysis, we investigated changes in seismic attributes as a function of azimuth using a wide-azimuth dataset from Ross oil field in the Williston Basin, North Dakota. We concluded that velocity-based methods such as azimuthal NMO analysis can help understand and characterize the direction and intensity of anisotropy in the subsurface. Finally, in the second field analysis, we combined the analysis of RMO with azimuthally sectored P-impedance inversion to create a broad overview of the nature of anisotropy in the Fort Worth Basin. We found anisotropic symmetry akin to mild VTI anisotropy in the Fort Worth Basin. Some azimuthal anisotropy effects may have been due to the presence of highly dipping structures.

APPENDIX A: Reflectivity modeling for fluid saturated physical model

In order to understand and characterize the individual events from the CDP gathers described in Section 2.4.4 (Chapter 2), we executed reflectivity modeling for the composite model using the model parameters shown in Tables 2.1 and 2.2. The intention was to use this reflectivity model to inform our interpretation of the CDP and NMO results presented in Chapter 2 (Section 2.4.4).

From the schematic diagram of underwater experimental setup shown in Figure 2.11 and using values from Tables 2.1 and 2.2, we are able to create a more detailed picture of the model and its physical properties. The modeling tool used for reflectivity modeling in this project was Anivec®. Anivec is modeling software based on work done by Mallick and Frazer (1990).

Figure A1 shows the input model to Anivec modeling tool based on values from Tables 2.1 and 2.2.

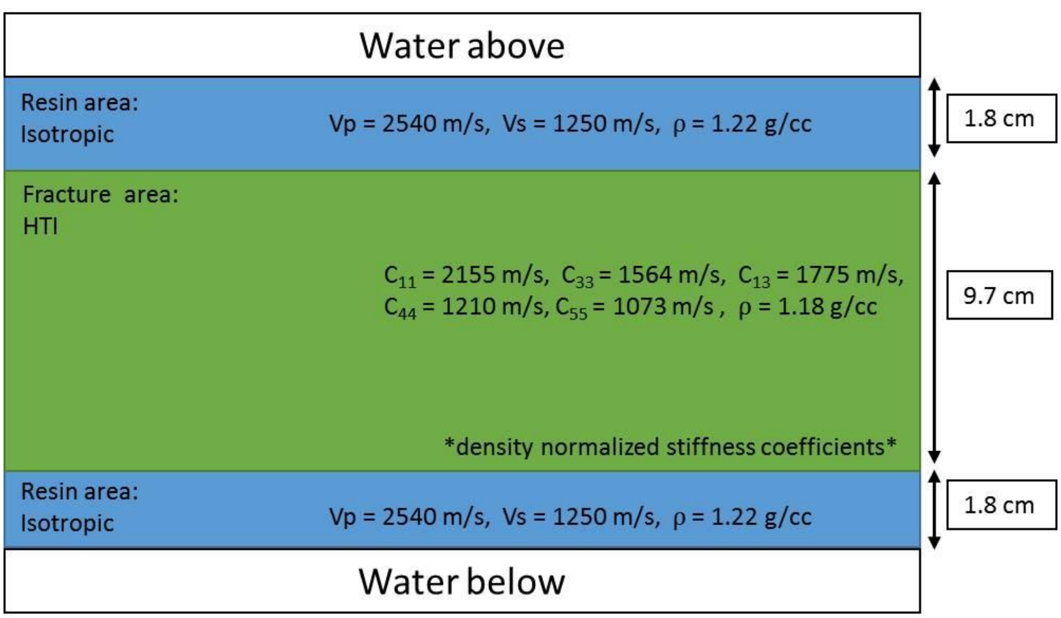

Figure A1: Input to Anivec modeling tool based on values from Tables 2.1 and 2.2.

The reflectivity modeling was run using 45 Hz and 10 Hz central frequency ranges. 45 Hz was to help better identify events corresponding to the top and bottom of the fracture area. The frequency of the modeled data (physical modeling experiment) was 10 Hz. Figure B2 shows all three gathers (45 Hz Anivec modeled, 10 Hz Anivec modeled and data from physical model). The model was run either on the slow direction (corresponding to 90^o source-receiver azimuth) or on the axis of symmetry only.

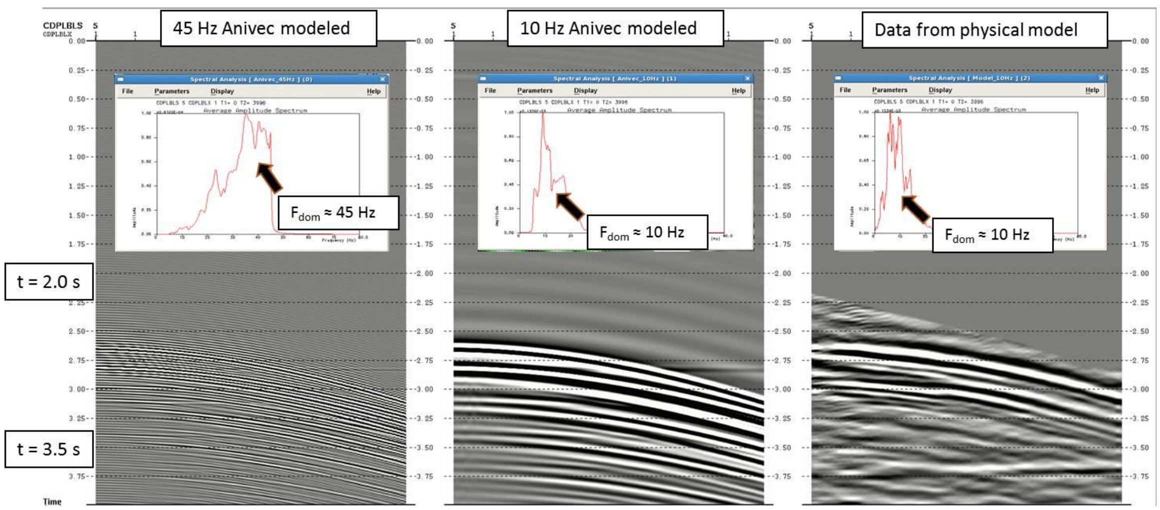

Figure A2: Seismic display showing: a) Anivec modeled synthetic CMP gather with central frequency of 45 Hz; b) Anivec modeled synthetic CMP gather with central frequency of 10 Hz; and c) CMP gather acquired over physical model. (Min offset = 4cm, max offset = 22cm offset interval = 0.3cm, azimuth = 90^o).

In Figure A2, we can observe similarities between B2 (b) and B2 (c), because both have a central frequency of 10Hz. This shows our model parameters are able to numerically modeled and that the physical modeling experiment is fairly reproducible under similar conditions.

A.1 45 Hz Anivec modeled data

Using an average velocity of 2000 m/s for the whole model, a 45 Hz central frequency data has an approximate wavelength of 44 m (0.44 cm). With this resolution, we are able to begin to identify events corresponding to the top and base of the model and fracture zones (the thinnest layer in the model was the resin area with a thickness of 1.8 cm).

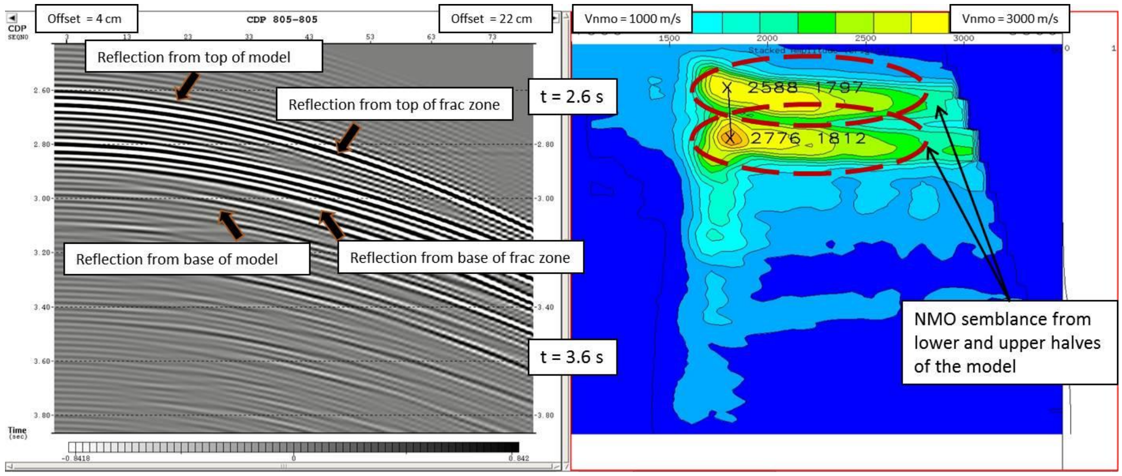

Figure A3: 45 Hz central frequency modeled CMP gather (azimuth = 90^{o}) showing approximate position of events of interest and stacking velocity semblance plot with time-velocity pairs.

In Figure A3, we can observe the approximate positions of the top and bottom of the fracture zone and composite model. However, on the stacking velocity semblance plot, we observe only two distinct semblances, which seem to correspond to the upper and lower half of the model. A plausible explanation for this type of semblance (NMO semblance) behavior is due to the ultra-low resolution of stacking velocity semblance. In this case (as true throughout this project), the resolution of the velocity semblance was estimated to be about 5 cm to 6 cm. With a model 13cm in depth, we might expect to see one to two full velocity semblances only.

A.2 10 Hz Anivec modeled data

A 10 Hz central frequency was used for reflectivity modeling for the sole purpose of mimicking the physical modeling data (physical modeling data has a central frequency of 10 Hz). Using an average velocity of 2000 m/s for the whole model, a 10 Hz central frequency data has an approximate wavelength of 200 m (2.0 cm). With this low resolution, we expected tuning, especially from the resin area; the thinnest layer in the model is the resin area, with a thickness of 1.8 cm. The top and base of the model and fracture zones were harder to identify.

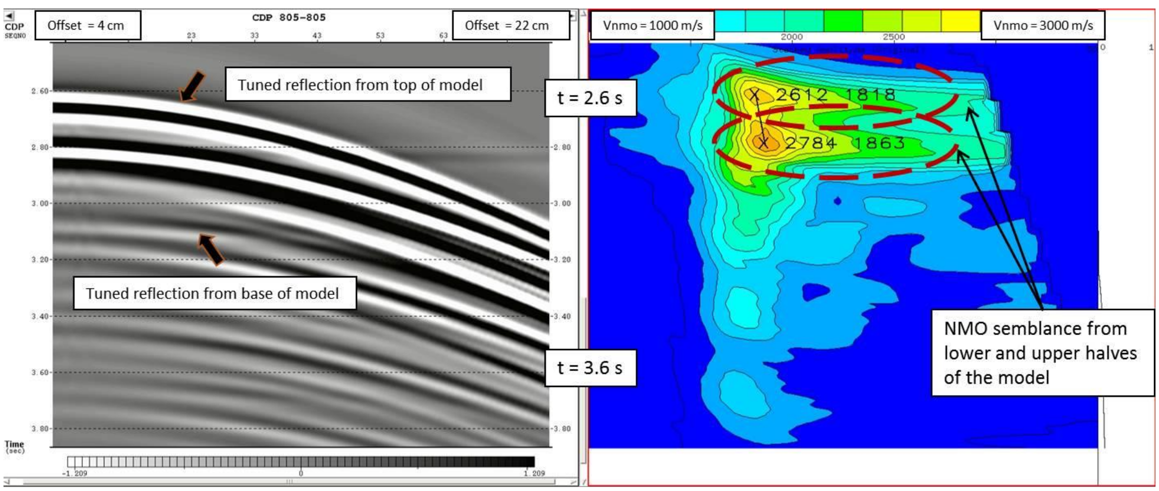

Figure A4: 10 Hz central frequency modeled CMP gather (azimuth = 90º) showing approximate position of events of interest and stacking velocity semblance plot with time-velocity pairs.

In Figure A4, we can observe a similar NMO semblance trend but reflectors on the gathers are more tuned and event identification is more difficult. With these modeling results, we can identify events on our physical modeling data with a higher degree of confidence.

B.3 Physical modeling data

The physical modeling data has a central frequency of 10 Hz. This essentially means it can neither resolve the top nor base of fractures. However, with the help of some reflectivity modeling, we were able to understand the physical modeling data better.

Figure B5 shows the physical modeling data with the approximate positions of events of interest.

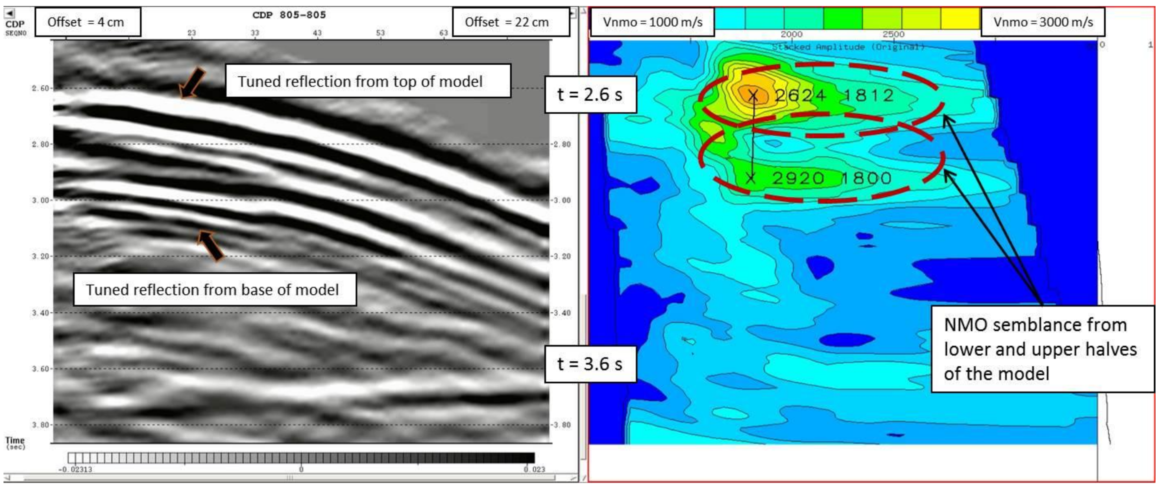

Figure A5: Physical modeling CMP gather (azimuth = 90°) showing approximate positions of events of interest and stacking velocity semblance plot with time-velocity pairs.

In Figure A5, we were able to estimate positions for our events of interest. Also, the velocity semblance plots had a very low resolution (5 cm to 6 cm) and so only two cycles of semblances were plotted. This appears to further tune the events of interest in the velocity domain.

References

Mallick, S., and L, N. Frazer., 1990, Computation of synthetic seismograms for stratified azimuthally anisotropic media. Journal of Geophysical Research. **95**, 8513-8526.